Synthesis of Ferroelectric Semiconductor Nanocrystals via Cation Exchange

By

Cara Elisabeth Bradsher

Dissertation

Submitted to the Faculty of the

Graduate School of Vanderbilt University

in partial fulfillment of the requirements

for the degree of

DOCTOR OF PHILOSOPHY

in

Chemistry

December 18, 2021

Nashville, Tennessee

Approved:

Sandra J. Rosenthal, Ph.D.

Janet E. Macdonald, Ph.D.

Timothy P. Hanusa, Ph.D.

D. Greg Walker, Ph.D.

ACKNOWLEDGEMENTS

TABLE OF CONTENTS

LIST OF FIGURES

CHAPTER I

INTRODUCTION

1.1 Semiconductor Nanomaterials

Nanomaterials are materials with at least one dimension on the scale of sub-100nm. Producing materials in the nano-size regime results in properties different from their bulk counterparts. With an increase in the number of dimensions that are spatially confined, more charge carriers within a semiconductor are confined and the effects of confinement become more evident. Quantum dots belong in the group of 0-D nanomaterials, in which particles exhibit confinement in all three dimensions.[1]

Quantum dots (QDs) exhibit interesting electronic and optical properties due to confinement relative to their bulk counterparts. In order to understand the properties of semiconductor nanomaterials, one must understand the energy band structure of bulk semiconductors, which lies between that of conductors and insulators. The valence and conduction bands overlap in conductors, resulting in highly mobile electron movement, while the valence and conduction bands in insulators are largely offset, resulting in a loss of conduction. Semiconductor materials have a small energy gap between the valence and the conduction bands, also known as the band gap and are, therefore, not always conductive. However, dependent upon the material and therefore the size of the band gap, if enough energy is input into the system, an electron and hole are generated in the valence band and conduction band respectively. As the electron-hole pair approach one another at a distance closer than the Bohr exciton diameter, an exciton pair is generated. The electron orbits

the hole at a distance that balances the Coulombic interaction. This distance is known as the Bohr exciton diameter.[1,2]

Semiconductor nanomaterials gain new properties from their bulk counterparts due to the fact that the size of the material is reduced to less than the Bohr exciton diameter.[3] Therefore, properties of the material are caused not only by the band gap which is dictated by the identity of the material, but also by the size of the particle. The size of a quantum dot constrains the distance of electron-hole pair separation resulting in the increase in the energy required to generate the exciton. From this increase in energy arises size- and shape-tunable absorption and emission properties.

The idea that electronic properties of small materials are different from those of their bulk counterparts was first proposed in 1984 by Louis E. Brus. As the size of semiconductor nanomaterials is decreased below the Bohr exciton diameter, quantization of the band gap energy occurs. With decrease in particle size, the exciton increases in energy of the excite state, which leads to a decrease in wavelength of light absorbed and emitted by the particles. Brus modeled this energy quantization in quantum dots as:

$$E_{ex} = \frac{\hbar^2 \pi^2}{2R^2}\left(\frac{1}{m_e} + \frac{1}{m_h}\right) - \frac{1.8e^2}{\varepsilon_2 R} + \frac{e^2}{R}\overline{\sum_{n=1}^{\infty} \alpha_n \left(\frac{S}{R}\right)^{2n}}$$

in which $\hbar$ is the reduced Planck's constant, R is the radius of the nanocrystal, m_e and m_h are the effective masses of the electron and hole respectively, e is the absolute charge of an electron, ε_2 is the dielectric constant of the semiconductor material, α_n is a constant that relates the dielectric constants of the semiconductor material and the surrounding medium, and S is the wavefunction that describes the position of the electron and hole in the 1S

exciton.[1] The first term of this equation relates to the quantization energy of the electron-hole pair spacing, reminiscent of Schrödinger's particle-in-a-box, in which the length of the box in inversely correlated to the difference in energy levels. The second term relates to the Coulombic attraction of the positive and negative charge carriers. The third term is the perturbation of the electrons around the exciton. The value of the first term is largely affected by the size of the QD due to the presence of the value of the nanocrystal radius in the denominator. As the size of the QD gets smaller, this term will increase resulting in the large observable change in the band gap and therefore changes to QD absorbance and fluorescence as a direct result of the change in size.
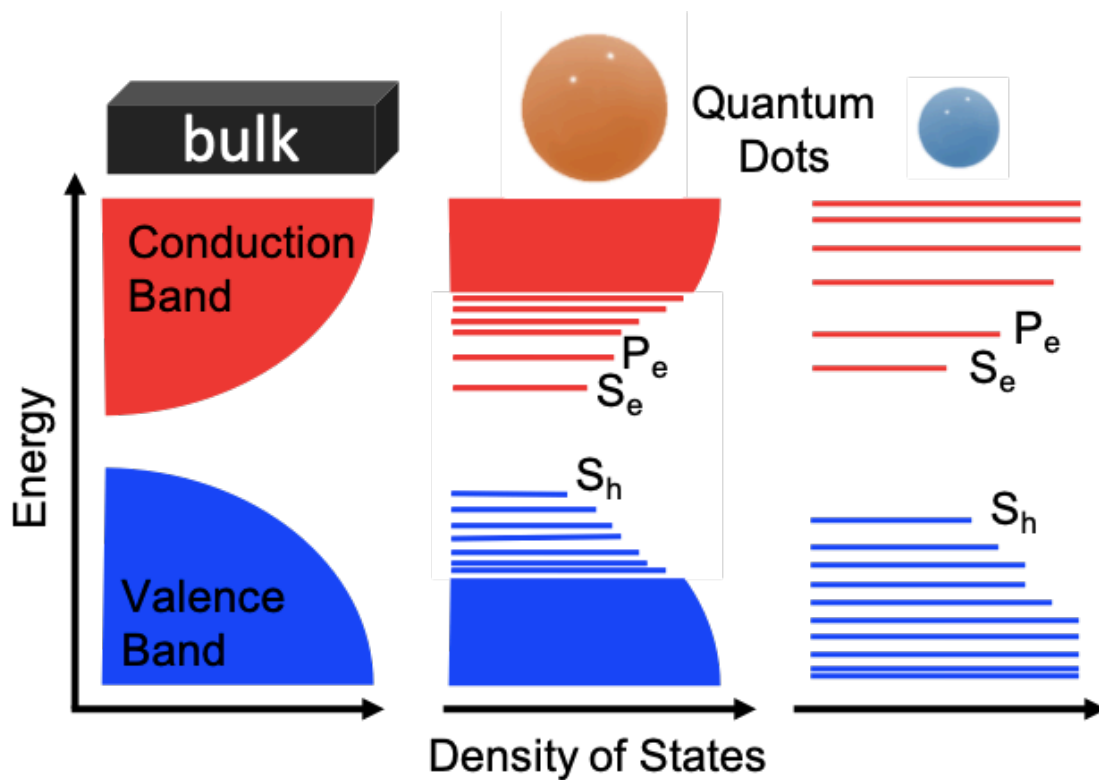
Figure 1.1 As the size of a QD gets smaller, the distance between the conduction band and the valence band, and therefore the band gap, increases.

The introduction of new electronic and optical properties in semiconductor nanomaterials as well as our ability to synthesize QDs with different materials and in different shapes and sizes allows for their use in a broad spectrum of applications. These include but are not limited to lighting, displays, solar cells, solar concentrators, biological labeling, and lasers.[4-18,89-93] Semiconductor nanocrystals can also be easily deposited on a wide variety of substrates, including flexible substrates, through reel-to-reel printing, spray painting, and ink-jet printing allowing for greater use of semiconductors in industrial applications.[9]

Cadmium selenide (CdSe) nanocrystals are ubiquitous in nanoscience and are currently the most thoroughly studied QD system.[84-86] CdSe QDs have been optimized for various applications through changes in shape and size, surface ligands, crystal structure, and various shell materials. Because its Bohr exciton diameter is 11.2 nm, CdSe nanocrystals smaller than 11.2 nm exhibit quantum confinement, resulting in a change in fluorescence with change in size covering the full visible spectrum. Ultrasmall CdSe QDs can also emit white light due to surface state emission.[19-21,87,88]

Figure 1.2 CdSe nanocrystals of various sizes, from ultrasmall white light emitting to 7 nm red emitting QDs, used to demonstrate size-dependent quantum confinement.
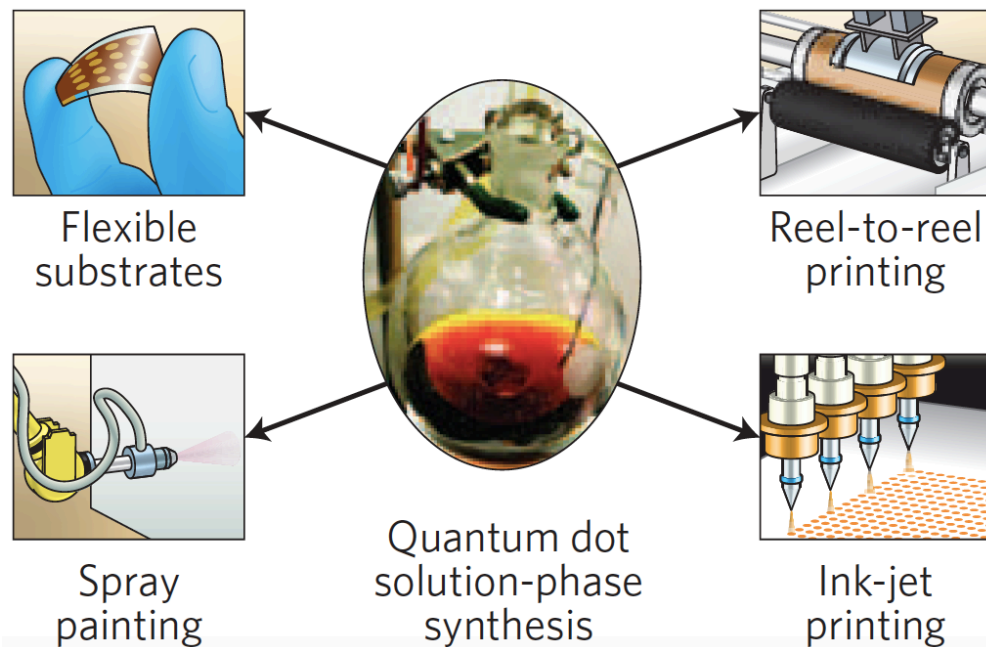
Figure 1.3 Semiconductor nanocrystals are more easily deposited compared to their bulk counterparts on various types of substrates through reel-to-reel printing, spray painting, and ink-jet printing.[9]

While CdSe QDs are largely popular, they are highly toxic[94] due to their heavy-metal composition; therefore, research has shifted to other materials for non-toxic QDs that emit in the visible spectrum for industrial applications.[22,99] Copper-, indium-, and zinc-based semiconductor nanocrystals have been the main focus of these studies due to their size-tunable absorption and emission from quantum confinement.[23-28,95-98] Commercial applications have been developed using these non-toxic QDs, such as Samsung's QLED TVs and Kindle Fire tablets; however, research to improve colloidal and fluorescence stability similar to their CdSe counterparts continues to be of great interest to the research community.

1.2 Ferroelectric Materials

Inducing ferroelectric properties introduces a plethora of applications to the already ever-growing list of quantum dot applications. The ability to change the polarization of ferroelectric materials through electric, thermal, and mechanical energy allows for their use in ferroelectric random access memory, energy harvesters, actuators, transducers, capacitors, and microelectromechanical devices.[29-40,65-76] Change in polarization due to change in mechanical energy results in their inherent piezoelectric properties while change in polarization due to change in thermal energy results in their inherent pyroelectric properties. These piezo- and pyroelectric materials have been used for energy harvesting in roads, floor tiles, shoes, and electronics in order to extend the lifetime for lighting and batteries for electronics. Ferroelectric random access memory (FRAM) uses the positive and negative polarization of ferroelectric materials and assigns them to binary 1s and 0s. The presence of a remnant polarization once the external electric field is removed and the ability to generate memory with only small atomic movements results in fast, non-volatile electronic memory; the best of both worlds from the already existing random access memory (RAM) and

read-only memory (ROM). While FRAM already exists, it is very expensive to synthesize in bulk; therefore, synthesizing nano-ferroelectrics would allow for the use of this remarkable technology in industry.[30,41]

Ferroelectric properties arise due to the presence of a non-centrosymmetric crystal structure with a permanent dipole that is reversible with the addition of an electric field. Due to the fact that all crystal classes with a non-centrosymmetric crystal structure are piezoelectric, all ferroelectrics are inherently piezoelectric. All ferroelectrics are also inherently pyroelectric, because non-centrosymmetric crystal structures with a permanent dipole moment exhibit pyroelectric properties. Therefore, in ferroelectric crystal structures, we have the ability to change the polarization of the material through changes in electric, thermal, and mechanical energy. When applying a positive or negative external electric field, ferroelectrics generate a positive or negative saturation polarization. Once the external electric field is removed, ferroelectrics require less energy to settle in either a slightly positive or slightly negative remnant polarization than in a zero polarization. The point at which a positive or negative applied electric field results in a net polarization of zero is called the coercive field, at which the numbers of positive and negative domains within the crystal structure are equal.[37-40]
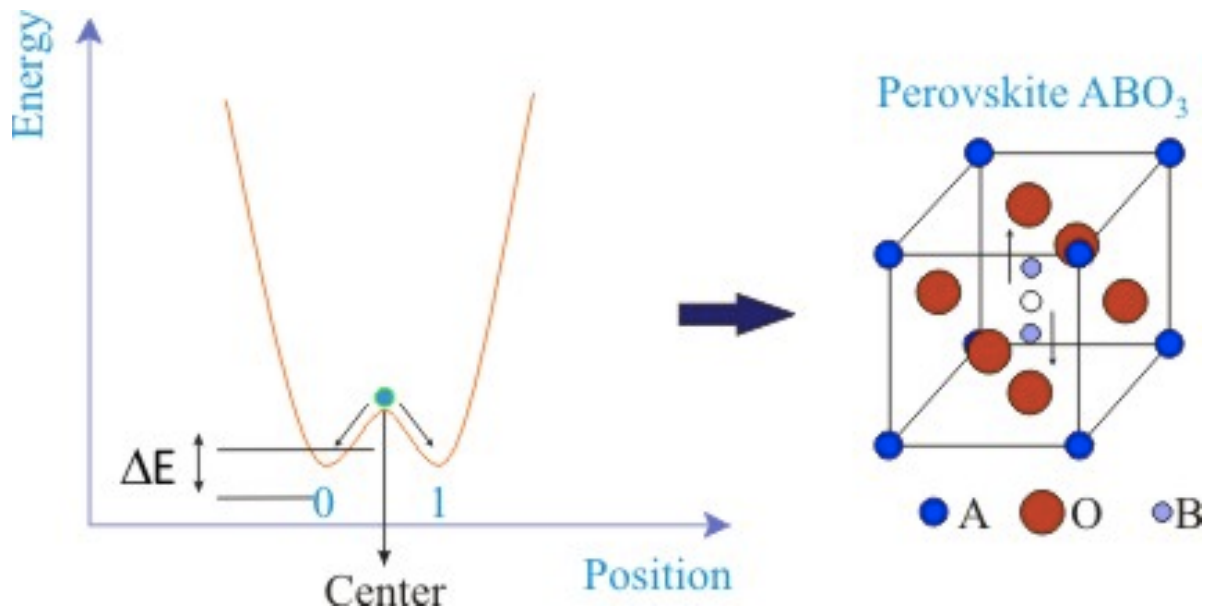
Figure 1.4 Once an external electric field is removed, ferroelectrics require less energy to settle in a positive or negative position remnant polarization rather than a zero polarization. Above is an example of a perovskite, tetragonal crystal structure, in which the central atom naturally rests, not in the center, but in a positive or negative position.

The most commonly referenced nano-ferroelectric material is barium titanate ($BaTiO_3$), which has a perovskite crystal structure and has been utilized in capacitors and data-storage devices. Bulk $BaTiO_3$ has been prepared by glycothermal and hydrothermal syntheses, while nanoscale $BaTiO_3$ has been synthesized by glycothermal treatment. A negative aspect of this material is the dependence of its ferroelectric response on size. Specifically, as the diameter for $BaTiO_3$ is reduced to about 10-30 nm, the crystal structure has been observed to shift from a tetragonal to a cubic phase, which are non-centrosymmetric and centrosymmetric respectively.[42-46,77-80] This shift results in the loss of ferroelectric properties with decrease in size. This highlights the importance of maintaining the crystal framework at the nanoscale in order to retain ferroelectric behavior. While other nano-ferroelectrics have been studied alongside $BaTiO_3$, they often require more complex synthetic techniques, which include nano-imprint lithography, sol-gel methods, or template

directed bottom-up synthesis.[47] Pre-synthesizing nanocrystals and inducing ferroelectricity

through a simple cation exchange reaction is a simple solution to the loss of ferroelectricity due to

crystal structure changes with decrease in size.
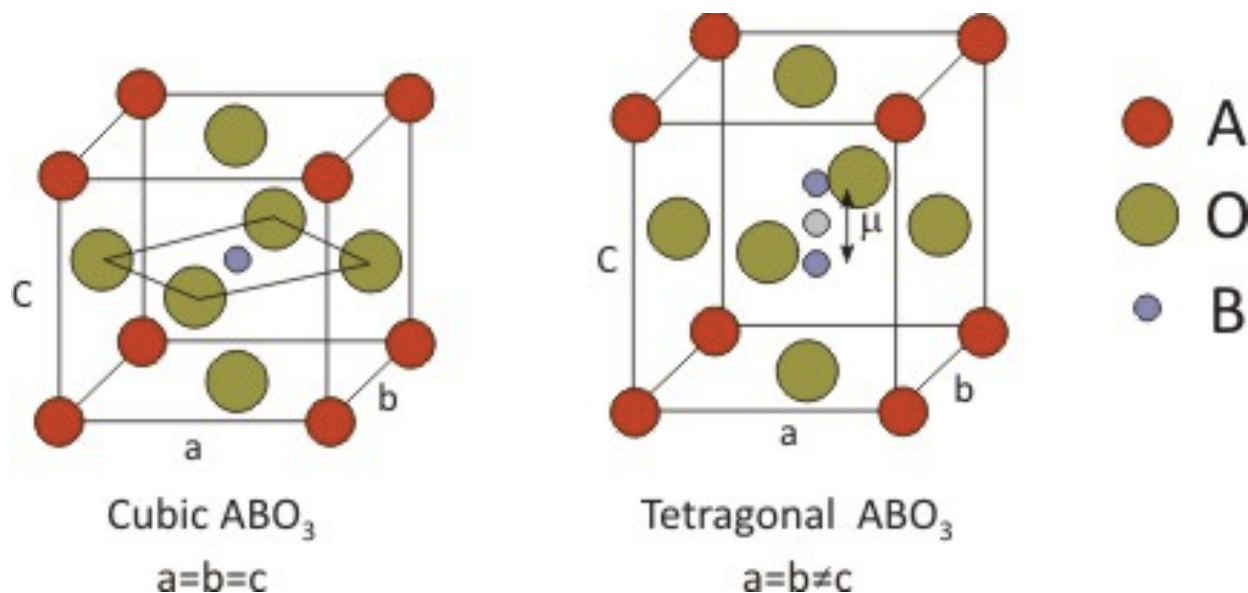
Figure 1.5 A cubic crystal structure is centrosymmetric and therefore not ferroelectric, while a tetragonal crystal structure is non-centrosymmetric and therefore ferroelectric due to the positive or negative position of the central atom.

Dr. Toshia Wrenn discovered the emergence of ferroelectric properties due to a room-temperature

cation exchange when studying the effects of doping semiconductor nanocrystals with antimony.

Rather than exhibiting typical doping effects that occur in bulk semiconductors, the nanoparticles

flocculated and were attracted to a van der Graaf generator wand that produced an external electric

field. In this synthesis, percent cation exchange and therefore ferroelectric saturation polarization

was controlled by the time at which the reaction was allowed to occur. Saturation polarization was

optimized at about 12h and quantitative ferroelectric analysis was performed using a Sawyer-

Tower circuit while elemental analysis was performed through STEM-EDS.[48]
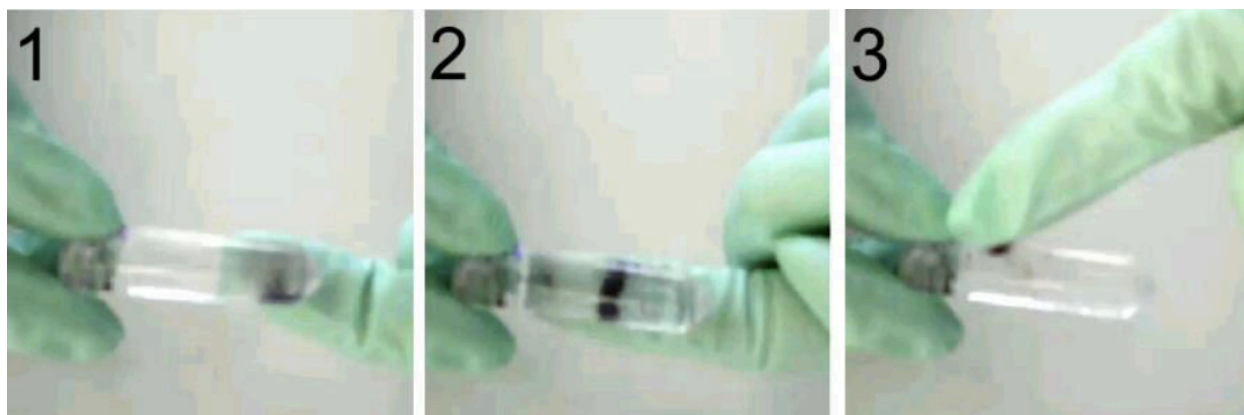
Figure 1.6 Qualitative demonstration of ferroelectricity in which antimony-treated QDs react to an external electric field produced by a finger.[48]

1.3 Overview

This work looks at the optimization of the synthesis of ferroelectric semiconductor nanocrystals through cation exchange. Chapter 2 discusses the experimental techniques used in the work covering various nanoparticle syntheses, cation exchange, and optical, visual, and electronic characterizations. Chapter 3 covers the optimization of ferroelectric properties through variations in the cation exchange synthesis. The identity of the cations and the concentration of the metal chloride salt solutions used in cation exchange were varied in order to optimize saturation and remnant polarization as well as crystal structure retention. Chapter 4 discusses the removal of byproducts through small changes in the cation exchange synthesis as well as the retention of colloidal stability through ligand exchange. Chapter 5 discusses fluorescence retention through performing cation exchange reaction in a protective CdS shell in order to prevent defects within the fluorescent CdSe core. Chapter 6 examines non-toxic alternatives that allow for the use of ferroelectric quantum dots in industrial applications. Chapter 7 reflects on this work and provides thoughts on the implementation of the ideas learned in this work in InP/ZnSe systems for the formation of non-toxic, fluorescent, ferroelectric semiconductor nanocrystals.

CHAPTER II

EXPERIMENTAL

2.1 Ferroelectric Optimization through Variation in Exchange Cation Solution

2.1.1 Synthesis of CdS$_x$Se$_{1-x}$ alloyed QDs

The synthesis of the CdS$_x$Se$_{1-x}$ alloyed QDs was based on the syntheses of Aubert, Keene, and Harrison.[49-51] Sulfur and selenium precursor solutions with 1 M concentrations were prepared beforehand. The sulfur precursor was obtained by mixing 0.32 g of sulfur in 10 mL of octadecene (ODE). The solution was purged with argon for 15 min; then, the solution was heated with a heat gun until the sulfur dissolved completely. The selenium precursor was obtained by mixing 0.79 g of selenium powder in 10 mL of ODE. The solution was purged with argon for 15 min and shaken vigorously to disperse the powder just before injection. For the synthesis of the CdS$_{0.7}$Se$_{0.3}$ alloyed QDs, 0.39 g of cadmium oxide was mixed with 2.06 g of myristic acid (MA) in 30 mL of ODE. The solution was placed in a 100 mL three-neck round-bottom flask equipped with a bump trap and a temperature probe. The reaction was purged with argon and heated to 270 °C, with a purge needle inserted until the reaction temperature reached 130 °C to release water generated from the reaction. Once the reaction reached 270 °C and the solution became completely colorless, 3 mL of 7:3 sulfur/selenium precursor solution was injected and the temperature was lowered to 260 °C. The crystals were allowed to grow for 2 hours and quenched by removing from heat and cooling

the flask with compressed air. The QDs were precipitated by an addition of isopropanol and centrifuged for 5 min at 7500 rpm. The QDs were then re-dispersed in toluene and the MA on their surface was exchanged by the addition of a 10-fold excess of oleic acid (OA). Purification was repeated three times with toluene and ethanol as the solvent and antisolvent, respectively. The resulting CdSSe nanoparticles were primarily a zinc blende crystal structure.

2.1.2 Cation Exchange with Various Metal Chloride Salts

This CdSSe cation exchange synthesis of the ferroelectric nanoparticles was based on the previously reported Wrenn *et al*. cation exchange synthesis on CdSe nanocrystals of the same crystal structure with adjustments made to solvents, concentrations, and cations used.[48] In order to avoid precipitation of cadmium chloride hydrate byproducts during cation exchange, the salts were dissolved in ethanol instead of toluene to form metal chloride precursors. The 2.5 mM antimony(III) chloride precursor was obtained by dissolving the $SbCl_3$ salt in 25 mL of ethanol in a glass vial and shaking until fully dissolved. Finally, the previously synthesized QDs were diluted to 0.45 mM in toluene and 1 mL of this solution was injected into the vial containing the salt−ethanol solution and shaken to mix. The cation exchange reaction was allowed to occur for 24 hours, then the vials were centrifuged for 3 minutes at 3000 rpm, and the supernatant was decanted. This synthesis was also carried out using 2.5 mM tin(II) chloride, gold(III) chloride, and tin(IV) chloride solutions in ethanol as well as tin(IV) chloride solutions of varying concentrations from 1.5 mM to 20 mM.

2.2 Fluorescence Retention

2.2.1 CdSe Nanoparticle Synthesis

The synthesis of the CdSe zinc blende QDs was based on the synthesis of Shen *et al*.[52] The selenium precursor solution was prepared beforehand by combining 15 mg of selenium and 3 mL of ODE. The solution was purged with argon for 15 minutes then shaken vigorously to disperse the powder before injection. For the synthesis of CdSe QDs, 26 mg of CdO was mixed with 3 mL of OA and 3 mL of ODE. The solution was placed in a 50 mL three-neck round-bottom flask equipped with a bump trap and a temperature probe. The reaction was purged with argon and heated to 270°C, with a purge needle inserted until the reaction temperature reached 130°C to release water generated from the reaction. Once the reaction reached 270°C and the solution became completely colorless, the selenium precursor solution was injected and the temperature was lowered to 250°C. The crystals were allowed to grow for 3 minutes and quenched by removing from heat and cooling the flask with compressed air. The QDs were precipitated by an addition of a 1:1 ethanol/acetone mixture and centrifuged for 5 min at 7500 rpm. Purification was repeated three times with toluene and ethanol as the solvent and antisolvent respectively. The final, washed CdSe nanoparticles were redispersed in toluene.

2.2.2 CdSe/CdS core-shell synthesis

The synthesis of core-shell CdSe/nCdS QDs through the SILAR approach was based on the syntheses of Peng and Hollingsworth.[53,54] Cadmium oleate and sulfur precursor solutions with 0.2 M concentrations were prepared beforehand. The Cd-oleate precursor was prepared by mixing 2 mmol of both CdO and oleic acid in 10 mL of ODE. The solution was purged with argon and

heated to 250°C while stirring until the CdO dissolved and the solution became colorless. The sulfur solution was prepared by mixing 2 mmol of sulfur and 10 mL of ODE. The solution was purged with argon for 15 min and heated with a heat gun until the sulfur dissolved completely. The quantity of precursors for growing each monolayer of shell was calculated using the procedure by Hollingsworth et al. A 100 mL three-neck round-bottom flask equipped with a bump trap and a temperature probe was loaded with 1.5 g of octadecylamine (ODA) and 10 mL of ODE and purged with argon at 150°C for one hour. The flask was injected with $\sim 1 \times 10^{-5}$ mol of washed 4.5 nm CdSe cores and purged again with argon for 30 min. The purge needle was removed and the solution temperature was increased to 245°C. Growth times were 1 h following each sulfur addition and 3 h following each cadmium addition. Once the desired shell thickness was achieved, the reaction was quenched by removing heat and cooling the flask with compressed air. The resulting QDs were precipitated by the addition of acetone and centrifuged for 5 min at 7500 rpm. Purification was repeated three times with toluene and acetone as the solvent and antisolvent respectively. The final, washed CdSe/CdS core-shell nanoparticles were redispersed in toluene.

2.2.3 Cation Exchange

The cation exchange synthesis of zinc blende ferroelectric nanoparticles was based on the previously reported Bradsher, Wrenn, and Rosenthal cation exchange syntheses on CdSe QD and $CdS_{0.7}Se_{0.3}$ alloyed QD.[48,55] The 2.5 mM tin(IV) chloride precursor was obtained by dissolving $SnCl_4$ in 25 mL of ethanol in a glass vial and shaking until fully dissolved. Synthesized CdSe and CdSe/CdS QDs were diluted to 0.45 mM in toluene and 1 mL of this solution was injected into the vial containing the $SnCl_4$-ethanol solution and shaken to mix. The cation exchange reaction was allowed to occur for 24 h, then the vials were centrifuged for 3 min at 3000 rpm, and the

supernatant was decanted. The ferroelectric QDs were then redispersed in toluene and the aggregation due to ligand displacement by chlorine was reversed by the addition of a 10-fold excess of TOP. The TOP-capped ferroelectric QDs precipitated by an addition of a 9:1 acetone/ethanol mixture and centrifuged for 3 min at 3000 rpm. Purification was repeated three times with toluene and ethanol as the solvent and antisolvent respectively. The final, washed TOP-capped ferroelectric QDs were redispersed in toluene.

2.3 Non-toxic Ferroelectric Semiconductor Nanoparticles

2.3.1 ZnSe Nanoparticle Synthesis

The synthesis of zinc blende ZnSe QDs was based on the synthesis of O'Brien.[56] A 100 mL three-neck round-bottom flask was loaded with 0.4 mmol of zinc-stearate, 0.4 mmol of selenium, and 26 mL of ODE. The reaction was purged with argon and heated to 295°C, with a purge needle inserted until the reaction temperature reached 130°C to release water generated from the reaction. Once the reaction reached 295°C the QDs were allowed to grow for 1 h. The QDs were precipitated by an addition of a 9:1 acetone/methanol mixture and centrifuged for 5 min at 7500 rpm. Purification was repeated three times with toluene and methanol as the solvent and antisolvent respectively. The final, washed ZnSe nanoparticles were redispersed in toluene.

2.3.2 Cation Exchange

The cation exchange synthesis of zinc blende ferroelectric nanoparticles was based on the previously reported Bradsher, Wrenn, and Rosenthal cation exchange syntheses on CdSe QD and $CdS_{0.7}Se_{0.3}$ alloyed QD.[28,55] The 2.5 mM tin(IV) chloride precursor was obtained by dissolving

SnCl$_4$ in 25 mL of ethanol in a glass vial and shaking until fully dissolved. Synthesized ZnSe QDs were diluted to 0.45 mM in toluene and 1 mL of this solution was injected into the vial containing the SnCl$_4$-ethanol solution and shaken to mix. The cation exchange reaction was allowed to occur for 24 h, then the vials were centrifuged for 3 min at 3000 rpm, and the supernatant was decanted. The ferroelectric QDs were then redispersed in toluene and the aggregation due to ligand displacement by chlorine was reversed by the addition of a 10-fold excess of TOP. The TOP-capped ferroelectric QDs precipitated by an addition of a 9:1 acetone/ethanol mixture and centrifuged for 3 min at 3000 rpm. Purification was repeated three times with toluene and ethanol as the solvent and antisolvent respectively. The final, washed TOP-capped ferroelectric QDs were redispersed in toluene.

2.4 Characterization

Thorough characterization of ferroelectric QDs was performed to analyze their photophysical properties, size, shape, elemental composition, crystal structure, and ferroelectric properties. Absorption and emission measurements provide information about QD size, color, and fluorescence quantum yield. Transmission electron microscopy and energy dispersive x-ray spectroscopy allows for analysis of size, shape, structure, monodispersity, and composition of QDs. X-ray diffraction provides information on crystal structure and disorder within the crystal. A Sawyer-Tower circuit allows for quantitative analysis of ferroelectric properties of the overall QD samples.

2.4.1 Static Optical Absorption and Emission

All synthesized QDs are initially characterized using static optical absorption and photoluminescence to determine the band gap and emission wavelength. For the more well-studied QD systems, such as CdSe, sizing curves have been developed that allow for the size of the nanocrystals to be determined just from absorption data.[57] Additionally, the sample's optical density determines how much light is being absorbed by the QDs at a specific wavelength. Absorption spectra were obtained using a Varian Cary 50 UV-Vis spectrophotometer and photoluminescence spectra were obtained with an ISS PC1 Photon Counting Spectrofluorimeter or a Photon Technology International QuantaMaster 40.

2.4.2 Photoluminescence Quantum Yield

Photoluminescence quantum yield (PLQY) is a measurement of quantum dot efficiency and therefore their brightness. Higher PLQY means more efficient radiative recombination of charge carriers. Explicitly, PLQY measures the ratio of photons absorbed by the QD to photons emitted:

$$PLQY = \frac{\#\ photons\ emitted}{\#\ photons\ absorbed}\ x\ 100\ \%$$

Measurements were taken using the single point calibration method using a laser dye (typically rhodamine 6G) which have a known PLQY. The absorbance of both the QDs and the reference dye were obtained at the excitation wavelength using a Varian Cary 50 UV-Vis spectrophotometer to ensure both had an optical density between 0.09 and 0.1. Their fluorescence was then obtained with a Photon Technology International QuantaMaster 40 and the area under the curve integrated. The QD sample's PLQY is then determined with the following equation:

$$PLQY = Q_R \frac{I}{I_R} \frac{OD_R}{OD} \frac{n^2}{n_R^2}$$

Where the subscript R is associated with values for the reference dye, I is the integrated fluorescence intensity, OD is the optical density or absorbance of the sample at the excitation wavelength, and n is the refractive index of the solvent.[58]

2.4.3 Transmission Electron Microscopy and Energy Dispersive X-ray Spectroscopy

High-resolution transmission electron microscopy (TEM) and scanning transmission electron microscopy with energy dispersive spectroscopy (STEM-EDS) images were taken on a FEI Tecnai Osiris transmission electron microscope operating at 200 keV. TEM allows for analysis of size and shape of the QDs as well as monodispersity. EDS provides information provides information on QD composition through x-rays that are given off by the QDs after their interaction with electrons in the TEM. The Tecnai Osiris is equipped with ChemiSTEM technology to perform elemental mapping through STEM-EDS on the nanoscale. EDS spectra were analyzed quantitatively using Bruker Espirit 1.9 software. To determine the average diameter of a sample of nanocrystals, 100–200 of the imaged nanocrystals were measured along long axis using ImageJ.[59] Samples were prepared by placing a drop of nanocrystals diluted in toluene to an optical density of <0.1 onto an ultrathin carbon supported by a Lacey carbon film on a 400-mesh copper TEM grid (Ted Pella, Inc.), wicking away any excess solvent.

2.4.4 X-ray Diffraction

X-ray diffraction (XRD) allows for analysis of crystal structure of the overall QD sample as well as crystal structure retention before and after cation exchange. XRD scans were obtained using a Rigaku SmartLab X-ray diffractometer with a Cu source (λ = 1.54056 Å), D/teX Ultra 250, and an amorphous glass sample support, using a step-size of 0.1° and scan speed of 1°/min.

2.4.5 Sawyer-Tower Circuit

A Sawyer-Tower circuit provides quantitative information about the saturation polarization, remnant polarization, and coercive field of the overall QD sample. Polarization response was measured utilizing a sandwich cell consisting of two indium tin oxide-coated glass slides separated by a 180 μm spacer with an active area of 1 cm^2, compressed around a concentrated paste of particles in ethanol and dried with a heat gun to remove the solvent and seal the system. The sandwich cells were connected to a traditional Sawyer-Tower circuit, consisting of a Tektronix AFG 3021C function generator and a Tektronix DPO 3034 oscilloscope. A triangular waveform of ±10 V was applied to the circuit and the voltage input and the voltage drop across a 10 μF reference capacitor in series with the cell were used to determine the polarization and electric field across the samples.[60,61]
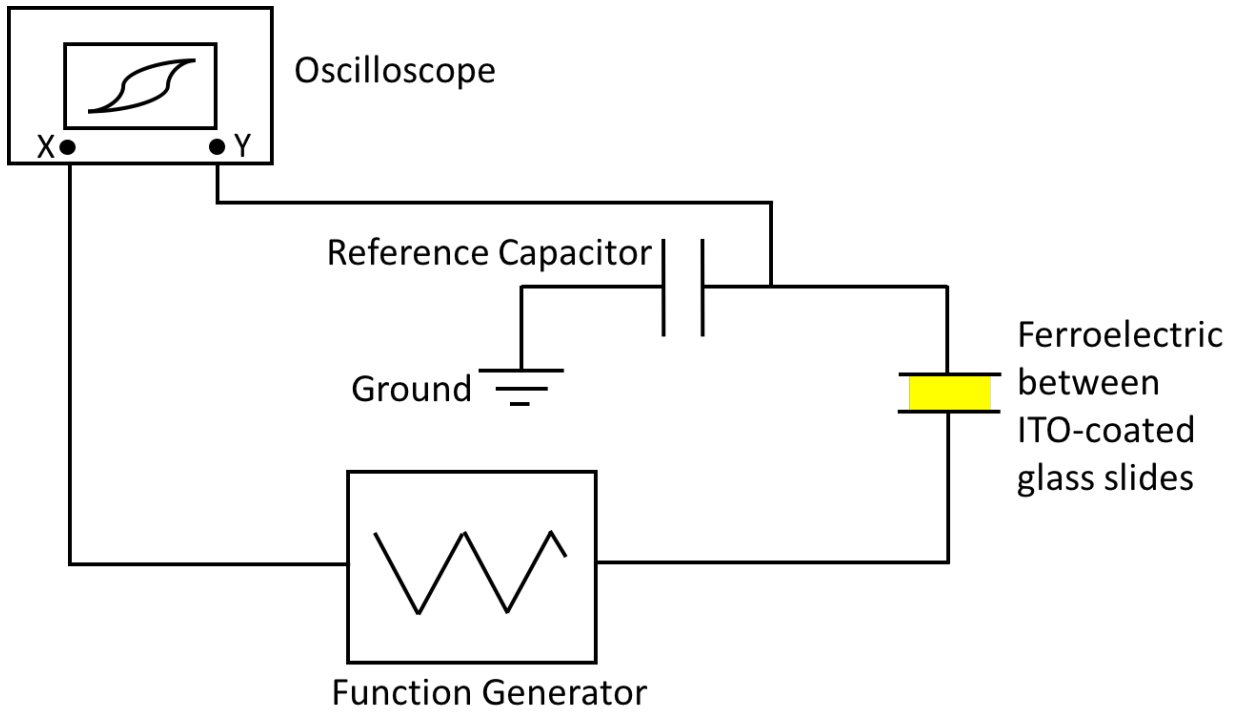
Figure 2.1 Diagram of a Sawyer-Tower circuit consisting of a function generator, an oscilloscope, a reference capacitor, and a ferroelectric sample sandwiched between two indium tin oxide-coated glass slides.
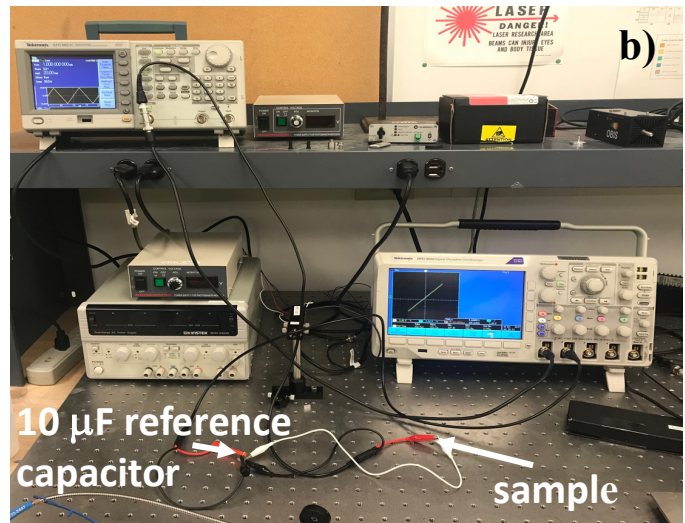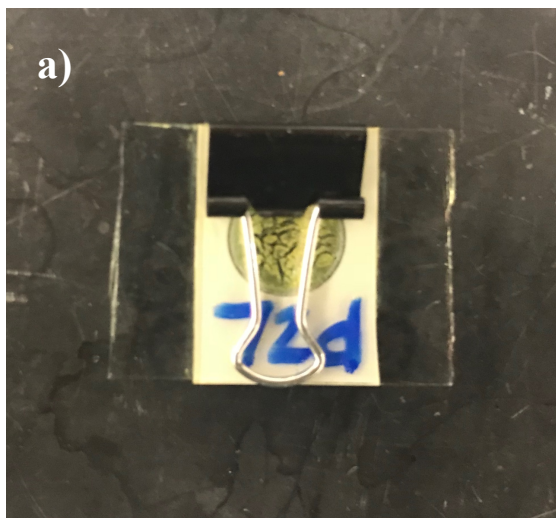

Figure 2.2 a) A ferroelectric sample sandwiched between two ITO-coated glass slides and b) the Sawyer-Tower circuit used to measure quantitative ferroelectric properties.

MODULATING FERROELECTRIC RESPONSE THROUGH CATION EXCHANGE

3.1 Introduction

Cadmium selenide and cadmium sulfide nanocrystals can be synthesized in either zinc blende or wurtzite crystal structures. Materials with a zinc blende crystal structure, which belong to the crystal class $\bar{4}3m$, are non-centrosymmetric and therefore piezoelectric. Zinc blende nanocrystals, while non-centrosymmetric, are neither pyroelectric nor ferroelectric due to the lack of a permanent dipole. Wurtzite materials belong to the 6mm crystal class and are non-centrosymmetric with a permanent dipole resulting in the inherent pyroelectric properties.[62] The main focus of this research is conducted on nanocrystals with a zinc blende crystal structure.

With the occurrence of cation exchange within this crystal structure, ferroelectric properties emerge due to the formation of a dipole because of a difference in cation electronegativity. Dissimilarity in electronegativity between the exchanged cation and the native cadmium creates small atomic displacements in the crystal structure, yielding permanent dipoles throughout the crystal structure at each substitution point. With the introduction of an electric field, these structure-induced dipoles can be polarized, aligning all of the small atomic displacements within the crystal. Cation exchange performed at room temperature with metal chloride salts of various sizes and identities revealed this effect. Differences in charge between cadmium and the exchanged cations causes the formation of localized permanent dipoles, resulting in the emergence of pyroelectric properties, as anions and cations shift within the crystal structure to compensate for the changed electrostatic attraction and repulsion. Ferroelectric response of the particles under an

applied field also emerges depending on the number of localized permanent dipoles, or the amount of cations exchanged, as well as the strength of the changed electrostatic attraction between cations and anions, or the difference in electronegativity and charge between the native cadmium and exchanged cations.
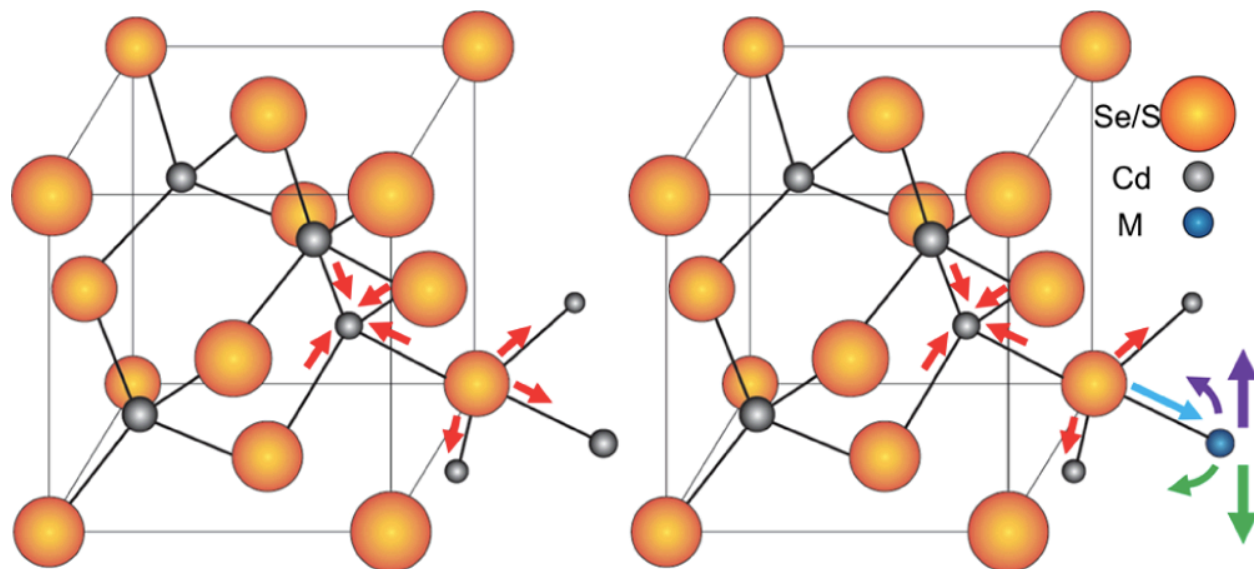
Figure 3.1 Structural depiction of cation exchange (right). With difference in the charge and electronegativity between the exchanged cation and the native cadmium within the zinc blende crystal structure, the remaining cadmium cations are repulsed by the cations exchanged. Cation movement (small purple and green arrows) because of this repulsion can occur in two directions, which can be affected by an applied electric field (large purple and green arrows). Similar but inverted distortions are expected for the anions around the exchanged cation (not shown). Dipoles (red and blue arrows) cancel in the original crystal structure (left), but a permanent dipole is formed through cation exchange (right).

3.2 Dependence of Ferroelectric Response on Cation Identity

Cation exchange syntheses were performed using various metal chloride salts including antimony (III) chloride, which was used in Dr. Wrenn's original synthesis, as well as tin (II) chloride, gold (III) chloride, and tin (IV) chloride. Aggregation occurred due to displacement of oleic acid ligands by chlorine anions. Subsequently, cation exchange took place between the metal cation and the

native cadmium in the original QDs, as shown through STEM-EDS imaging in Figure 3.2.[63] TEM

images and EDS spectra as well as XRD of QD aggregates after each cation exchange reaction

were also analyzed.

Figure 3.2 STEM−EDS maps of CdSSe nanocrystals after undergoing partial cation exchange with tin(II), antimony(III), gold(III), and tin(IV). Chlorine was present in all samples because of particle surface ligand displacement by the chlorine anions from the salts used in the cation exchange process.
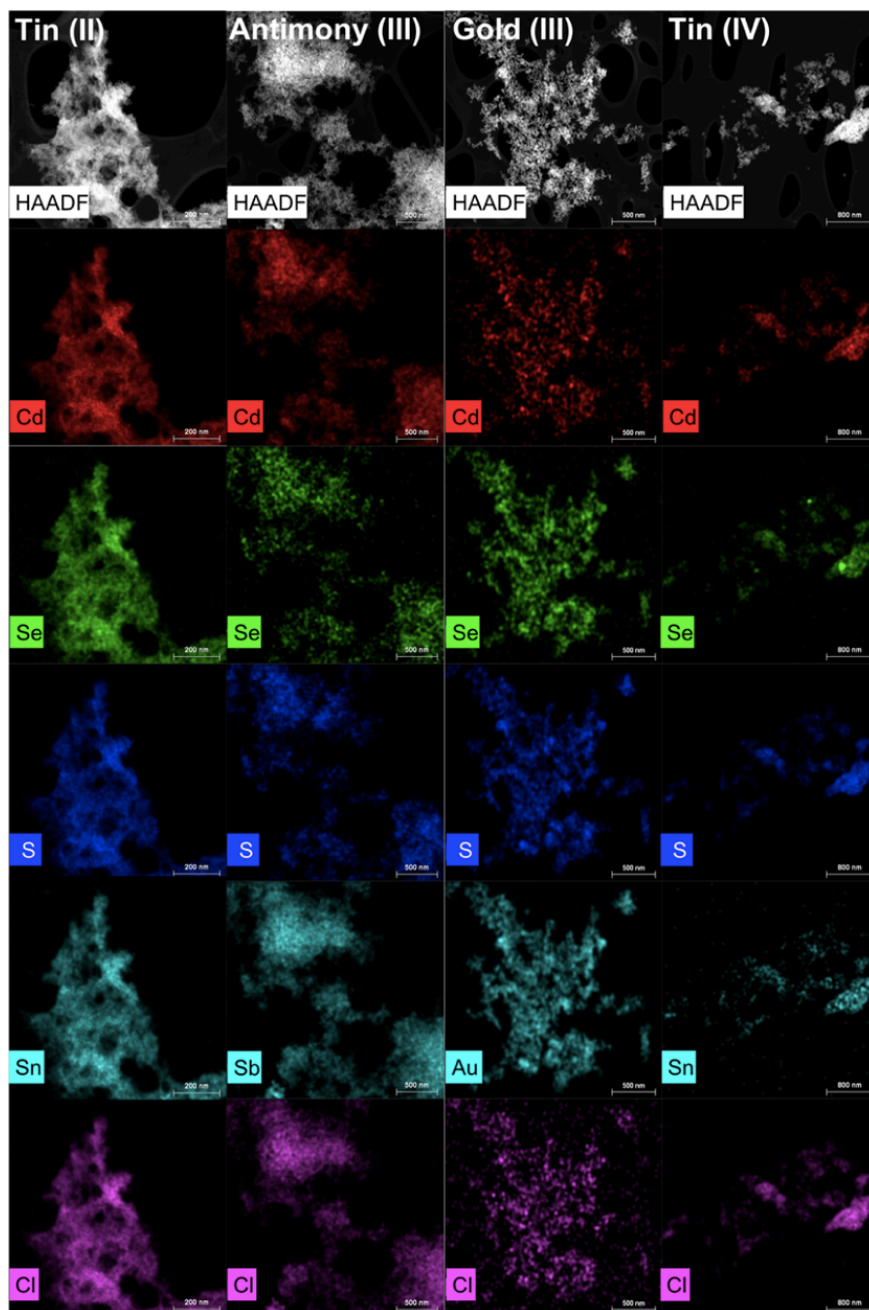
Ferroelectricity emerged with each cation exchange reaction; however, remnant and saturation polarization values varied. These values were compared to a control sample of CdSSe before cation exchange. The particles' ferroelectric properties were analyzed qualitatively using a small Van der Graaff generator as well as quantitatively using a Sawyer-Tower circuit. Under the small electric field generated by the hand-held Van der Graaff generator, the particles in solution begin to move, much like magnetic nanoparticles do under a magnetic field.

Saturation polarization and remnant polarization, as measured with the Sawyer-Tower circuit, increased with cation charge, as shown in Figure 3.3. This is likely because of the differences in electronegativity between the exchanged cation and the native cadmium. The Mulliken equation for electronegativity is used to determine the electronegativity of each cation where χ is the electronegativity, E_I is the ionization energy (kJ/mol), and E_{ea} is the electron affinity (kJ/mol). This equation allows for differentiation between the same elements with different oxidation states, for example, tin (II) and tin (IV), because of its inclusion of ionizaiton energy values.

$$\chi_{Mulliken} = (1.97 \times 10^{-3})(E_I + E_{ea}) + 0.19$$
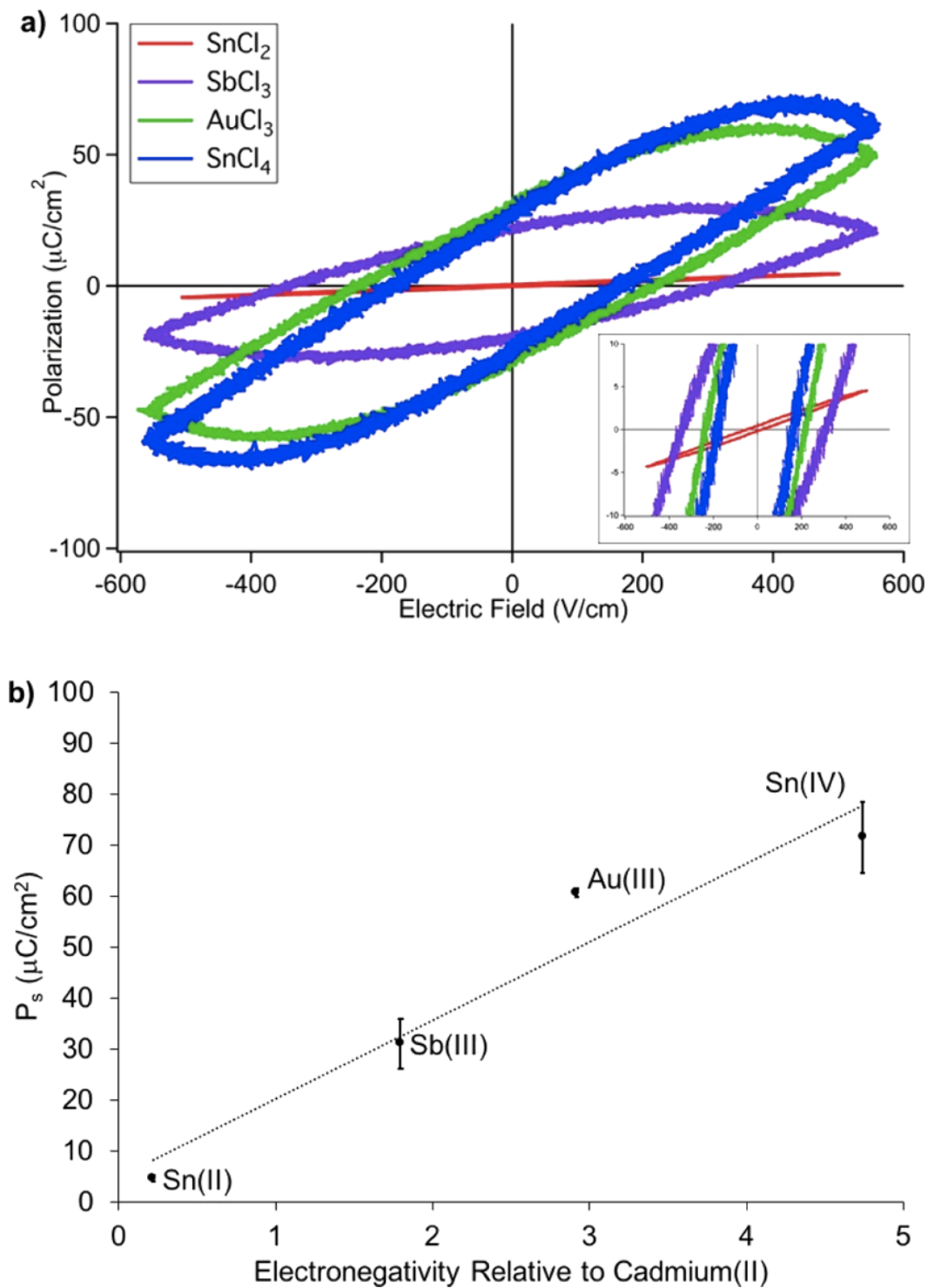
Figure 3.3 a) Polarization responses within an applied electric field for CdSSe QDs treated with various metal chloride salts (SnCl$_2$, SbCl$_3$, AuCl$_3$, and SnCl$_4$). A Sawyer-Tower circuit was used to quantitatively measure polarization from ferroelectric nanoparticles. b) Saturation polarization dependence on electronegativity of the cation relative to cadmium. Electronegativity values were calculated using the Mulliken equation for electronegativity.

When applying this equation for electronegativity values of each cation, a positive trend between electronegativity and saturation polarization values emerges, as shown in Figure 3.3b (Sawyer-Tower circuit measurements were performed at a higher sensitivity to improve signal to noise for the $SnCl_2$ cation exchange sample). The increase in saturation polarization is due to an increased attraction between the anions making up the backbone of the crystal structure and the exchanged cations within the tetrahedral holes, causing increased distortion within the crystal structure and generating a larger ferroelectric response. The size of the cations used in the cation exchange syntheses decreases with increase in electronegativity.[64]

3.3 Dependence of Ferroelectric Response on Exchange Cation Concentration

Up to this point, the dependence of saturation and remnant polarization on reaction time and cation identity has been determined. In order to further understand the role of concentration in the formation of ferroelectric nanocrystals through cation exchange, the degree of ferroelectric response was measured as a function of the concentration of tin (IV) chloride. Tin (IV) chloride was chosen because it gave the highest saturation polarization values compared to the other cations analyzed. The percentage of cations exchanged in the cation identity studies was around 40% for each exchanged cation relative to the original cadmium using the original synthesis at which the metal chloride solution was a concentration of 2.5 mM. The percentage of cations exchanged in the particles for concentration studies was controlled between 30% and nearly 100% as measured by quantitative STEM-EDS (Figure 3.4) by increasing the concentration of the tin (IV) chloride solution employed. Near complete exchange was achieved by using the highest concentration solution employed (20 mM $SnCl_4$) and adding a heating step at 78ºC for 2 hours (Figure 3.4a). The ferroelectric characteristics of the resulting particles were measured using a Sawyer-Tower circuit.
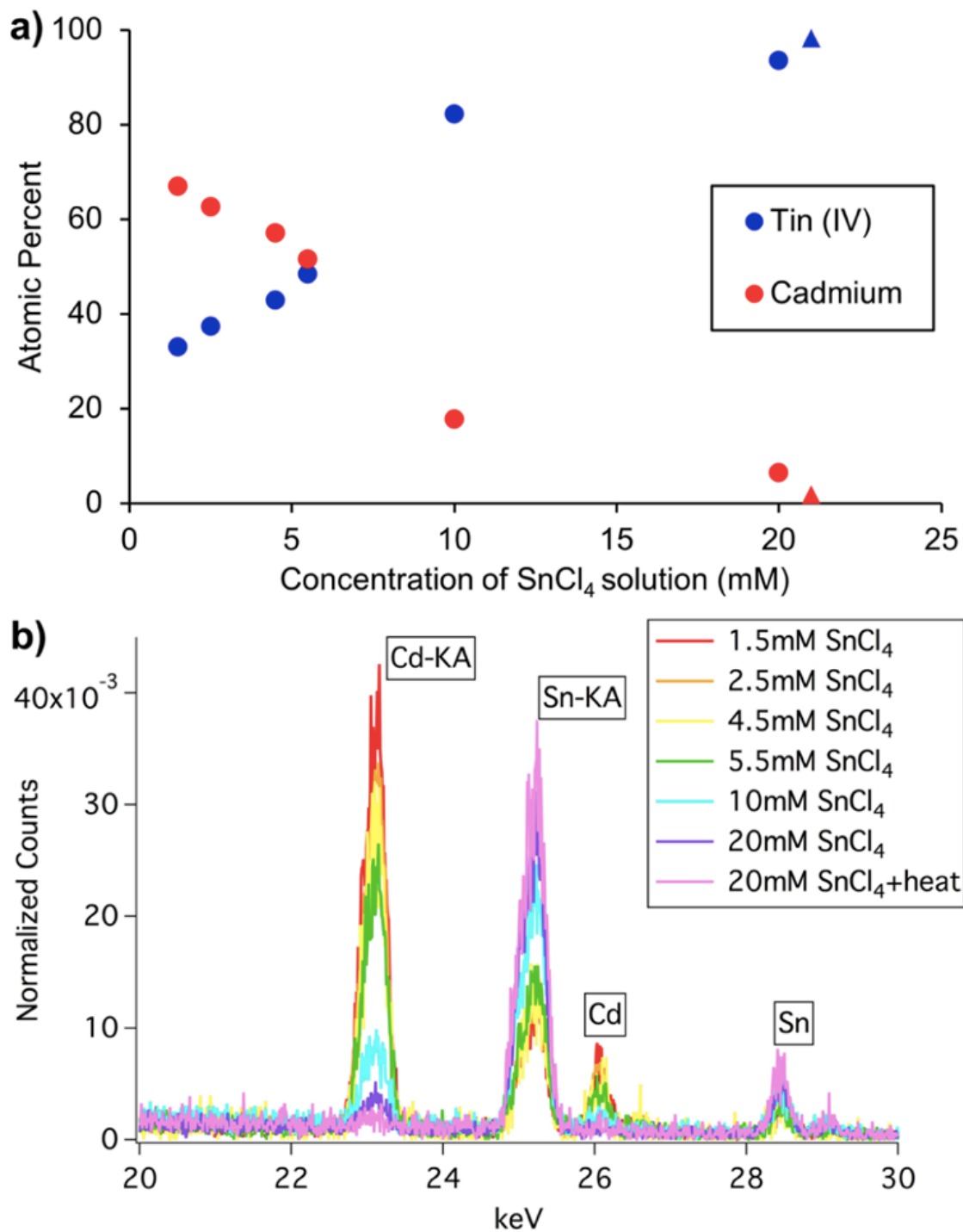
Figure 3.4 a) Dependence of atomic percent ratio of cations exchanged and cadmium on the concentration of the SnCl$_4$ solution used in room temperature cation exchange reactions as determined by b) quantitative STEM−EDS. The cation exchange reaction denoted by triangles was performed using an alternate procedure in order to allow for a near total cation exchange. The SnCl$_4$ and CdSSe mixture was heated to 78 °C for 2 h before allowing to sit for 24 h. All other exchanges took place entirely at room temperature.

It was hypothesized that with an increase in the ratio of tin (IV) exchanged for the native cadmium (II), that the saturation polarization values would increase as well. However, the series of ferroelectric hysteresis curves of the particles in figure 3.5 show that rather than a consistent increase in ferroelectric polarization values with an increased degree of exchanges, the saturation polarization rose as expected until the tin/cadmium ratio reached about 1:1, at which point the sample, like the original CdSSe nanoparticles, and gave a dielectric response. This is likely the result of a cancellation of dipoles within the zinc blende crystal structure (Figure 3.6). With a continued increase in the concentration of the $SnCl_4$ salt solution, the ferroelectric response returned and continued to increase as expected as the ratio of tin/cadmium exceeded 1:1 until the tin (IV) atomic percent reached near 100%, at which point a dielectric response occurred once more due to a cancellation of dipoles (Figure 3.6) as the crystal structure returns to that of the original QDs. Another possible cause of the loss of ferroelectric response is due to crystal structure disorder, shown in Figure 3.7.
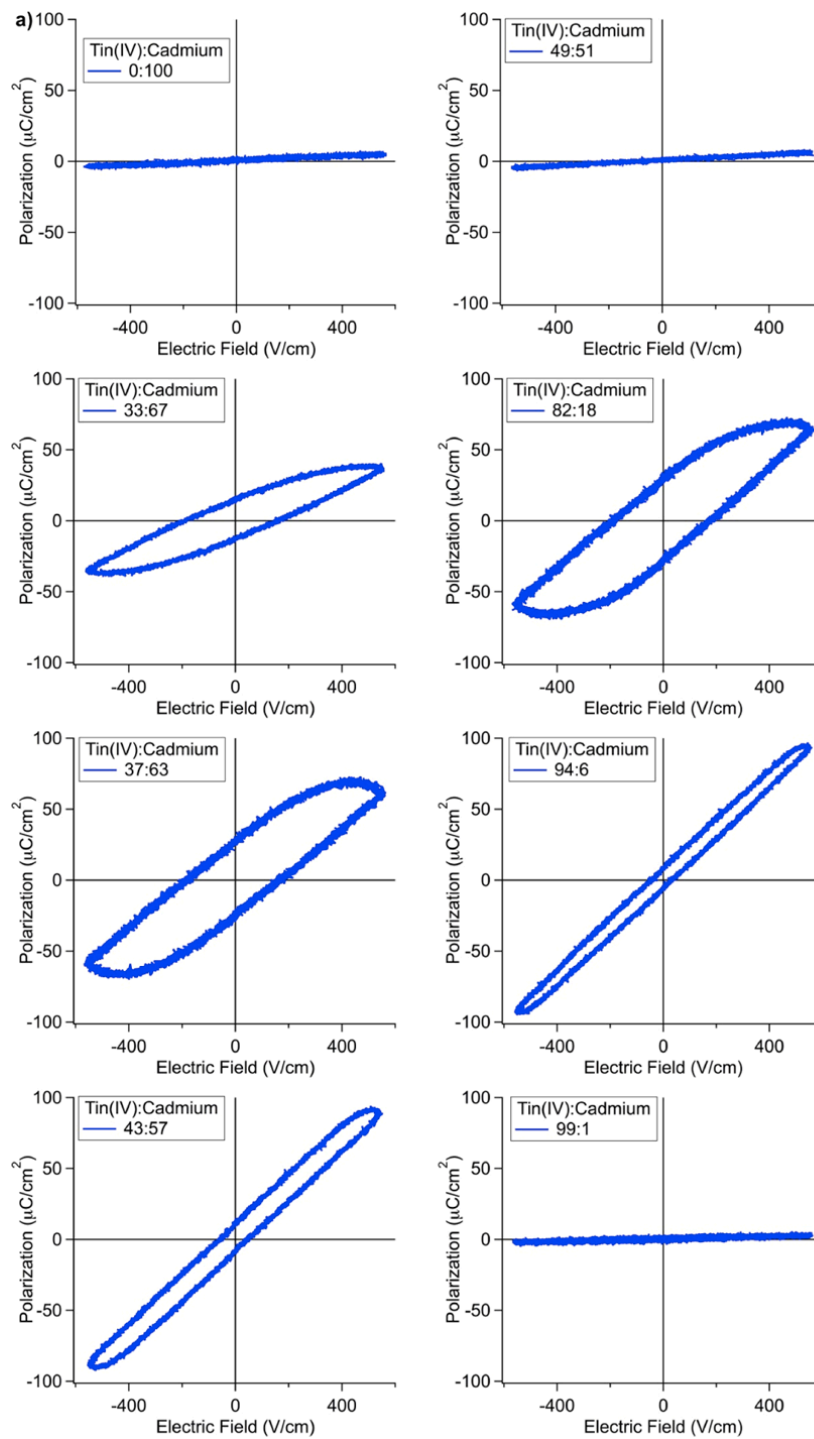
Figure 3.5 Polarization response within an applied electric field for CdSSe QDs treated with solutions of an increasing concentration of SnCl$_4$. A change in tin(IV) concentrations causes a change in the polarization values in the ferroelectric hysteresis, showing that saturation polarization and remnant polarization can be controlled through simple changes in tin(IV) to cadmium ratios.
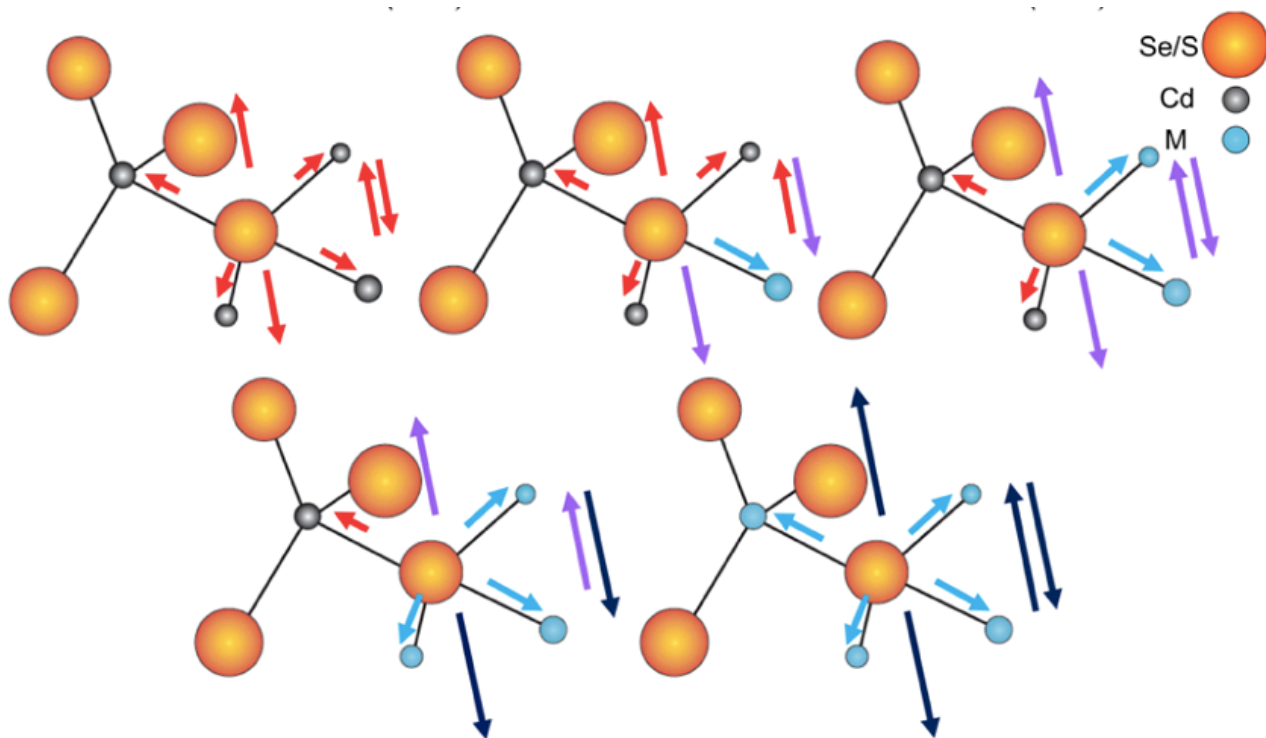
Figure 3.6 Graphic showing dipole moments affected by cation exchange based on polarization response related to atomic percent ratio of tin and cadmium. At lower concentrations, a dipole moment forms and once the ratio of cations exchanged with cadmium reaches about 50:50, the dipoles cancel. With continued increase in the cations exchanged, a dipole moment forms again and once the ratio of cations exchanged with cadmium reaches nearly 100:0, the dipoles cancel again.

The greater charge and electronegativity of tin (IV) as compared to the native cadmium would cause the anions making up the backbone of the zinc blende crystal structure to move closer to the exchanged tin (IV) cations within the tetrahedral holes. This contraction of the anions around the tin (IV) causes an overal shortening of bonds within the crystal, which can be observed by x-ray diffraction. The XRD reflections of a series of CdSSe nanoparticles with an increased ratio of tin (IV) to cadmium (II) exchanged show the reflections shift to higher angles, which is associated with an decrease in *d*-spacing and bond length within the crystal structure. Specifically, the (111) reflection increased by a 2θ of 0.3, the (220) refection increased by a 2θ of 0.2, and the (311) increased by a 2θ of 0.4, shown in Figure 3.7.

Crystal structure disorder due to anion movement toward the exchanged tin (IV) cations is responsible for the peak broadening and decrease in peak intensity observed in the XRD. There is a larger decrease in relative intensity of the (220) peak with increasing exchange with respect to the other reflections. Because the (110) plane has a greater number of cations within the plane, there is a greater relative increase in exchange-induced disorder. This presence of disorder is further shown as the percentage of tin (IV) reaches near 100% and the nanoparticle reaches an amorphous glass phase, which could further explain the measured dielectric response. Another source of this disorder could be the loss of selenium as a result of the heat applied for the exchange to reach near completion. These byproducts were removed using a syringe filter. Overall, it was observed that the saturation polarization increased with a higher tin concentration. However, at lower concentrations of tin (IV), the remnant polarization is greater and the particles better retain crystallinity.
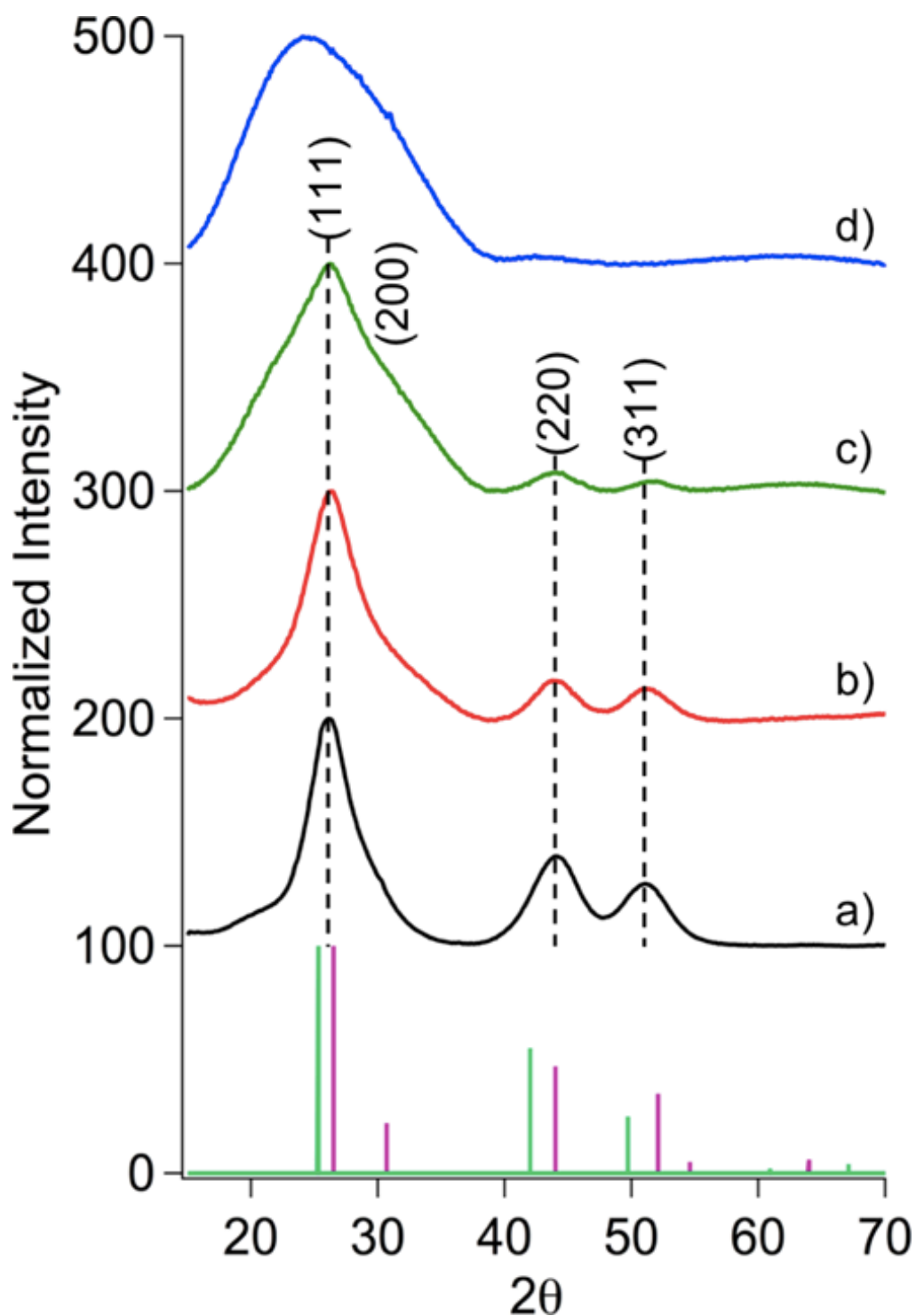
Figure 3.7 XRD pattern showing an increase in crystal structure disorder with the addition of exchange cations. As the tin(IV) to cadmium(II) ratios increased, the disorder within the crystal structure also increased, as shown by peak broadening and a decrease in relative peak intensities and a shift to the right as the amount of tin(IV) to cadmium ratios increase (a) 0:100 (b) 33:67 (c) 49:51 (d) 99:1. The vertical bars are corresponding to JCPDS files for zinc blende CdSe no. 19-0191 and CdS no. 42-1411.

3.4 Conclusions

Formation of ferroelectric nanoparticles through cation exchange gives access to control over shape and size as well as ferroelectric properties of ferroelectric nanomaterials. Through variation of charge and electronegativity as well as concentration, we've gained a greater understanding of the emergence of ferroelectric properties through cation exchange. Cation exchange with different metal chloride salts shows an increase in saturation polarization with an increase in difference in electronegativity between the exchange cation and the native cadmium. Greater charge as well as electronegativity causes a larger change in the dipole. Increasing the concentration of tin (IV) chloride also allowed for modulation of saturation and remnant polarization because of an increase in the number of localized dipoles. Through small changes in the concentration of tin (IV) chloride solutions, we can control ferroelectric properties, broadening the degrees of freedom afforded by nanoparticle-based ferroelectrics. Further, we demonstrated that the lower concentrations of exchanged tin (IV) cations allowed for better crystal structure retention and most likely, greater stability.

CHAPTER IV

OPTIMIZATION OF FERROELECTRIC CATION EXCHANGE SYNTHESIS

4.1 Introduction

The original cation exchange synthesis discovered by Dr. Toshia Wrenn resulted in various byproducts as well as loss of colloidal stability. A large portion of my research focused on optimization of the ferroelectric cation exchange synthesis through various synthetic techniques. Byproducts were first removed through an extra washing step with ethanol, then the formation of byproducts was prevented by performing the cation exchange synthesis in ethanol rather than the original toluene solution in which the QDs were suspended. Aggregation was initially reversed by ligand exchange after the cation exchange synthesis and was then prevented by performing ligand exchange before the washing step in the QD synthesis as well as before the cation exchange synthesis.

4.2 Preventing Byproducts of Cation Exchange Reaction

In our original synthesis based upon the previous Wrenn *et al*. synthesis, the cation exchange was performed with 3 nm +/- 0.16 QDs and antimony (III) chloride both dissolved in toluene. The QDs almost immediately crashed out of solution due to ligand displacement by the chlorine anions while partial cation exchange occurred between antimony and cadmium. The displaced cadmium reacted with the remaining chlorine anions in solution to form $CdCl_2 \cdot H_2O$, a known ferroelectric. $CdCl_2 \cdot H_2O$ is highly soluble in polar solvents, so in order to remove the byproducts and get a more reliable polarization response, we performed the cation exchange in ethanol rather than toluene to

disallow $CdCl_2 \cdot H_2O$ formation completely. TEM and STEM-EDS show large $CdCl_2 \cdot H_2O$ sheets

in Figures 4.1 and 4.2 as well as the presence of chlorine on the surface of the QDs due to ligand

displacement in the original synthesis in toluene and, while the chlorine is still localized on the

QDs, the $CdCl_2 \cdot H_2O$ sheets disappear in the new ethanol synthesis shown in Figure 4.3. This is

confirmed through XRD of the original QDs, the synthesis in toluene showing presence of

$CdCl_2 \cdot H_2O$, and the synthesis in ethanol in which the peaks corresponding to $CdCl_2 \cdot H_2O$
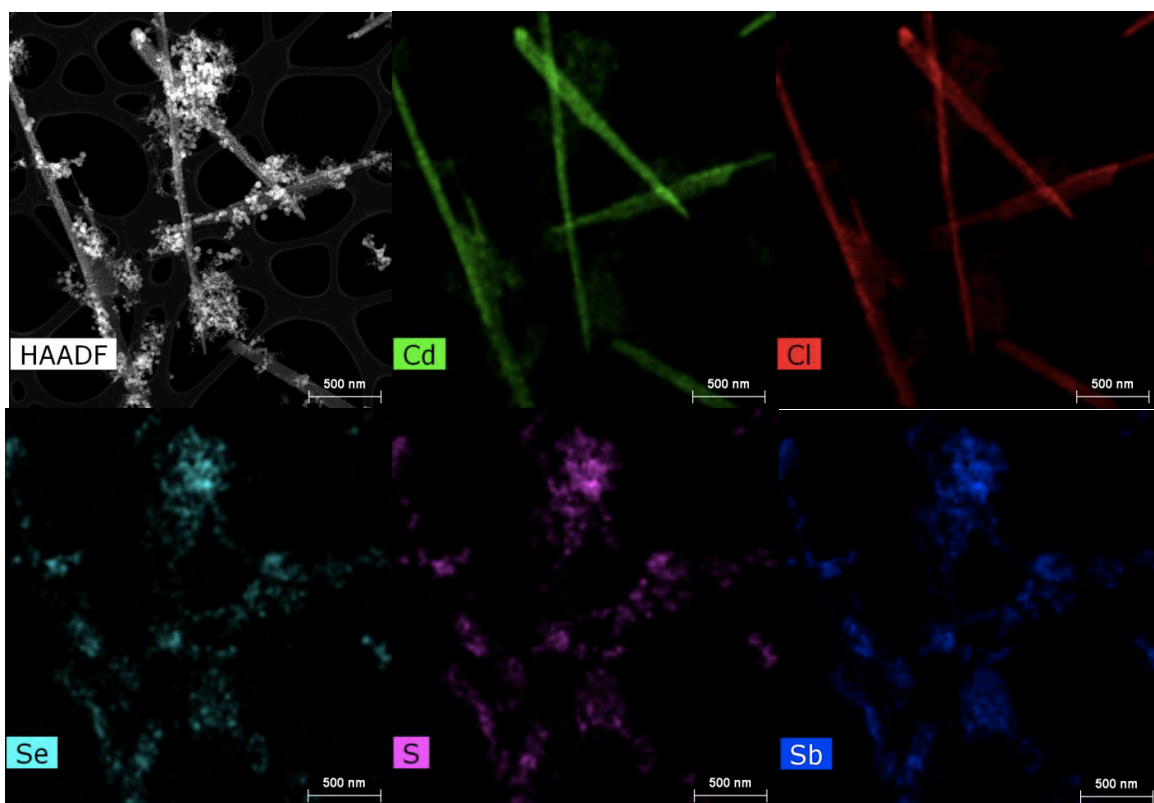
disappear, shown in Figure 4.4.

Figure 4.1 STEM-EDS mapping showing $CdCl_2 \cdot H_2O$ sheets surrounded by $CdSSe/SbCl_3$
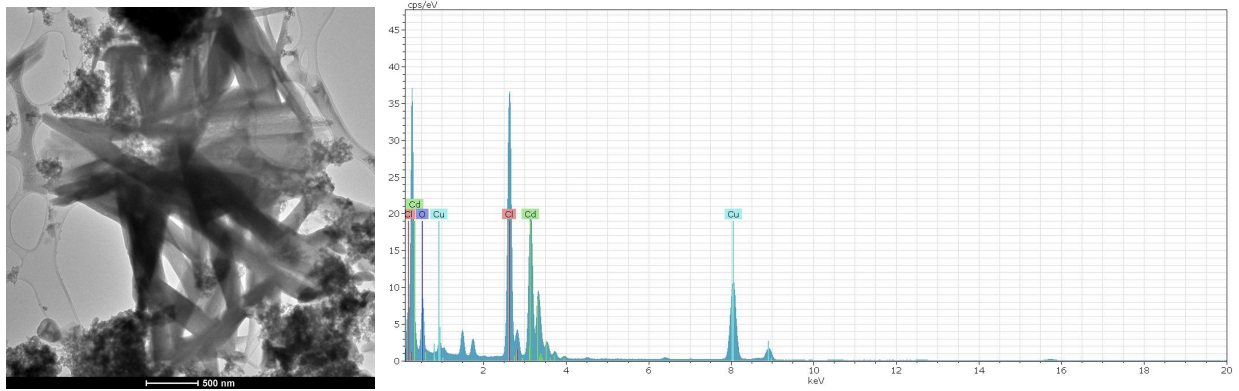aggregates. $CdCl_2 \cdot H_2O$ forms only in cation synthesis in toluene.

Figure 4.2 TEM and EDS spectrum of magnified $CdCl_2 \cdot H_2O$ sheets.

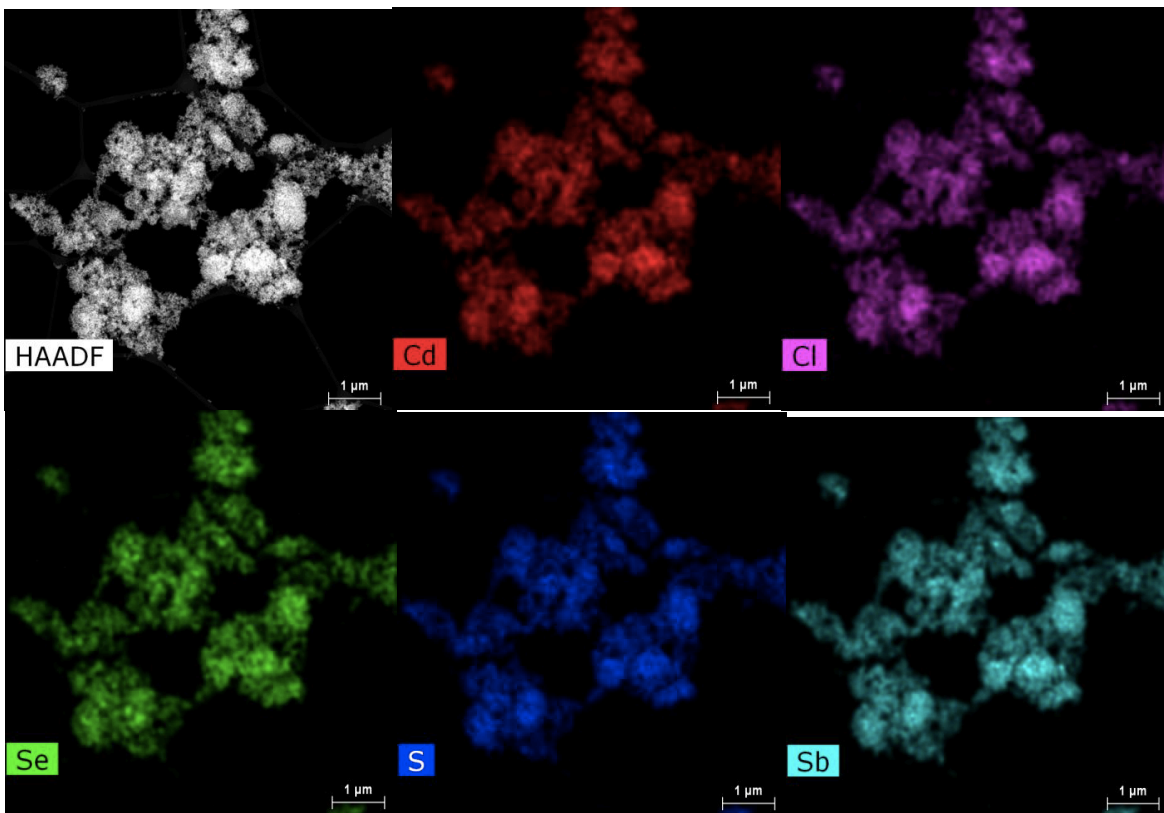
Figure 4.3 TEM and STEM-EDS of $CdSSe/SbCl_3$ sans $CdCl_2 \cdot H_2O$. Cation exchange synthesis in ethanol disallows for formation of $CdCl_2 \cdot H_2O$.
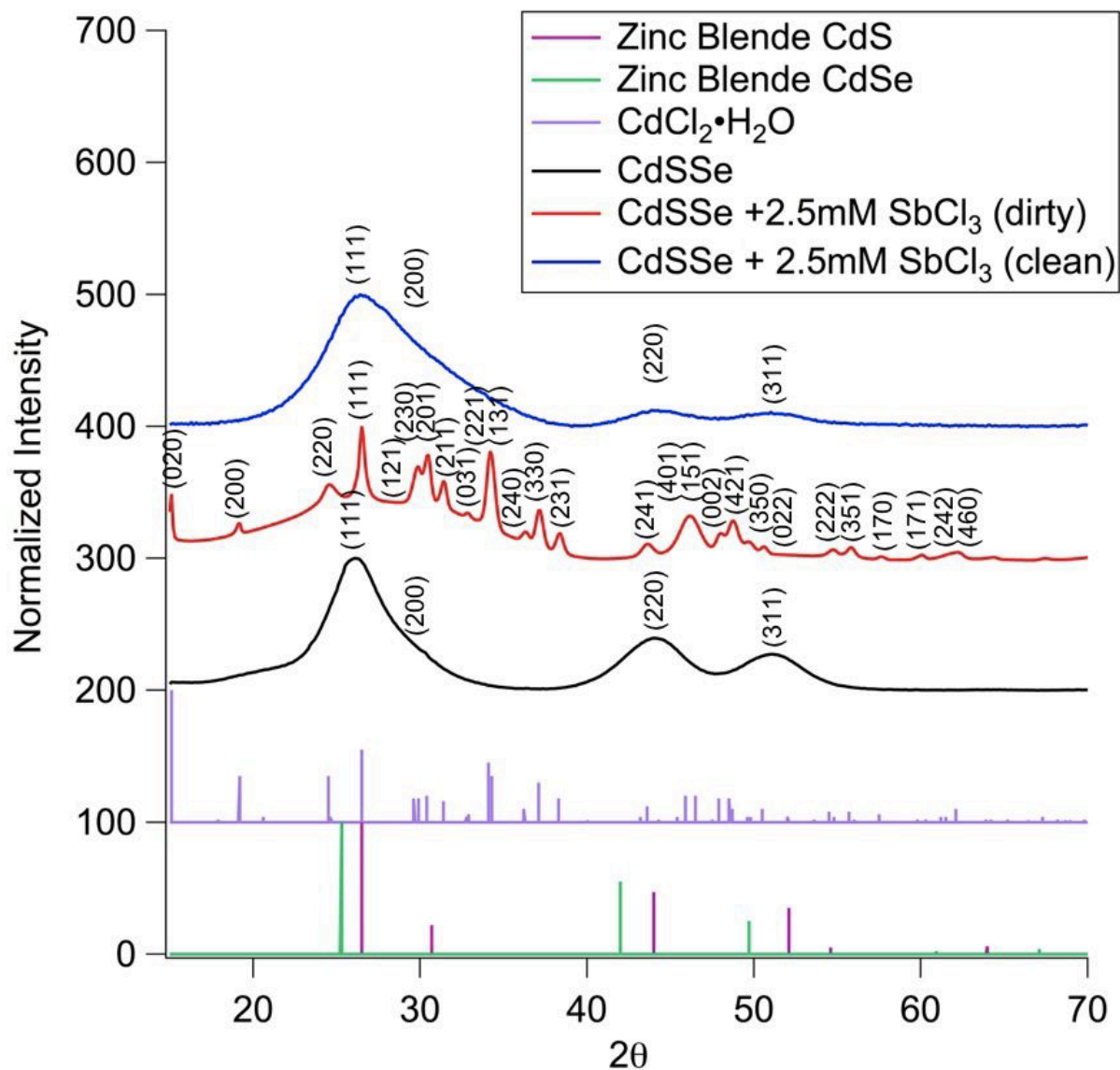
Figure 4.4 XRD of original CdSSe quantum dots and CdSSe SbCl₃ cation exchange syntheses in toluene and ethanol to show presence of CdCl$_2$•H$_2$O formation in toluene and that CdCl$_2$•H$_2$O is unable to form in ethanol synthesis.

4.3 High Concentration Byproducts

As tin (IV) chloride concentrations reached higher concentrations and as heat was applied, large selenium elemental particles began to form, which was apparent in STEM-EDS and XRD analysis (Figures 4.5 and 4.6). The relatively high concentrations of tin (IV) and increase in temperatures may have caused a REDOX reaction to occur, reducing some tin (IV) to tin (II) and partially

oxidizing negatively charged selenium within the nanoparticles to selenium metal. These were removed using a syringe filter and remaining particles were analyzed using XRD shown in Figure 4.6. Se(0) has not been found to have ferroelectric properties at room temperature. Because ferroelectric properties and crystal structure retention were optimized at lower concentrations, the formation of selenium byproducts is avoided.
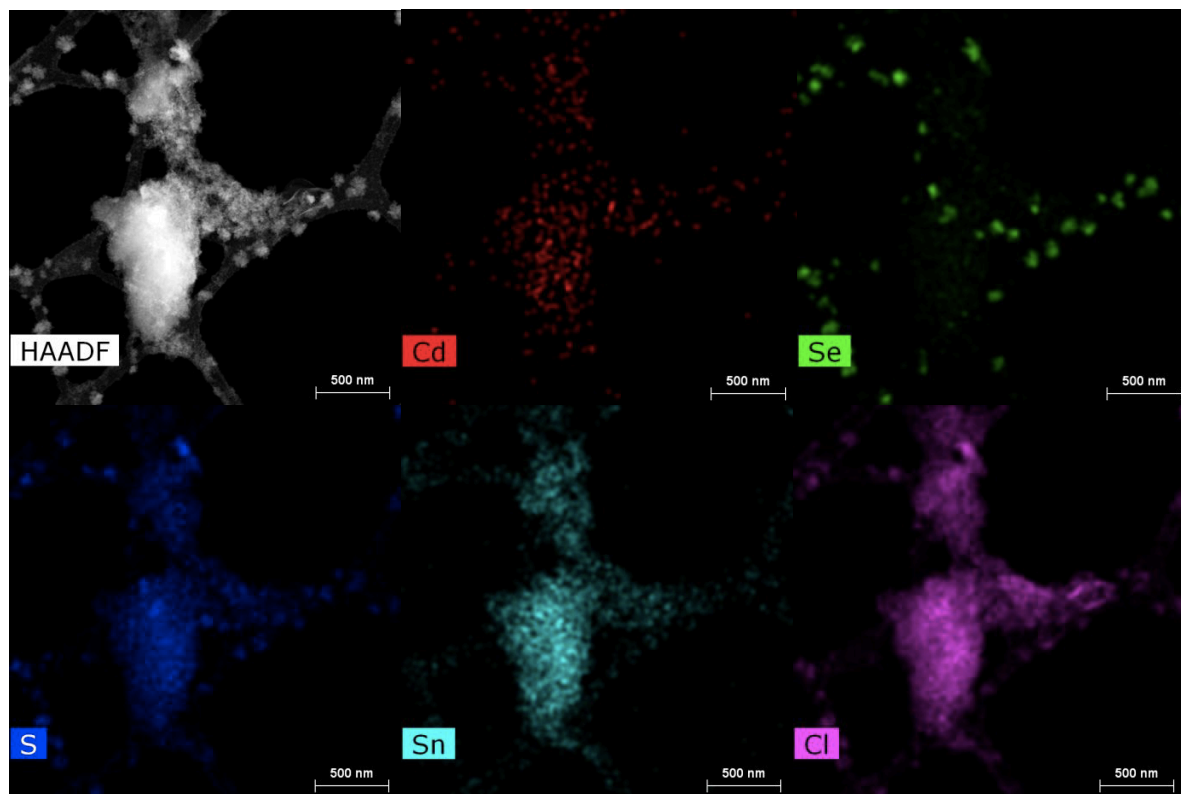

Figure 4.5 STEM-EDS of high concentration, heated $SnCl_4$ cation exchange reaction, showing the formation of nanoparticle aggregates with high Sn^{4+} dopant concentrations as well as elemental selenium formation due to possible REDOX reactions due to higher concentrations and increase in temperature.
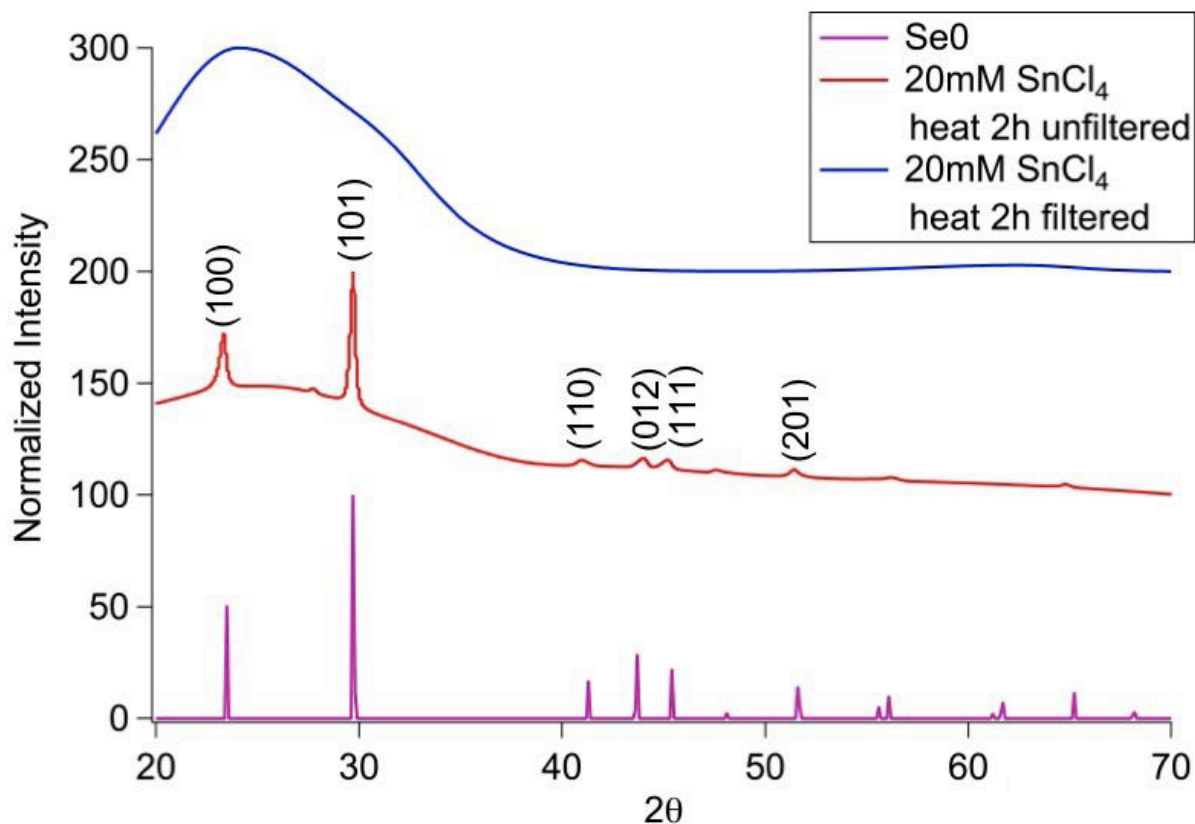
Figure 4.6 XRD of filtered and unfiltered high concentration, increased temperature CdSSe SnCl$_4$ reaction, showing formation of elemental selenium as well as disordered crystal structure of resulting CdSSe with high Sn^{4+} dopant concentrations once elemental selenium is removed.

4.4 Aggregation Prevention

Cation exchange synthesis performed on QDs resulted in aggregation due to the displacement of oleic acid ligands by chlorine anions on the QD surface. This is shown by the presence of chlorine on aggregated nanoparticles in STEM-EDS maps. According to hard-soft acid-base theory, cadmium is a soft acid, while carboxylate ligands, such as oleate, are hard bases. This makes it easy for a borderline base, such as chloride ions, to displace these ligands, causing the loss of colloidal stability and aggregation. This aggregation is reversed with the presence of an excess of soft base, such as an organic phosphine ligand in the form of trioctylphosphine (TOP).[81-83] TOP was shown to displace the chloride ions through redispersion of the nanoparticles in solution and

by visual analysis and the analysis of TEM images (Figure 4.8). While oleic acid and chlorine are known to be X-type ligands, which can easily displace each other, trioctylphosphine is an L-type ligand.[101] Owen *et al.* has demonstrated L-to X-type ligand exchange is possible in CdSe nanocrystals while Buhro *et al.* has shown that this ligand exchange reaction between L- and X-type ligands is fully reversible using CdSe quantum belts.[102, 103] The difference in charge of the ligands exchanged may result in a positively charged surface due to the displacement of anionic ligands by neutral-donor ligands. By performing a ligand exchange before cation exchange, aggregation is prevented by disallowing ligand displacement by chlorine anions, shown by the disappearance of chlorine in STEM-EDS maps as well as the chlorine peak in the EDS spectrum of the chlorine anions on the QD surface (Figures 4.9 and 4.10).
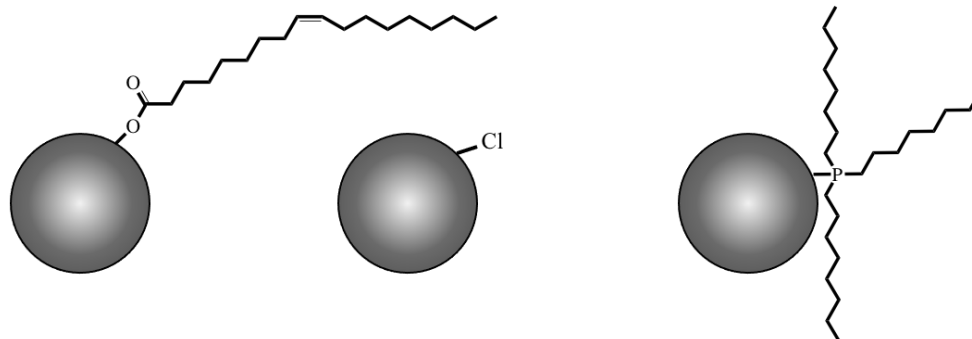
Figure 4.7 Hard-soft acid-base theory implies that oleate, a hard base, is easily displaced by chlorine, a borderline base on soft-acid cadmium nanoparticles. A soft base, such as trioctylphosphine then easily displaces chlorine.
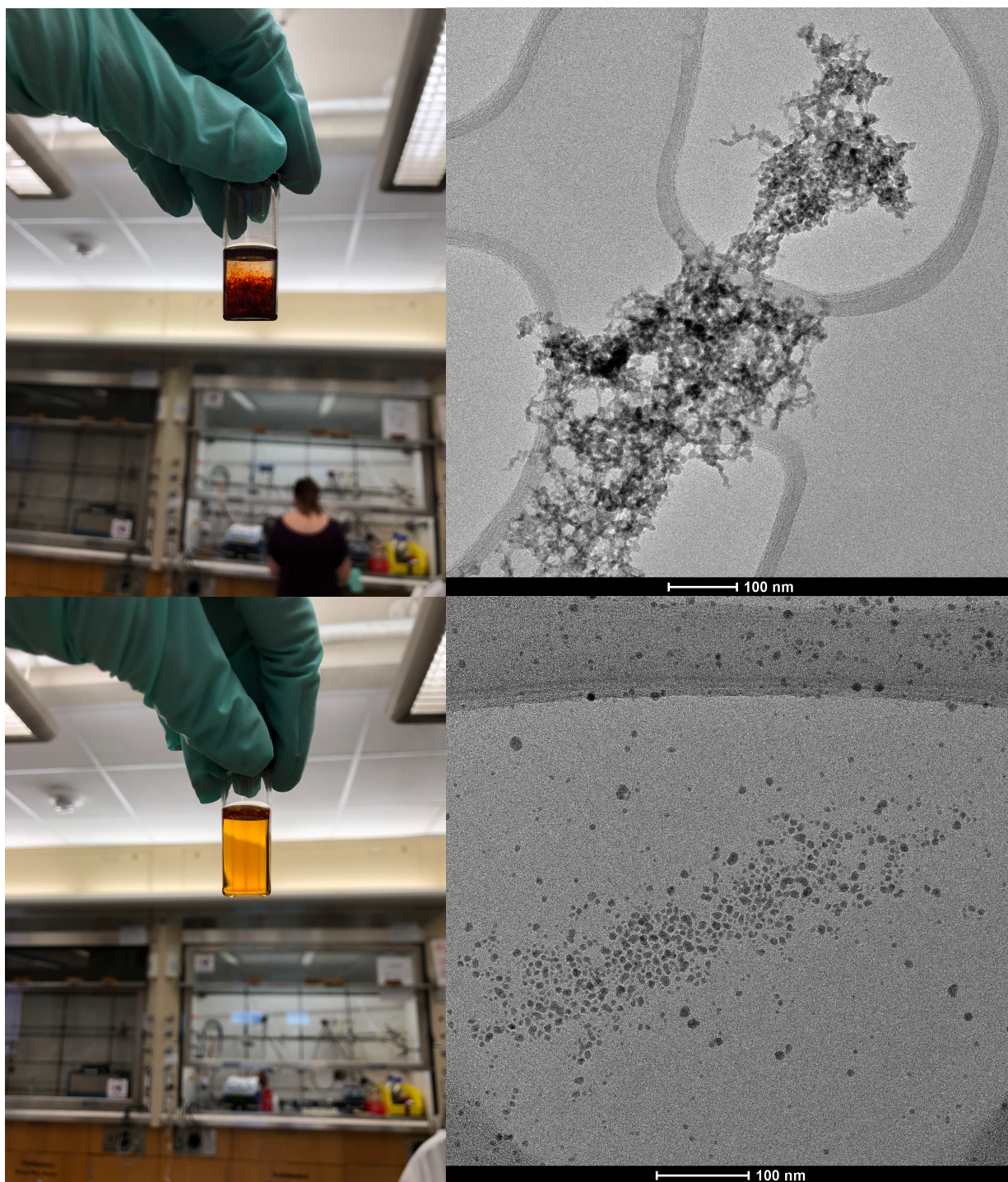
Figure 4.8 Aggregation almost instantly occurs due to oleate ligand displacement by chlorine anions but is reversed with an excess of trioctylphosphine.

Figure 4.9 STEM-EDS maps and EDS spectrum of aggregated nanoparticles after tin(IV) cation exchange showing the presence of cadmium, selenium, sulfur, tin, and chlorine.

Figure 4.10 STEM-EDS maps and EDS spectrum of nanoparticles after tin(IV) cation exchange showing the presence of cadmium, selenium, sulfur, and tin. Chlorine is no longer present on the surface and nanoparticles are no longer aggregated.

4.5 Conclusions

The original synthesis by Dr. Toshia Wrenn in which CdSe nanoparticles were treated with antimony (III) chloride resulted in the discovery of ferroelectric QDs. Howe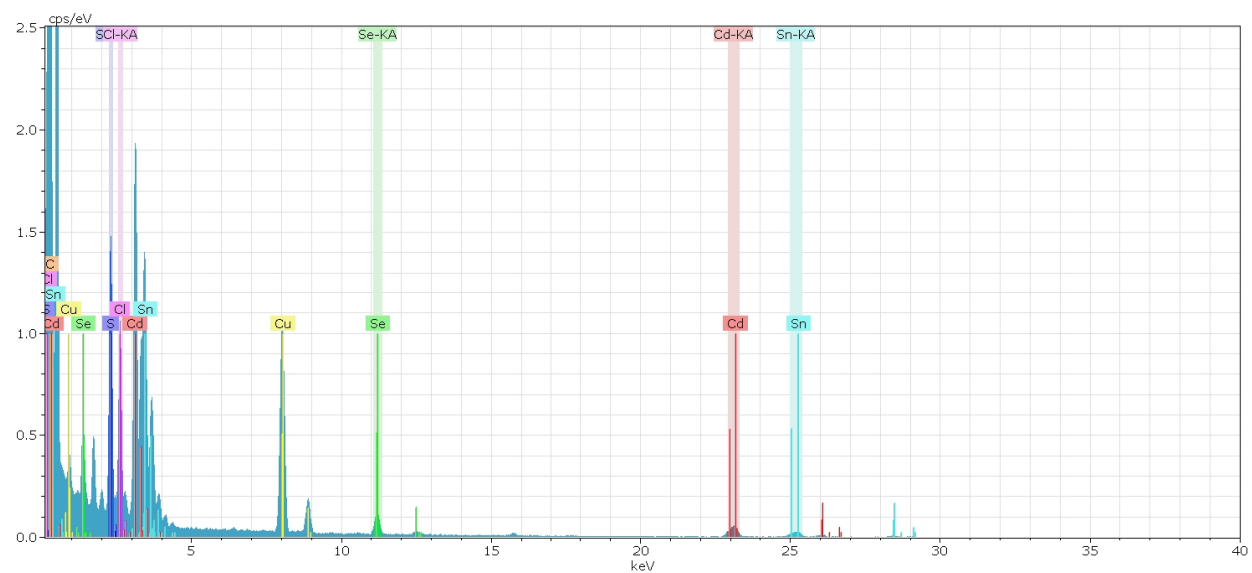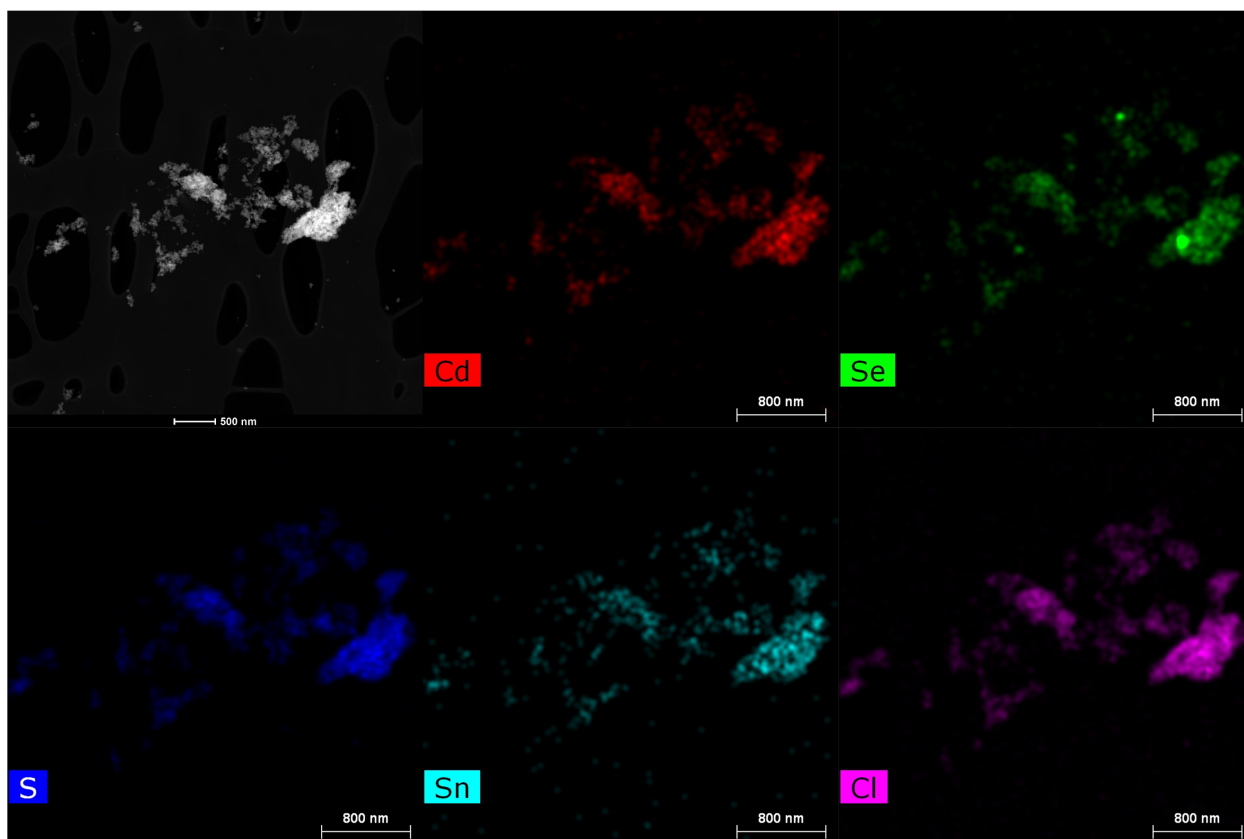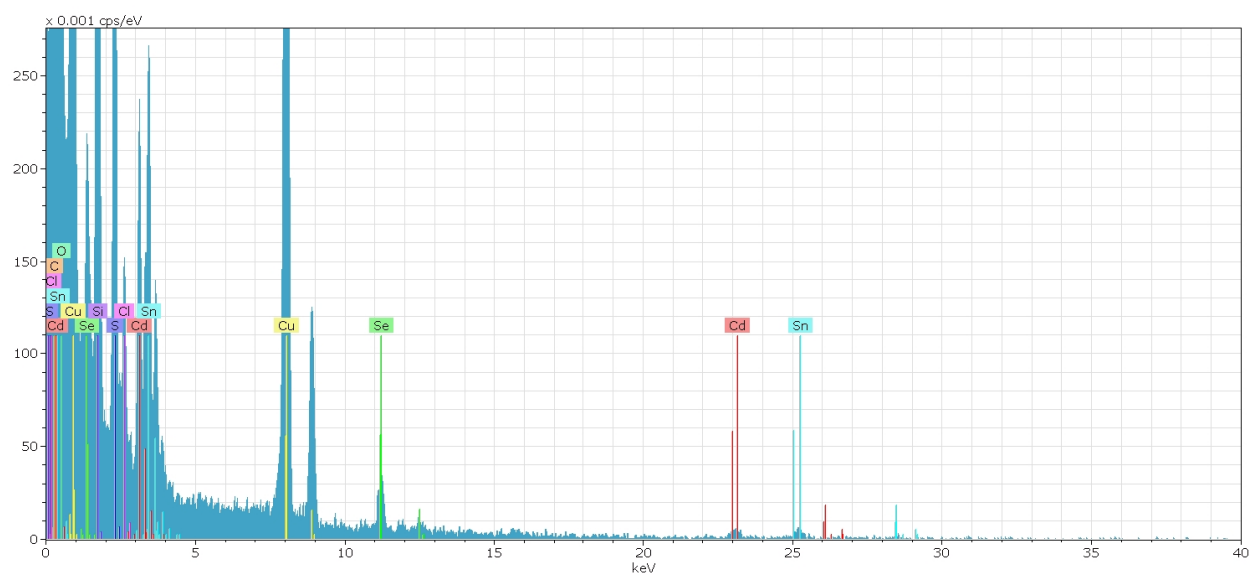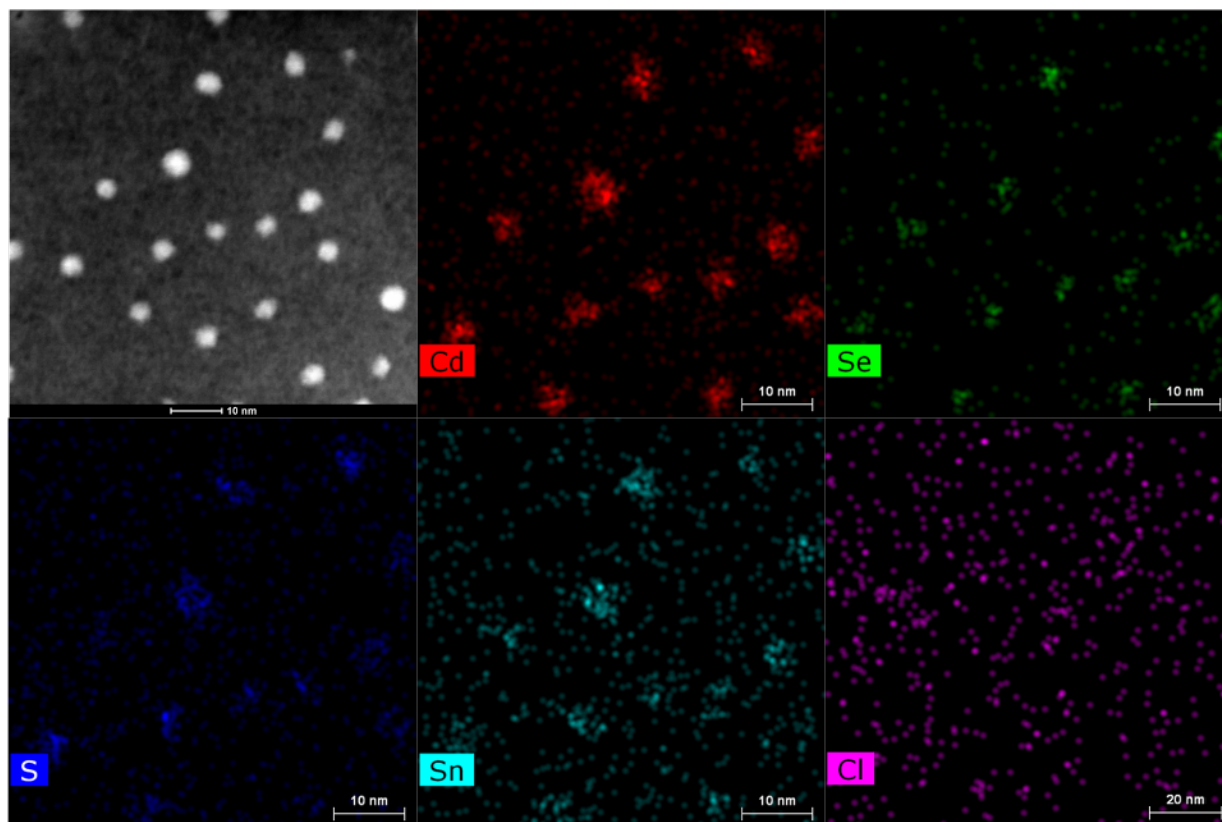ver, the cation exchange synthesis resulted in aggregation as well as the formation of byproducts that effect quantitative ferroelectrics analysis and EDS quantification. Byproducts that formed due to a reaction between chloride anions in solution and the ejected cadmium were removed by performing the cation exchange synthesis in a polar solvent, which resulted in the lack of formation of $CdCl_2 \cdot H_2O$. High concentration byproducts found during ferroelectric optimization studies were removed via syringe filter. These products only formed when using the highest concentration tin (IV) chloride solution and applying heat due to a redox reaction and it was found that ferroelectric properties and crystal structure retention were optimized at lower concentrations. Aggregation occurred due to the displacement of oleate ligands by chlorine anions. Colloidal stability was first recovered through ligand exchange with trioctylphosphine to displace the chlorine on the nanoparticle surface then retained through ligand exchange before cation exchange to prevent ligand displacement.

CHAPTER V

FLUORESCENCE RETENTION

5.1 Introduction

Once ferroelectric properties were optimized, byproducts were removed, and loss of colloidal stability was reversed, complications with fluorescence retention still remained. This is likely due to the presence of defects as a result of cation exchange, which leads to charge carrier trapping. Here we report a method of introducing ferroelectricity while maintaining fluorescence by adding a protective shell to the core. The shell provides a sacrificial material where cation exchange can occur without introducing fluorescence quenching defects in or near the surface of the core (Figure 5.1). This final optimization step yields colloidally stable and fluorescent ferroelectric quantum dots.
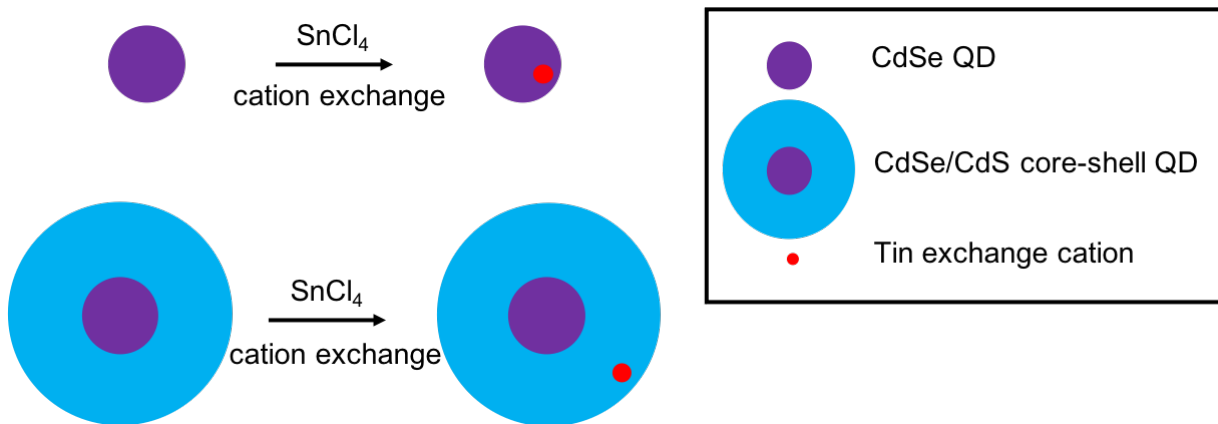

Figure 5.1 Schematic of the introduction of defects into QDs due to tin cation exchange. Cation exchange occurring within the fluorescent CdSe QD (purple) results in near 100% fluorescence quenching while cation exchange within a protective CdS shell (blue) allows for fluorescence retention while still introducing ferroelectric properties.

5.2 Fluorescence Retention Through Protective Shelling

Cation exchange synthesis performed on CdSe nanoparticles resulted in near total quenching of fluorescence. In order to prevent fluorescence quenching, we shelled the fluorescent CdSe core in CdS. This allows for the protection of the core from defects produced from cation exchange and therefore allows for quantum yield retention. Partial displacement of cadmium by tin cations within the QDs is confirmed by STEM-EDS in Figure 5.2. To avoid overlap between cadmium and tin during EDS quantification, the tin Kα peak at 25.2 keV was used.
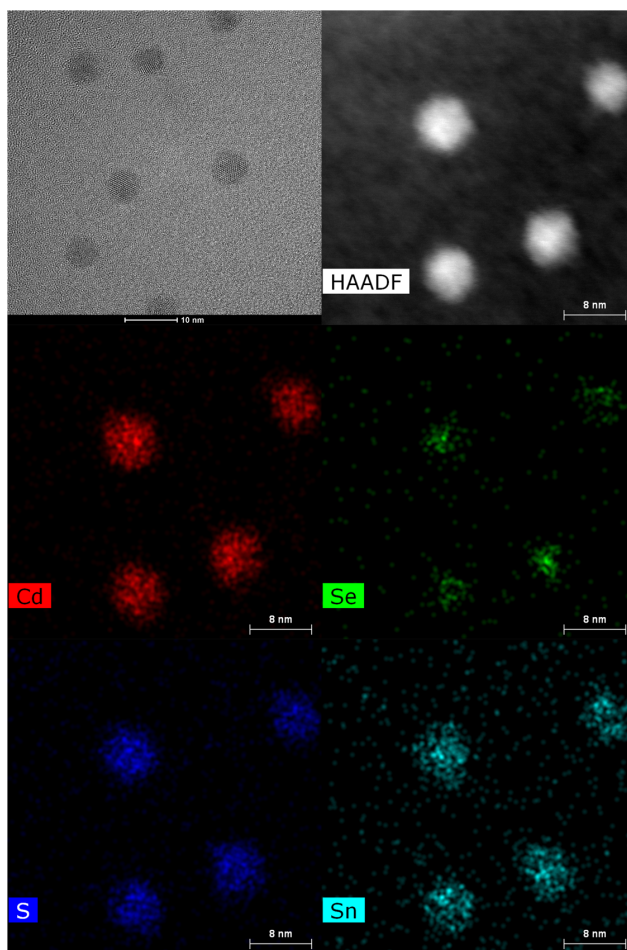

Figure 5.2 STEM-EDS maps of 8 monolayer core-shell CdSe/CdS nanocrystals after undergoing partial cation exchange with tin(IV).

The CdSe/CdS core-shell synthesis varied from 0-8 monolayers, increasing fluorescence retention from total quenching at 0 CdS shells to near 99% fluorescence retention at 8 monolayers. However, the fluorescence blue-shifted in each cation exchange reaction. The initial red-shift that occurs during CdSe/CdS shelling occurs due to the leaking of confinement of the hole from the core into the shell. Cation exchange disrupts the band structure of the shell which results in better confinement to the CdSe core and therefore a blue-shift in the final fluorescence spectra. Ferroelectric properties of CdSe, CdSe/2CdS, CdSe/4CdS, CdSe/6CdS, and CdSe/8CdS have similar saturation polarization and remnant polarization values which is confirmed in Figure 5.3. Analysis of EDS quantification shows decrease in Sn/Cd ratio, meaning similar amounts of tin were exchanged and ferroelectric properties remained the same. This can be attributed to the idea that a similar amount of dipoles form with similar amounts of tin exchange. With thick CdS shells, enough cation exchange can occur to induce a ferroelectric response while minimizing charge carrier overlap with the exchange created defects, which could be in the form of vacancies or interstitial defects.
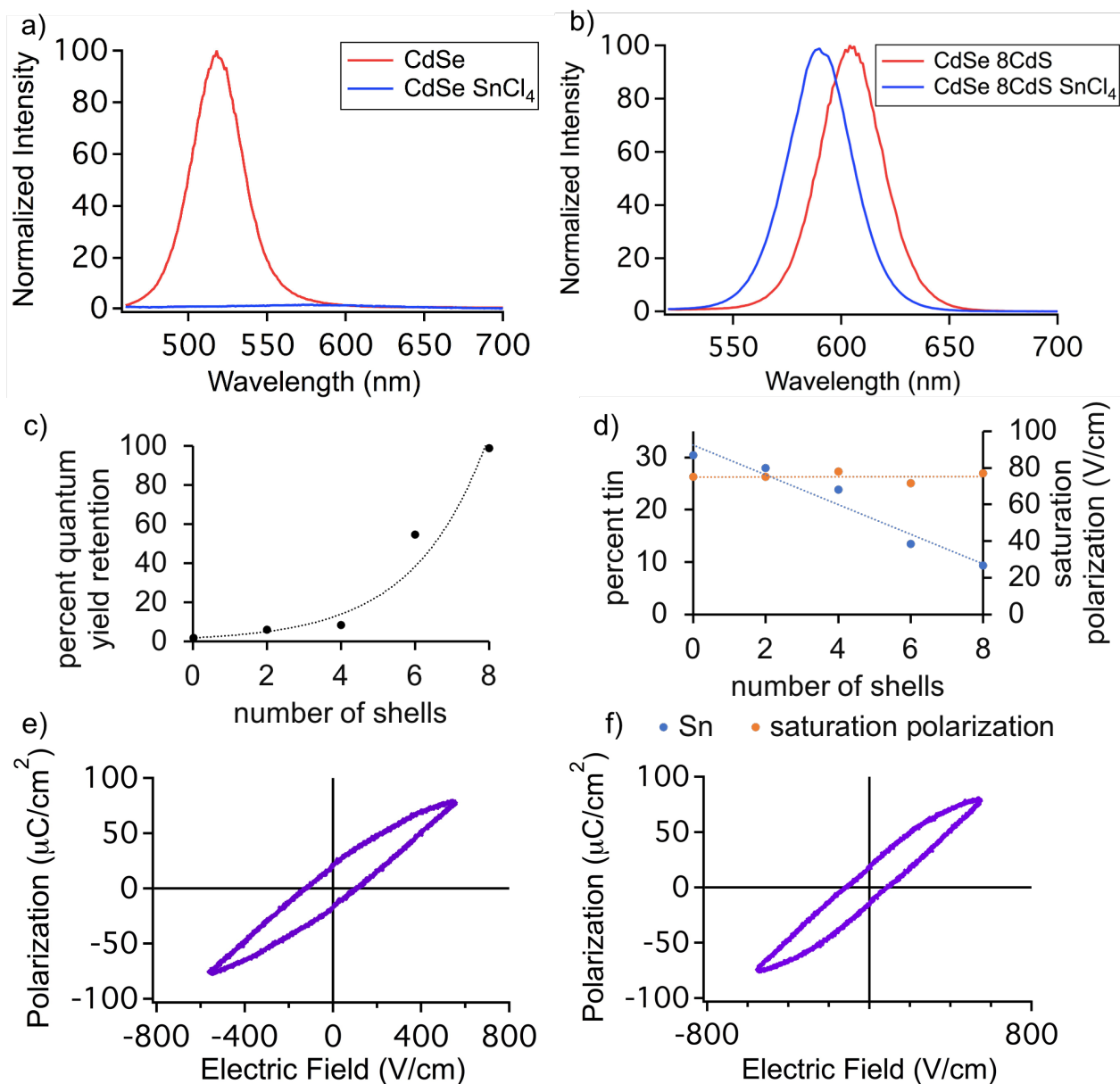
Figure 5.3 Fluorescence spectra of a) CdSe QDs before and after tin(IV) cation exchange and b) CdSe/8CdS core-shell QDs before and after tin(IV) cation exchange. c) Dependence of fluorescence quantum yield retention on number of CdS monolayer shells. d) Dependence of relative percent tin exchanged on number of CdS monolayer shells (blue) and the retention of ferroelectric saturation polarization (orange). e,f) Polarization response within an applied electric field for e) CdSe and f) CdSe/8CdS QDs after tin(IV) cation exchange. A Sawyer-Tower circuit was used to quantitatively measure polarization from ferroelectric nanoparticles.

5.3 Conclusions

Inducing ferroelectricity through cation exchange greatly increases the already broad spectrum of QD applications. With the introduction of defects within the crystal structure that occurs due to cation exchange in the fluorescent CdSe core, fluorescence was fully quenched with the introduction of ferroelectric properties. In order to retain fluorescence, a protective CdS shell was grown around the core before cation exchange, resulting in the introduction of defects, and therefore ferroelectricity, in the protective shell instead of the core. While fluorescence was nearly totally quenched in pure CdSe QDs, with 8 CdS shells, fluorescence quantum yield was retained 98.8%. After the cation exchange, colloidally stable fluorescent, ferroelectric QDs are realized.

CHAPTER VI

NON-TOXIC, FERROELECTRIC QUANTUM DOTS

6.1 Introduction

While cadmium-based nanoparticles have been primarily used for these studies, non-toxic QDs are more functional for industrial applications. Indium phosphide/zinc selenide core-shell nanocrystals have been considered as a possible non-toxic substitute for CdSe/CdS QDs. ZnSe has a similar zinc blende crystal structure to CdSe and CdS QDs, which were used in previous studies. Therefore, similar properties should emerge through cation exchange in ZnSe nanocrystals.

6.2 Ferroelectric Zinc Selenide Quantum Dots

Zinc selenide has a similar zinc blende crystal structure to the previously synthesized cadmium selenide, $CdS_{0.7}Se_{0.3}$ graded alloy, and CdSe/CdS core-shell nanoparticles. Because the emergence of ferroelectricity is entirely based on the emergence of dipoles based on the crystal structure, with tin cation exchange within zinc selenide nanoparticles and through EDS quantification, we can determine that a 15.7% cation exchange occurred (Figures 6.1 and 6.2). Our hypothesis of the emergence of ferroelectric properties through cation exchange in zinc blende nanoparticles was confirmed through the emergence of a hysteresis curve with a saturation polarization of 77.5 $\mu C/cm^2$ and a remnant polarization of 11.3 $\mu C/cm^2$ (Figure 6.3).
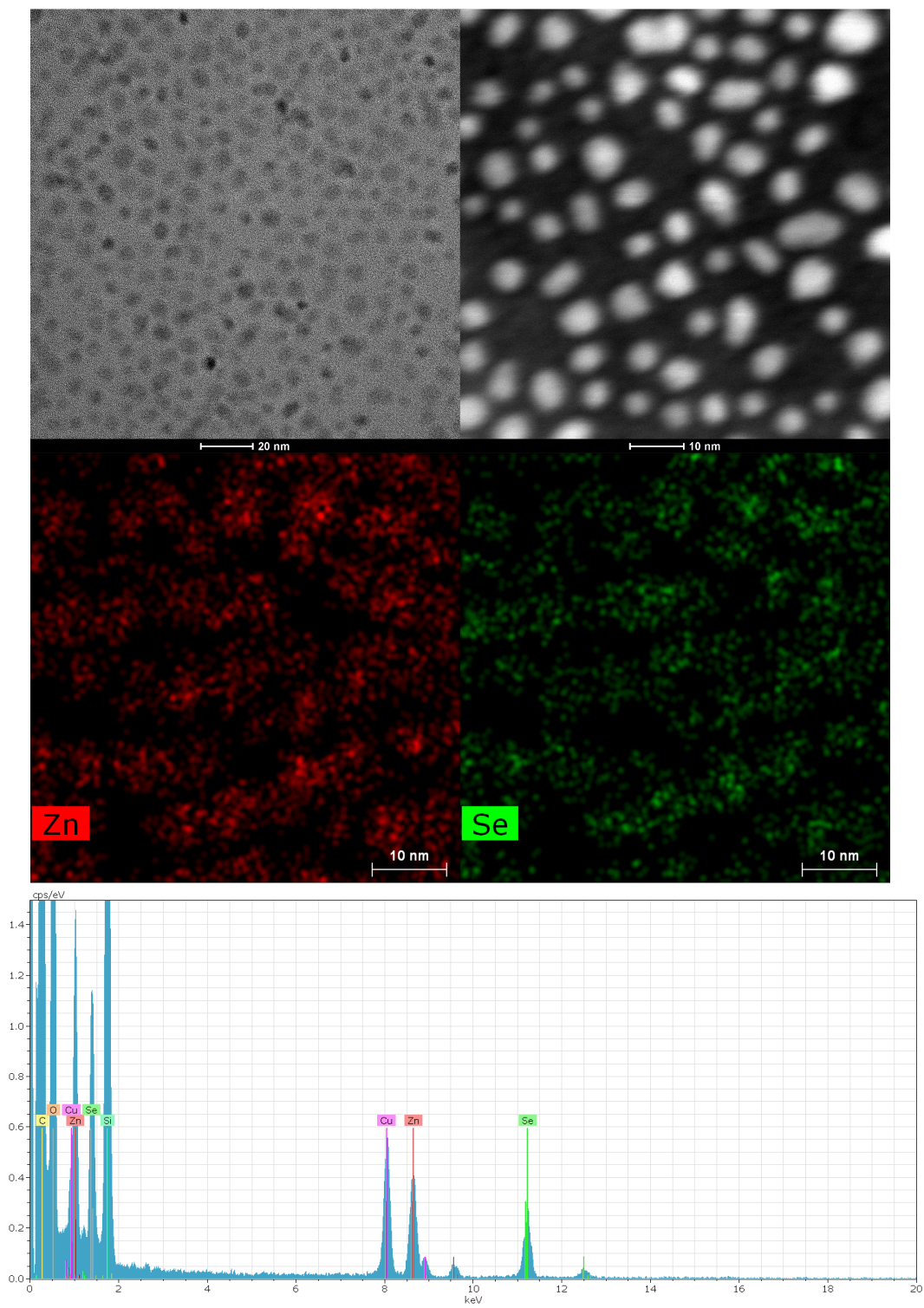
Figure 6.1 STEM-EDS maps and EDS spectrum of ZnSe nanoparticles showing the presence of zinc and selenium.
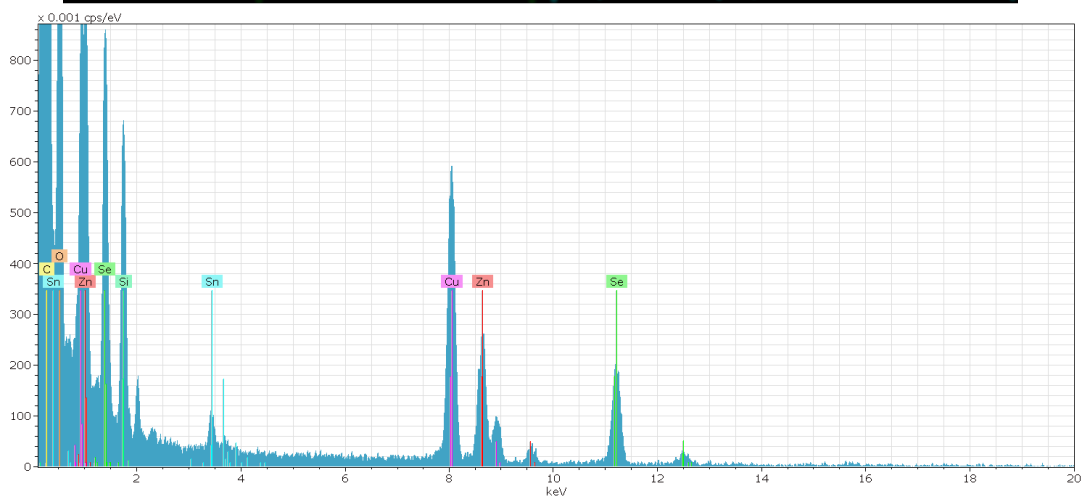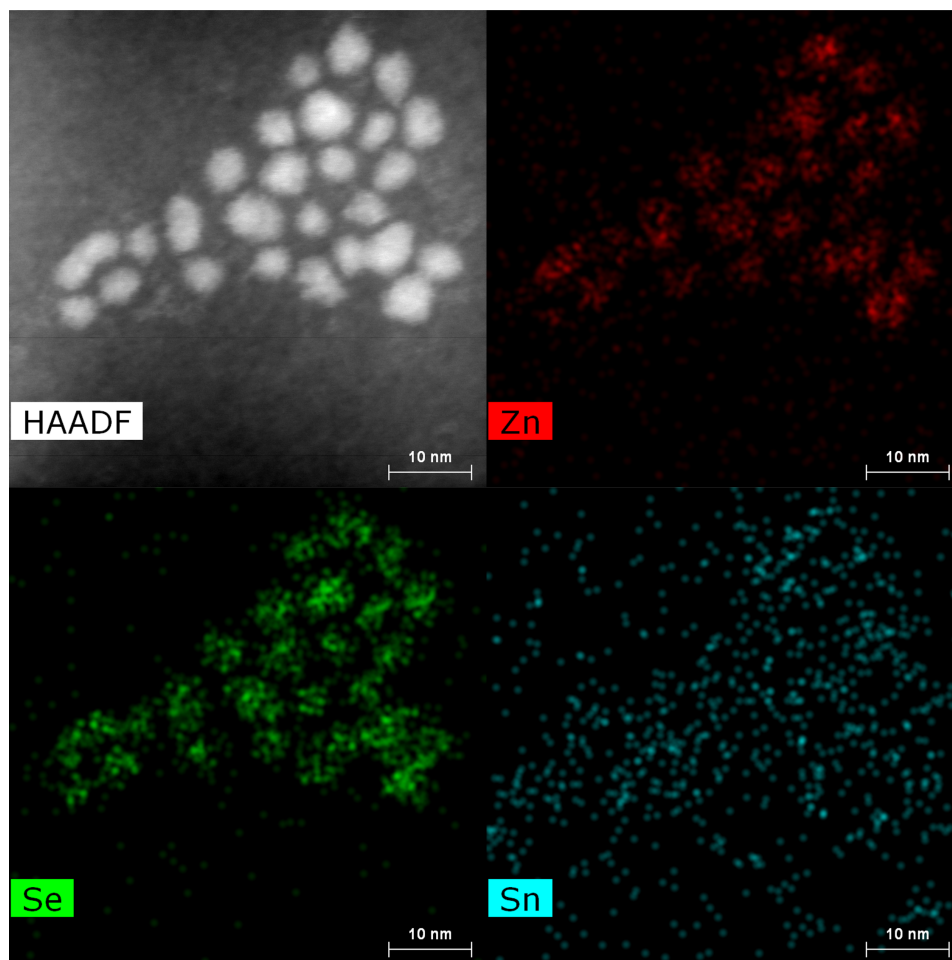
Figure 6.2 STEM-EDS maps and EDS spectrum of ZnSe nanoparticles after tin(IV) cation exchange showing the presence of zinc, selenium, and tin.
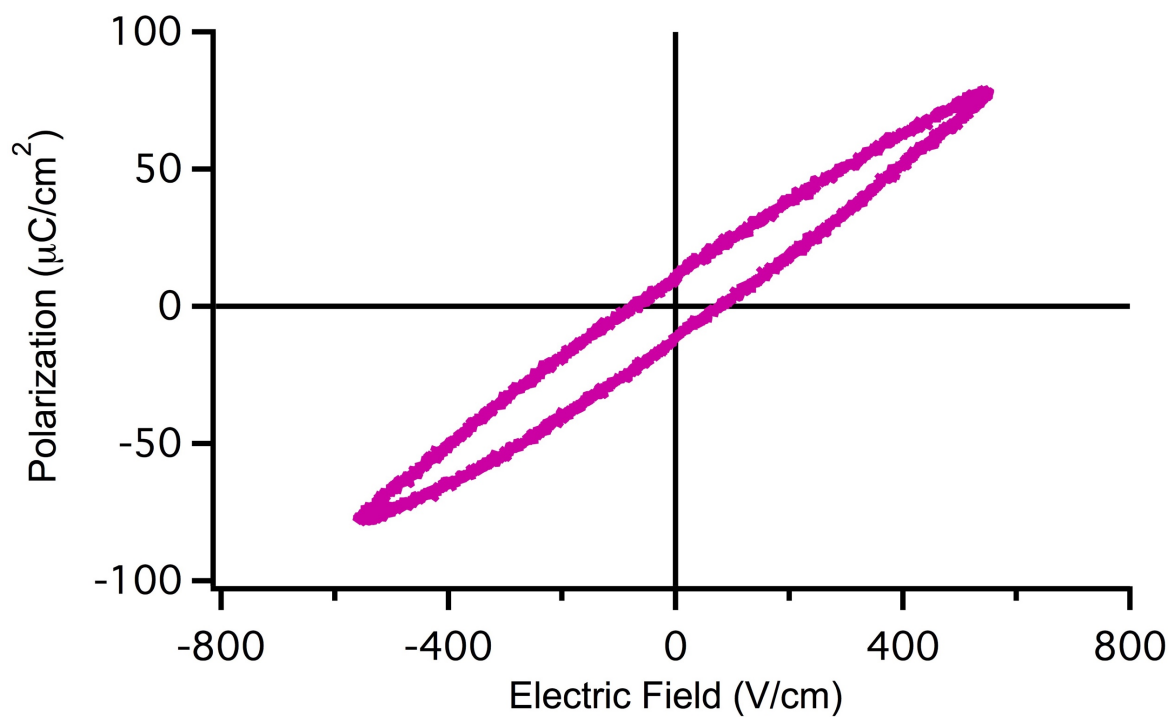
Figure 6.3 Polarization response within an applied electric field for ZnSe QDs after tin(IV) cation exchange.

6.3 Conclusions

Synthesis of ferroelectric QDs by performing cation exchange on non-toxic, zinc blende semiconductor nanocrystals allows for the use of ferroelectric QDs in industrial settings. Zinc selenide is easily synthesized and colloidally stable, allowing for ease of analysis after cation exchange for an introduction to non-toxic, ferroelectric semiconductor nanocrystals by using nanocrystals with a similar crystal structure to previously synthesized cadmium-based ferroelectric QDs. With the introduction of a tin (IV) exchange cation to the ZnSe nanocrystals, ferroelectric properties emerged just as they did in their cadmium-based counterparts. Once colloidal stability has been achieved in zinc blende InP/ZnSe core-shell nanoparticles[100], the synthesis of non-toxic, fluorescent, ferroelectric semiconductor nanocrystals can be achieved. Using the core-shell studies

of the cadmium-based ferroelectric QDs, fluorescence retention will be achieved by inducing ferroelectric properties in a protective ZnSe shell which surrounds a fluorescent InP core.

CHAPTER VII

CONCLUSIONS AND FUTURE WORK

7.1 Overall Conclusions

Ferroelectric semiconductor nanocrystals formed through cation exchange were first discovered in 2015 by Dr. Toshia Wrenn through antimony (III) treatment of CdSe nanoparticles. The realization of these new properties added to the plethora of already ever-growing QD applications. While QDs already have a use in lighting, displays, biological labeling, lasers, and solar cells, the introduction of ferroelectric properties also allows for their use in ferroelectric random access memory, energy harvesters, energy scavengers, actuators, transducers, capacitors, and micro electromechanical devices due to the ability to change the polarization of the materials through electric, thermal, and mechanical energy.

While Dr. Wrenn optimized ferroelectric properties through increased reaction time in the cation exchange synthesis, I was able to further optimize saturation and remnant polarization by varying cation identity and concentration. A correlation between electronegativity determined through the Mulliken equation and saturation polarization was found when analyzing ferroelectric nanoparticles formed through cation exchange with various metal chloride salts including tin (II) chloride, antimony (III) chloride, gold (III) chloride, and tin (IV) chloride. It was found that the exchange synthesis using the highest electronegativity cation, tin (IV), resulted in the highest saturation polarization. Therefore, optimization of percent cation exchange was performed using tin (IV) at varied concentrations of tin (IV) chloride salt solutions. Saturation and remnant polarization were optimized at about 37% and

82%; however, crystal structure was best retained at lower exchange cation to cadmium ratios. Therefore, ferroelectric semiconductor nanocrystals were best optimized through a tin (IV) cation exchange reaction with a 37% cation exchange.

Once ferroelectric properties were optimized, removal of byproducts and aggregation prevention would allow for optimization of the ferroelectric nanoparticles. Through performing the cation exchange synthesis in polar solvents rather than toluene, $CdCl_2 \cdot H_2O$ byproducts formed due to cation exchange were unable to form. Selenium byproducts that formed at high concentrations with the addition of heat were removed with a syringe filter for analysis; however, since ferroelectric properties and crystal structure retention were optimized at lower concentrations, the formation of these byproducts is avoided. Aggregation was prevented through ligand exchange with TOP, a soft base, before cation exchange was performed.

Due to the introduction of defects, fluorescence was quenched after the cation exchange synthesis. Because ferroelectricity emerges due to polarization within the crystal structure, by performing a cation exchange reaction and introducing defects into a protective CdS shell on a fluorescent CdSe core, ferroelectric properties still emerge while fluorescence is retained. Fluorescence retention is optimized at 98.8% with a 8 monolayer CdS shell and saturation polarization and remnant polarization values are also retained at the same values.

For use in industrial applications, the same room temperature cation exchange reaction can be performed on non-toxic zinc blende quantum dots. Zinc selenide was first used because it is a common shelling material for non-toxic core-shell semiconductor nanocrystals. Tin (IV) was used in the cation exchange synthesis and the same methods for prevention of byproducts and aggregation were used as in the cadmium-based synthesis of ferroelectric nanocrystals.

Ferroelectric properties emerged with a saturation polarization of 77.5 $\mu C/cm^2$ and a remnant polarization of 11.3 $\mu C/cm^2$.

Overall, polarization values in all ferroelectric nanoparticles in which the cation exchange synthesis was performed remained at about 75 $\mu C/cm^2$. These values are much higher than $BaTiO_3$, a highly studied nanoferroelectric which exhibits polarization values around 15 $\mu C/cm^2$.[79] Other nanoferroelectrics with more complex syntheses exhibit a saturation polarization between 10 $\mu C/cm^2$ and 50 $\mu C/cm^2$.[29] While some of these values are closer to that of those synthesized in this work, these materials consistently have greater ferroelectricity than other nanoferroelectrics while retaining fluorescence and colloidal stability.

7.2 Future Directions

Optimization of ferroelectric semiconductor quantum dots formed through cation exchange in cadmium-based systems has been achieved. However, in order to use these materials in industrial applications, non-toxic materials must be used. Preliminary studies using ZnSe nanocrystals creates a steppingstone toward the synthesis of non-toxic, fluorescent, ferroelectric semiconductor nanocrystals. ZnSe is commonly used in shelling of InP fluorescent nanocrystals, which emit in the visible spectrum and can therefore be used in the same applications as CdSe QDs. Using the information gathered in the CdSe/CdS core-shell studies, one can infer that ferroelectricity can be induced in a protective ZnSe shell, preventing fluorescence quenching due to defects in the fluorescent InP core. This will allow for the use of fluorescent, ferroelectric QDs produced through a simple room-temperature cation exchange in industrial applications.

APPENDIX A

COMPOSITION AND CRYSTAL STRUCTURE DATA FOR GRADED ALLOY

NANOPARTICLES BEFORE AND AFTER CATION EXCHANGE

Following are TEM and STEM-EDS images and EDS quantification data studied in Chapter 3. Refer to Figures 3.3 and 3.5 for ferroelectric data corresponding to these QDs before and after cation exchange. Also included is XRD of CdSSe nanoparticles before and after cation exchange with varied cation identity, demonstrating peak broadening and decrease in peak intensity after each cation exchange reaction.

Figure A.1 TEM, STEM-EDS maps, and EDS spectrum showing the presence of cadmium, sulfur, and selenium in the original CdSSe nanoparticles.
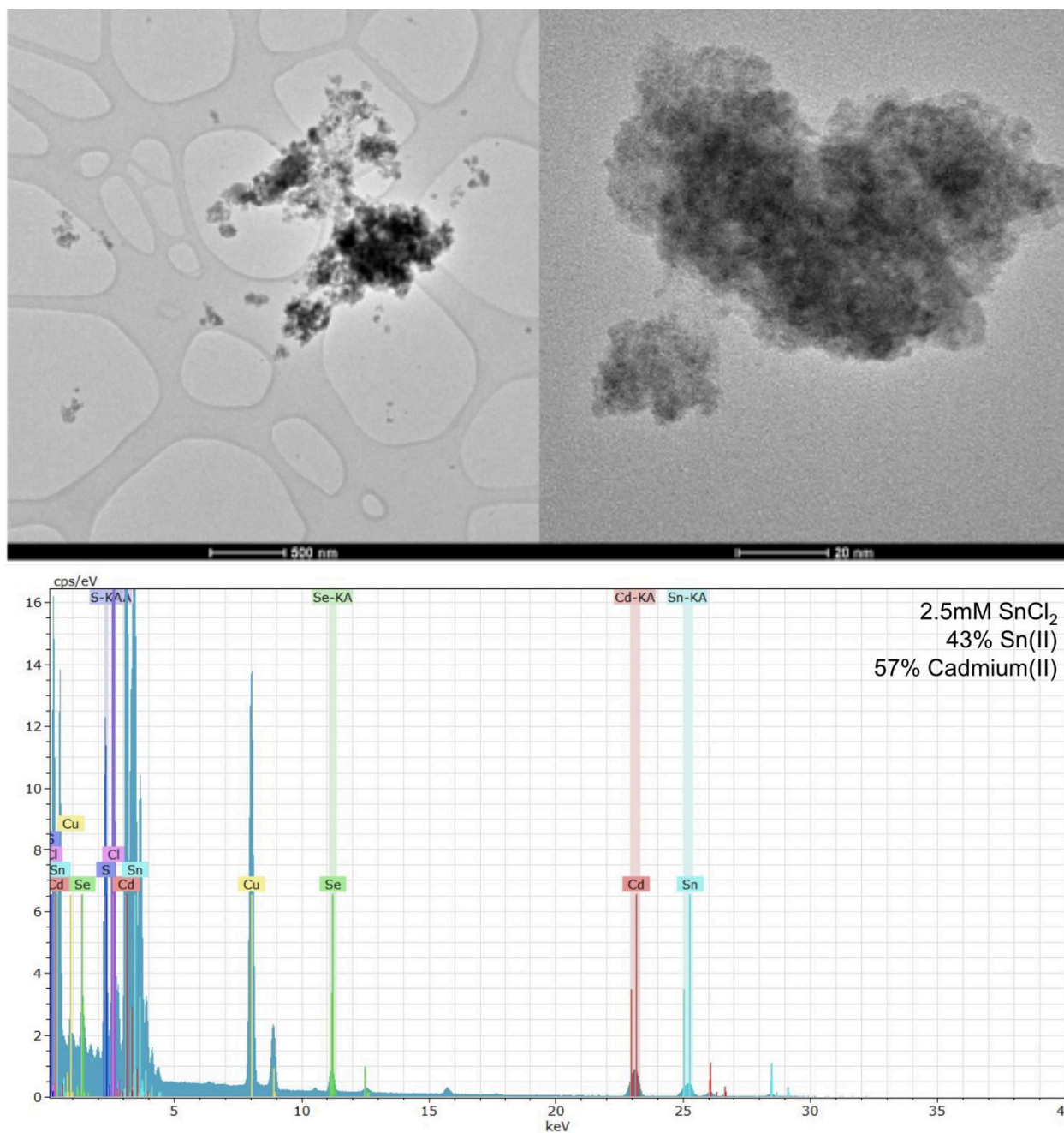
Figure A.2 TEM and EDS spectrum after tin (II) cation exchange showing aggregation as well as the presence of tin after cation exchange.
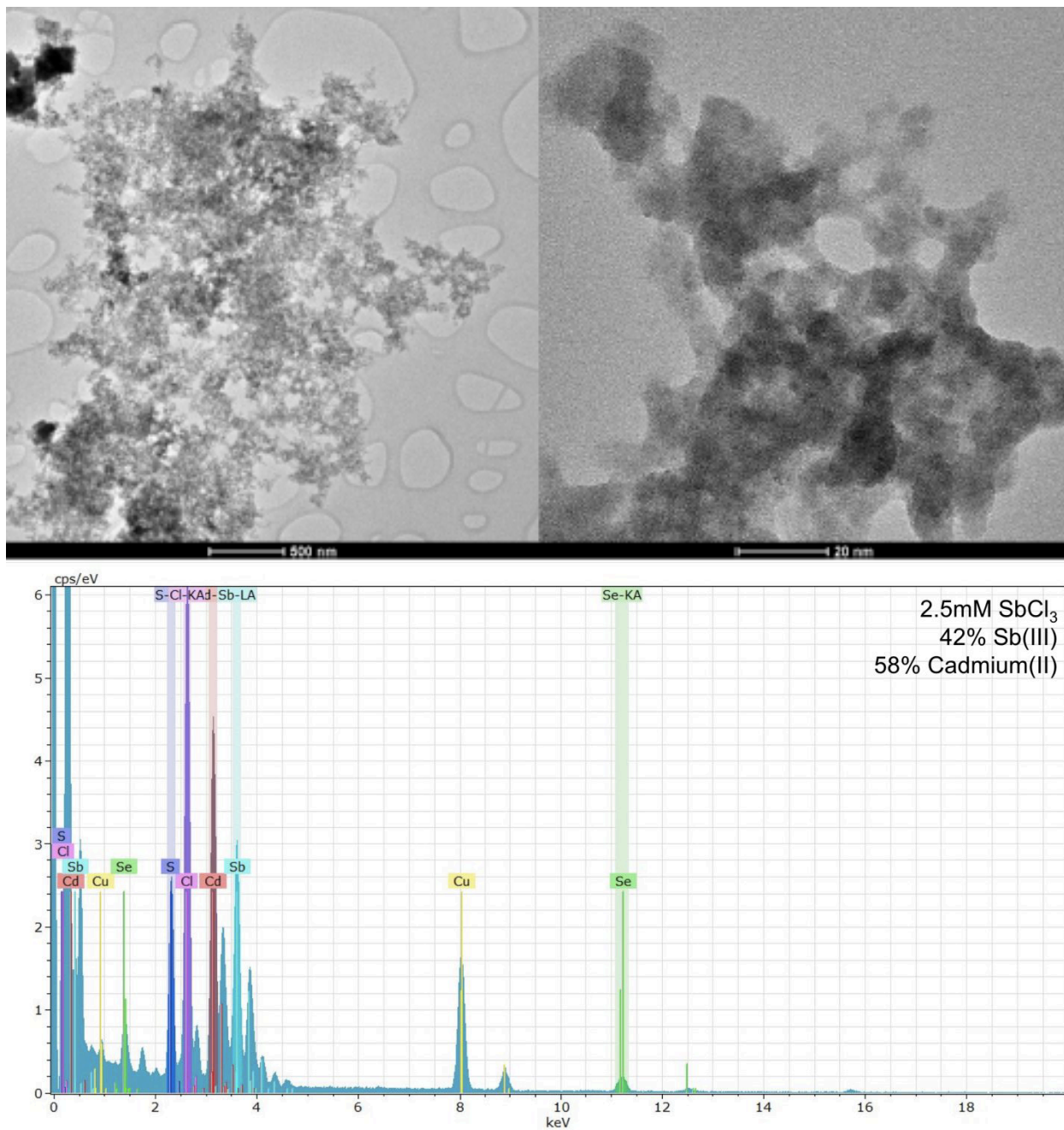
Figure A.3 TEM and EDS spectrum after antimony (III) cation exchange showing aggregation as well as the presence of antimony after cation exchange.
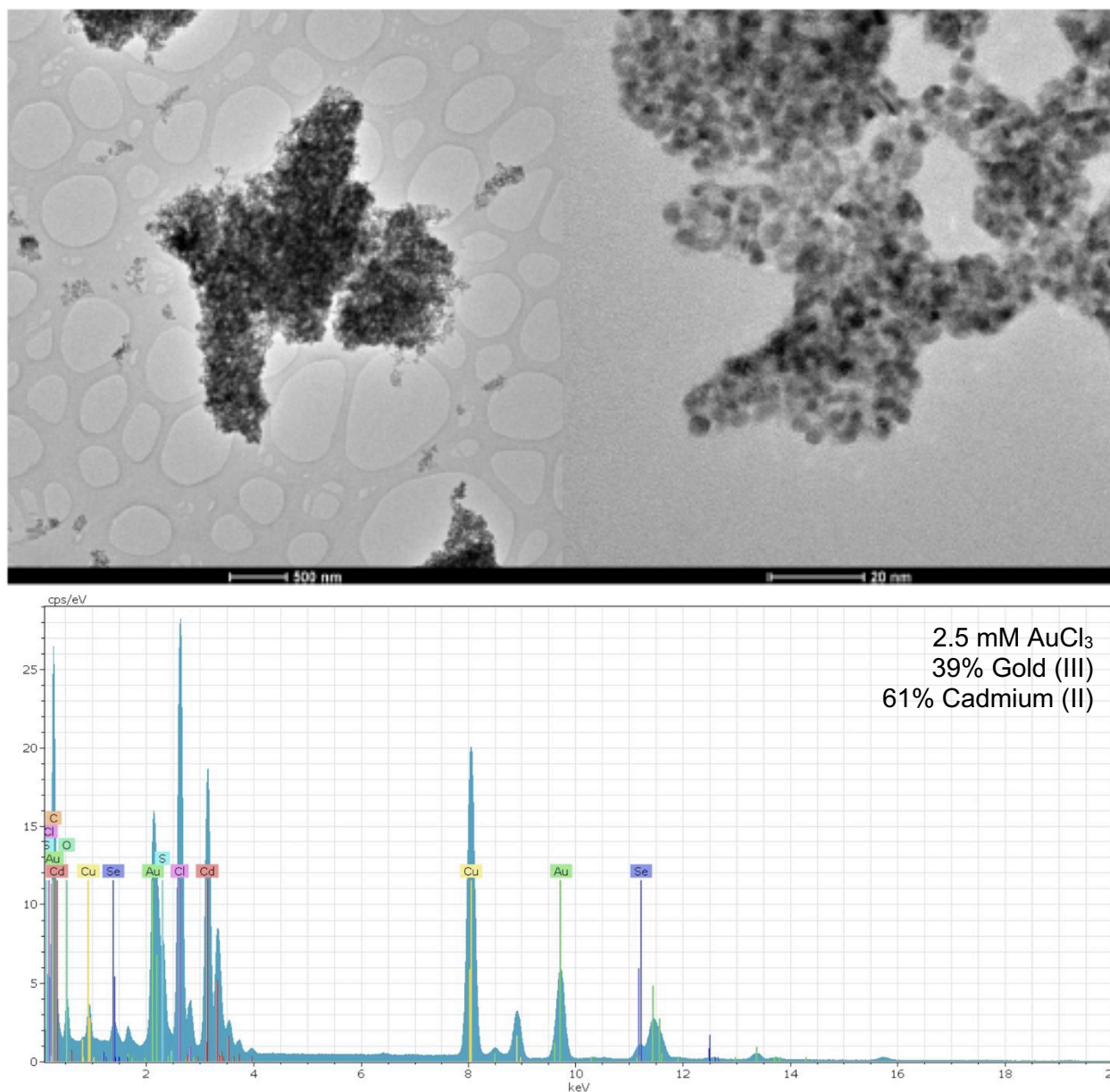
Figure A.4 TEM and EDS spectrum after gold (III) cation exchange showing aggregation as well as the presence of gold after cation exchange.
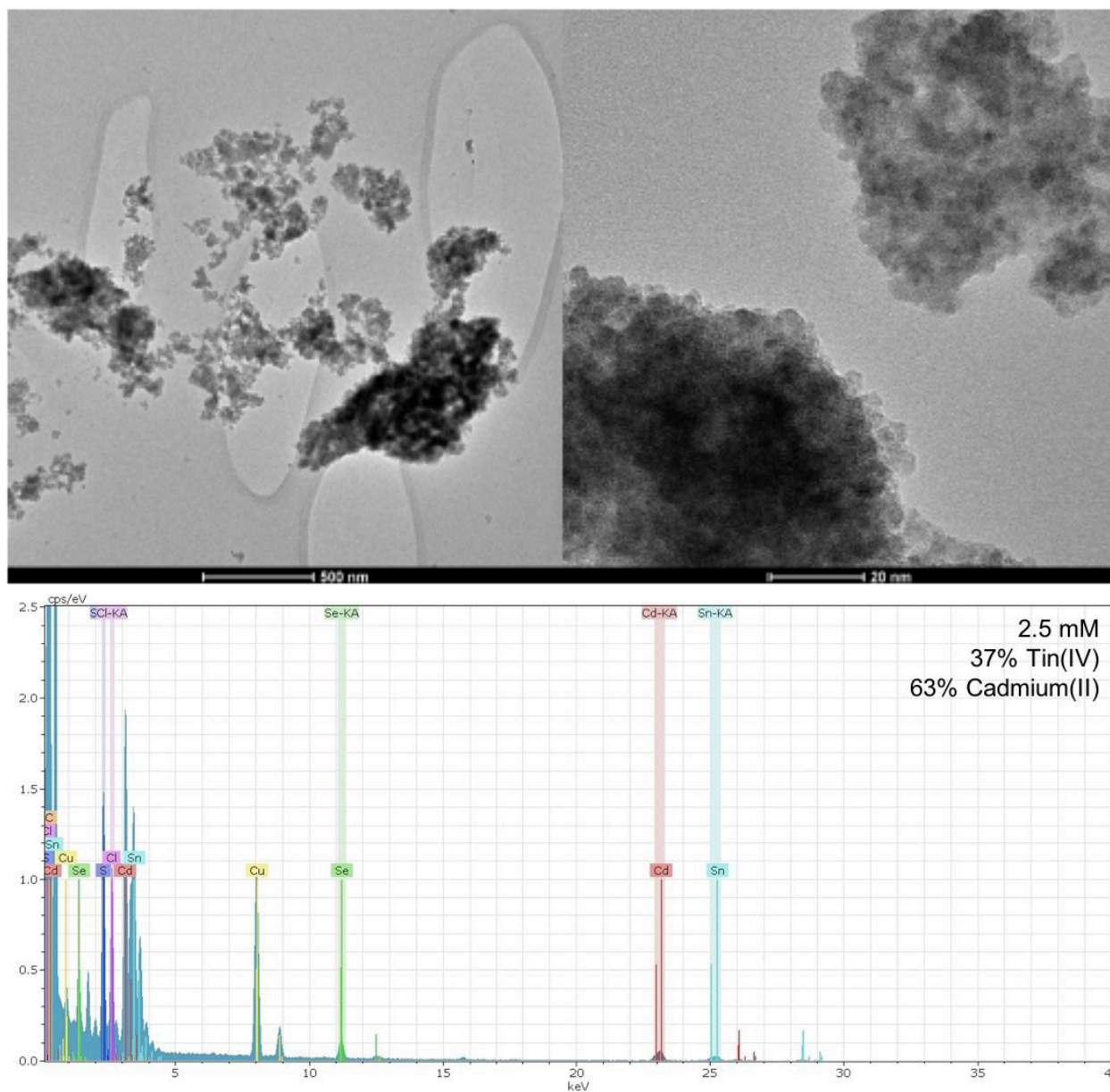
Figure A.5 TEM and EDS spectrum after tin (IV) cation exchange showing aggregation as well as the presence of tin after cation exchange.
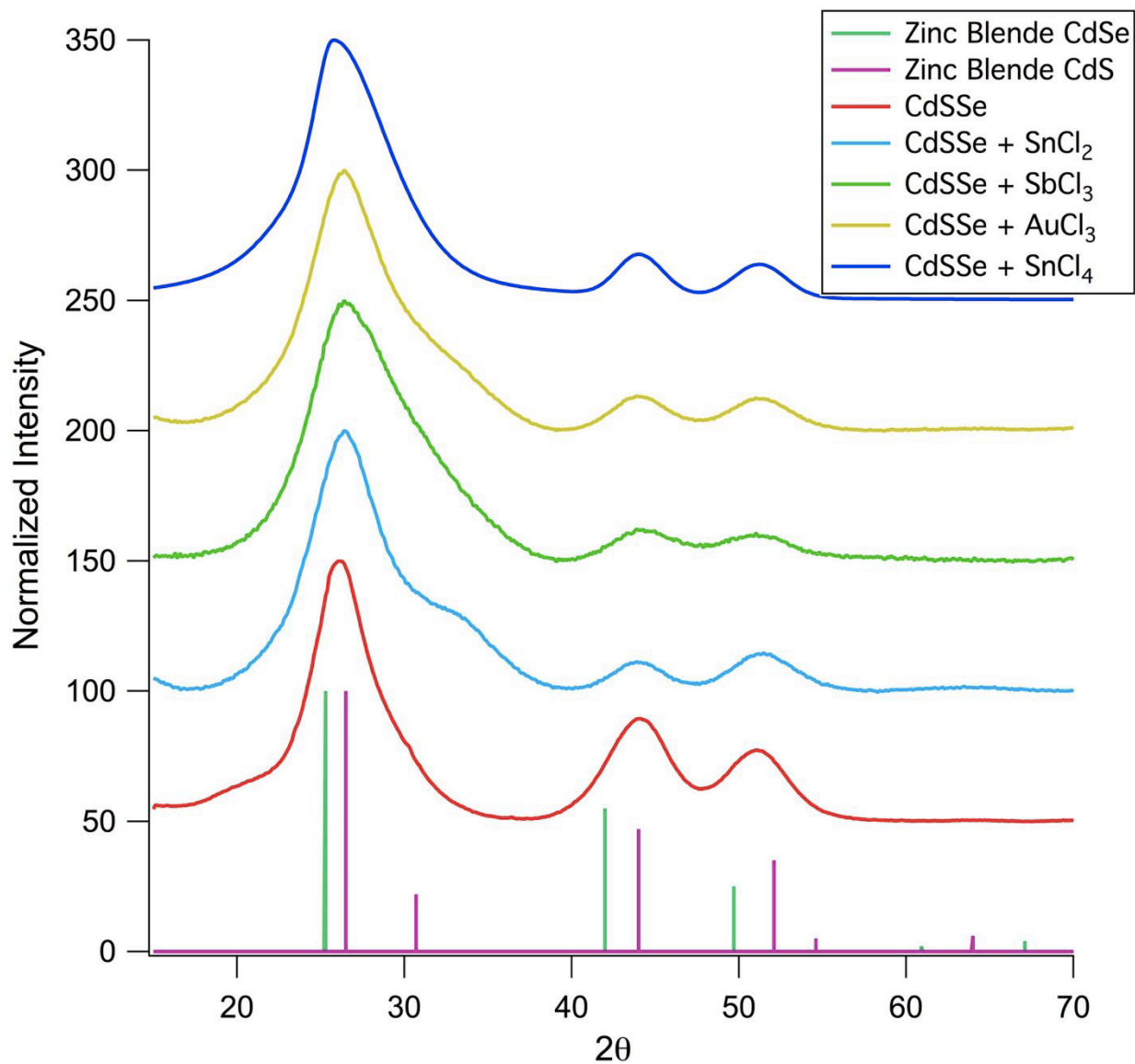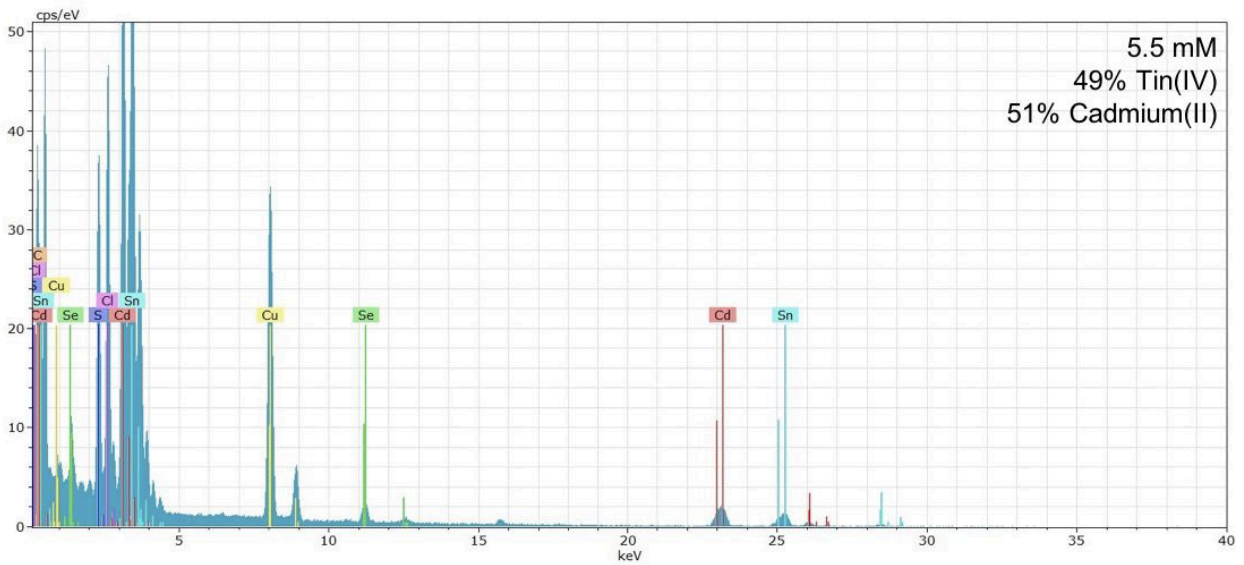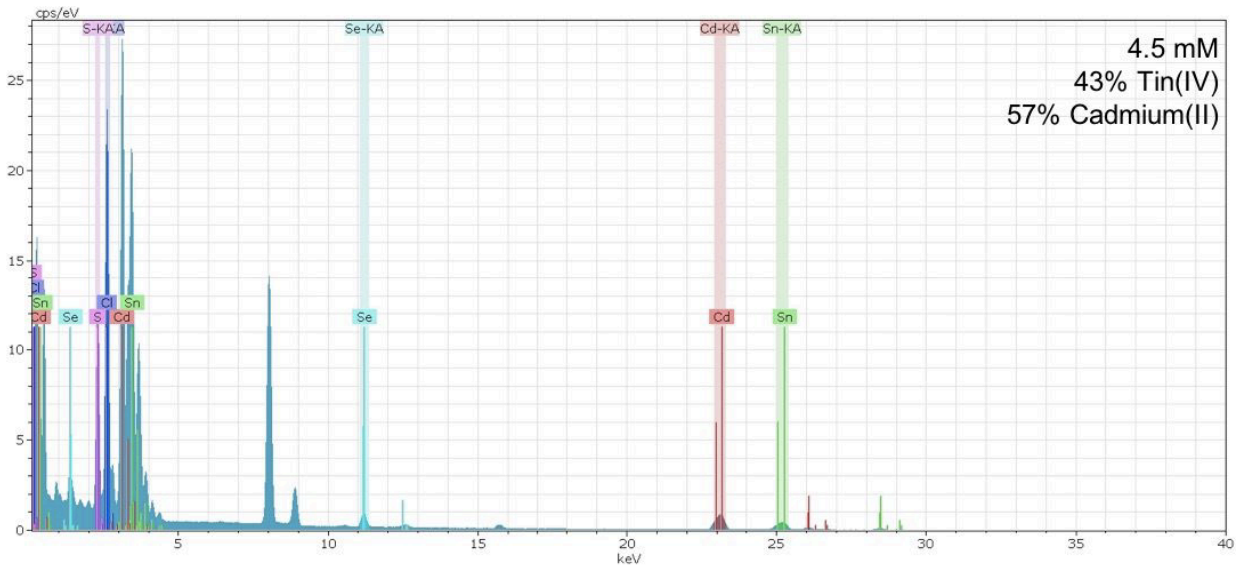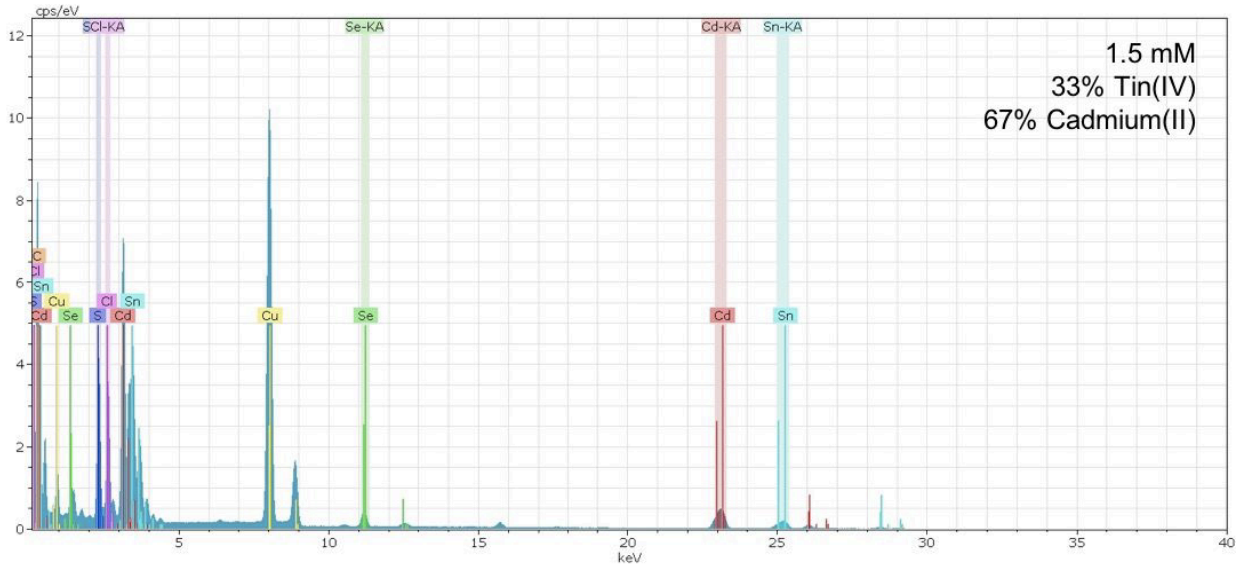
Figure A.6 XRD of CdSSe QDs before and after cation exchange with SnCl$_2$, SbCl$_3$, AuCl$_3$, and SnCl$_4$ salts.
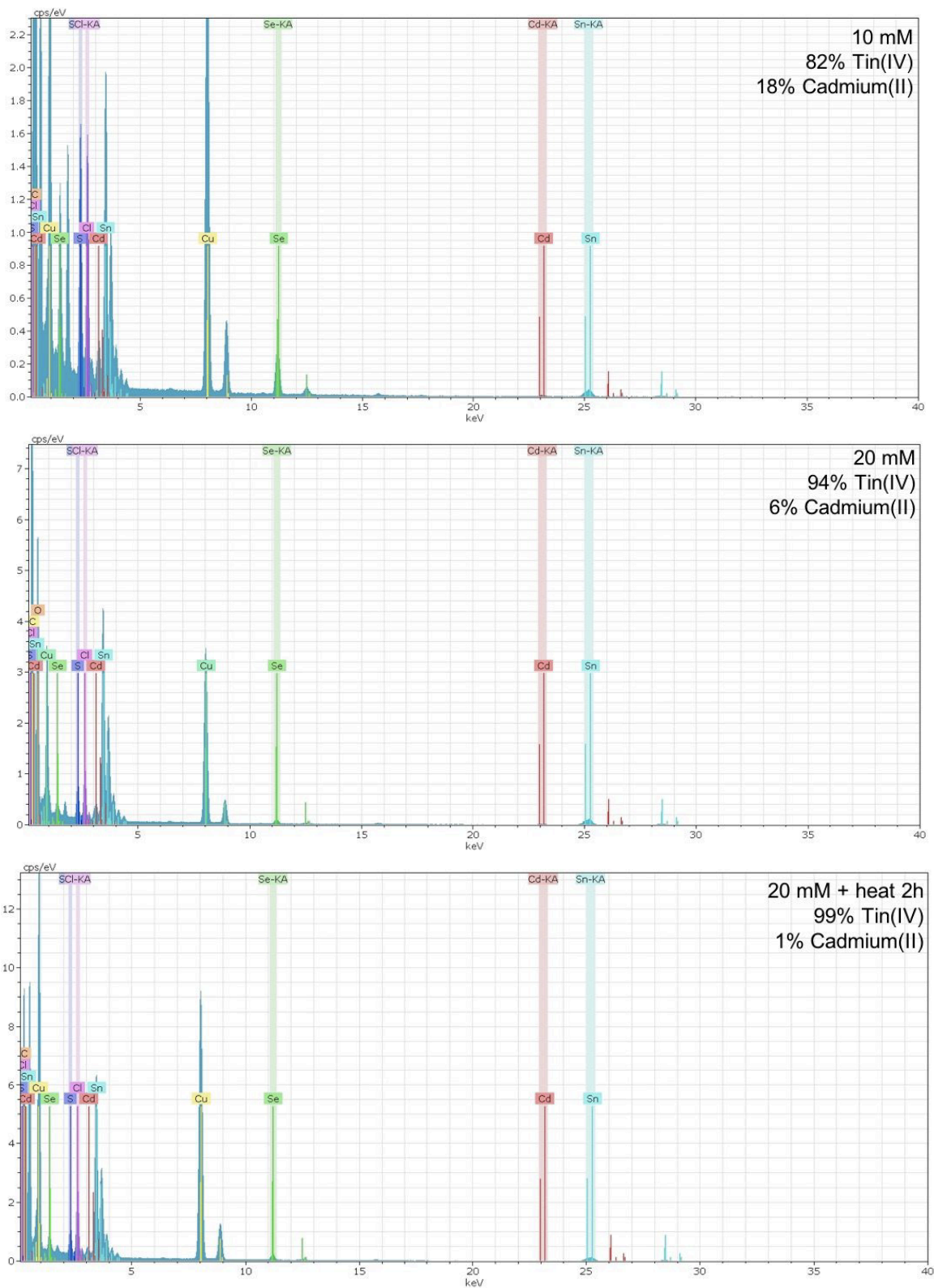
Figure A.7 STEM-EDS spectra quantification shows increase the ratio between tin(IV) and cadmium(II) with increase in tin(IV) chloride solution concentration used in the cation exchange reaction as well as heating in the final reaction.

APPENDIX B

PROOF OF THE EMERGENCE OF FERROELECTRIC PROPERTIES DUE TO CATION EXCHANGE RATHER THAN LIGAND DISPLACEMENT BY CHLORINE ANIONS

Further proof that ferroelectricity emerged due to cation exchange rather than the presence of chlorine was shown through similar experiments carried out with NaCl and SbI_3 salts. The NaCl experiments resulted in chlorine on the surface similar to the other metal chloride salt reactions, but no cation exchange reaction and no emergence of ferroelectricity. The SbI_3 experiments resulted in iodine on the surface as well as aggregation, but cation exchange still occurred and ferroelectric properties emerged.
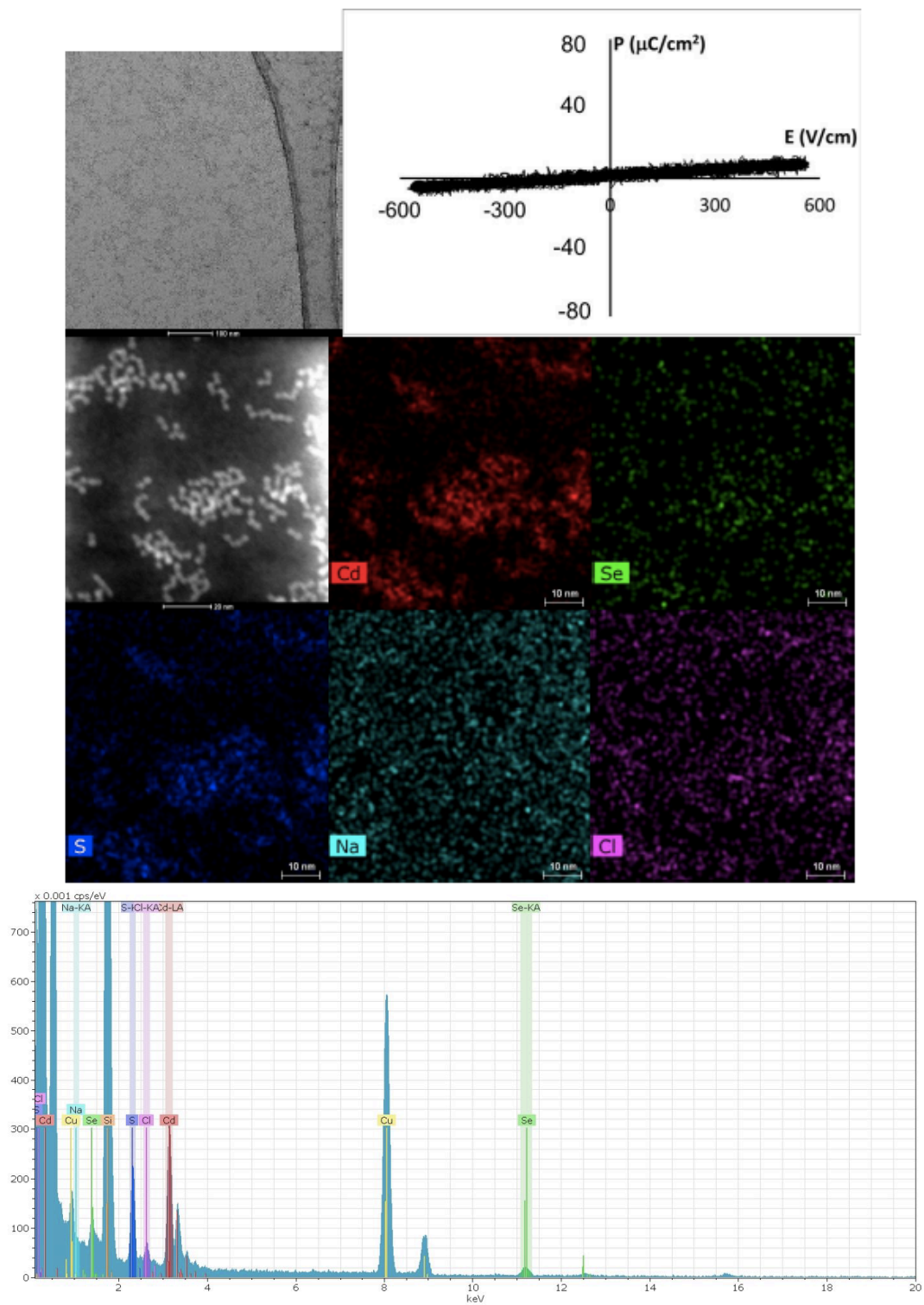
Figure B.1 TEM, STEM-EDS mapping, and EDS spectrum when cation exchange synthesis is performed with NaCl shows that sodium is not present, while aggregation still occurs and due to ligand displacement by chlorine. Sawyer-Tower circuit experiments show no ferroelectric properties.
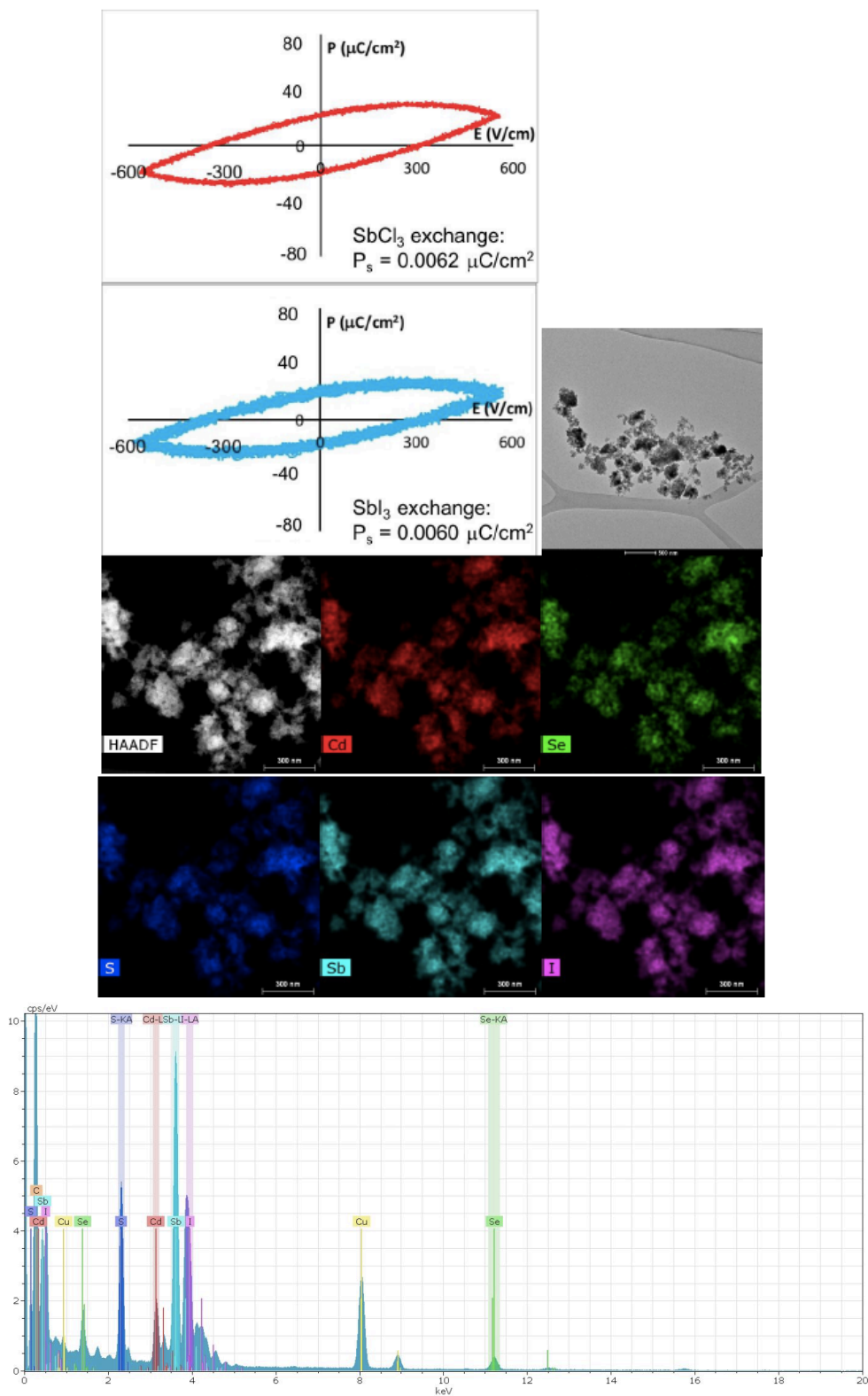
Figure B.2 Cation exchange synthesis with both antimony (III) chloride and antimony (III) iodide both result in aggregation and comparable ferroelectric properties. Aggregation is still believed to be due to ligand displacement by iodine shown by STEM-EDS mapping and the EDS spectrum.

APPENDIX C

COMPOSITION AND CRYSTAL STRUCTURE DATA FOR CORE-SHELL

NANOPARTICLES BEFORE AND AFTER CATION EXCHANGE

Following are TEM and STEM-EDS images and EDS quantification data studied in Chapter 5. Refer to Figures 5.3 for ferroelectric data corresponding to these QDs before and after cation exchange. Also included is XRD of CdSe nanoparticles before and after cation exchange with tin (IV), demonstrating peak broadening and decrease in peak intensity after cation exchange reaction.
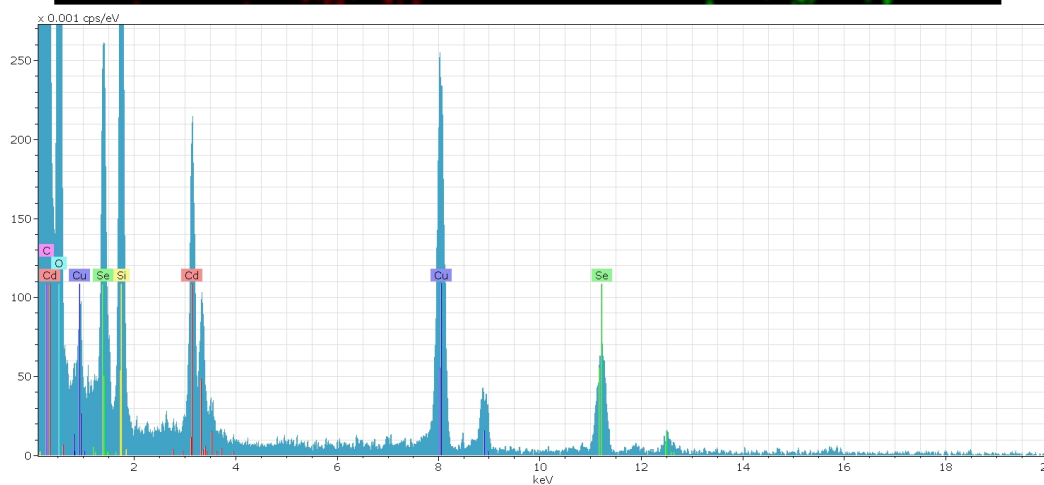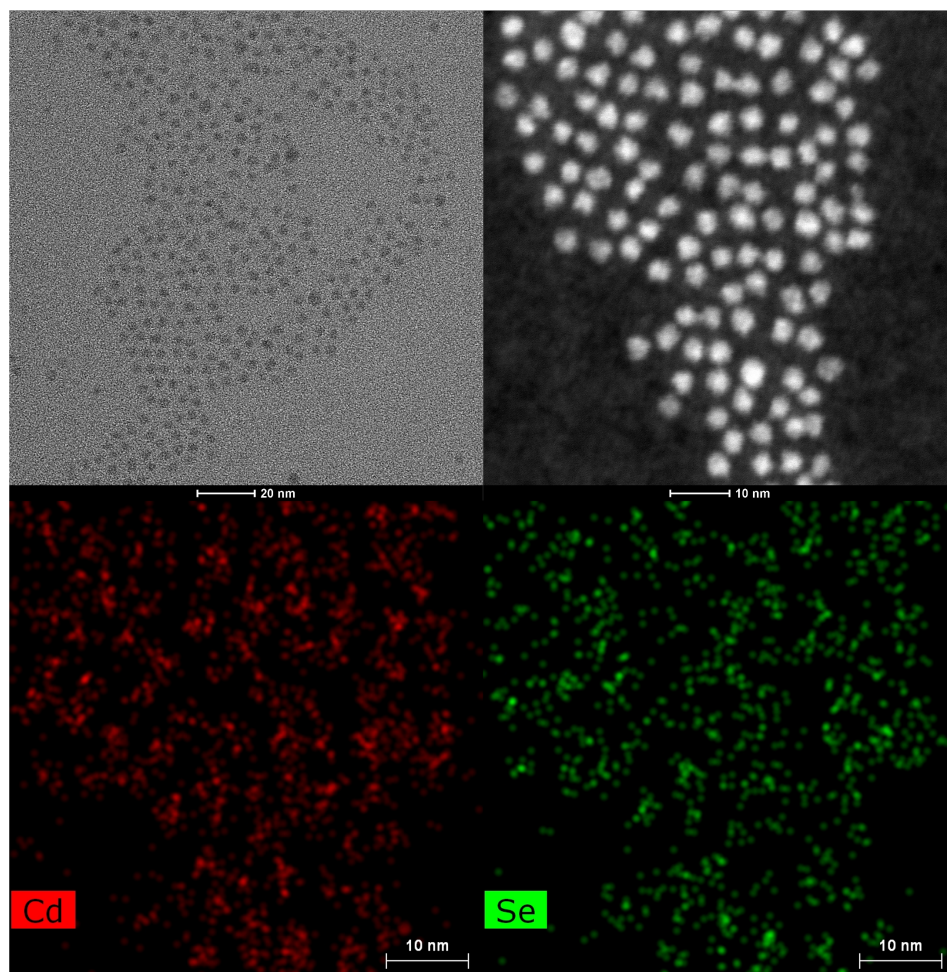
Figure C.1 STEM-EDS maps and EDS spectrum of CdSe nanoparticles showing the presence of cadmium and selenium.
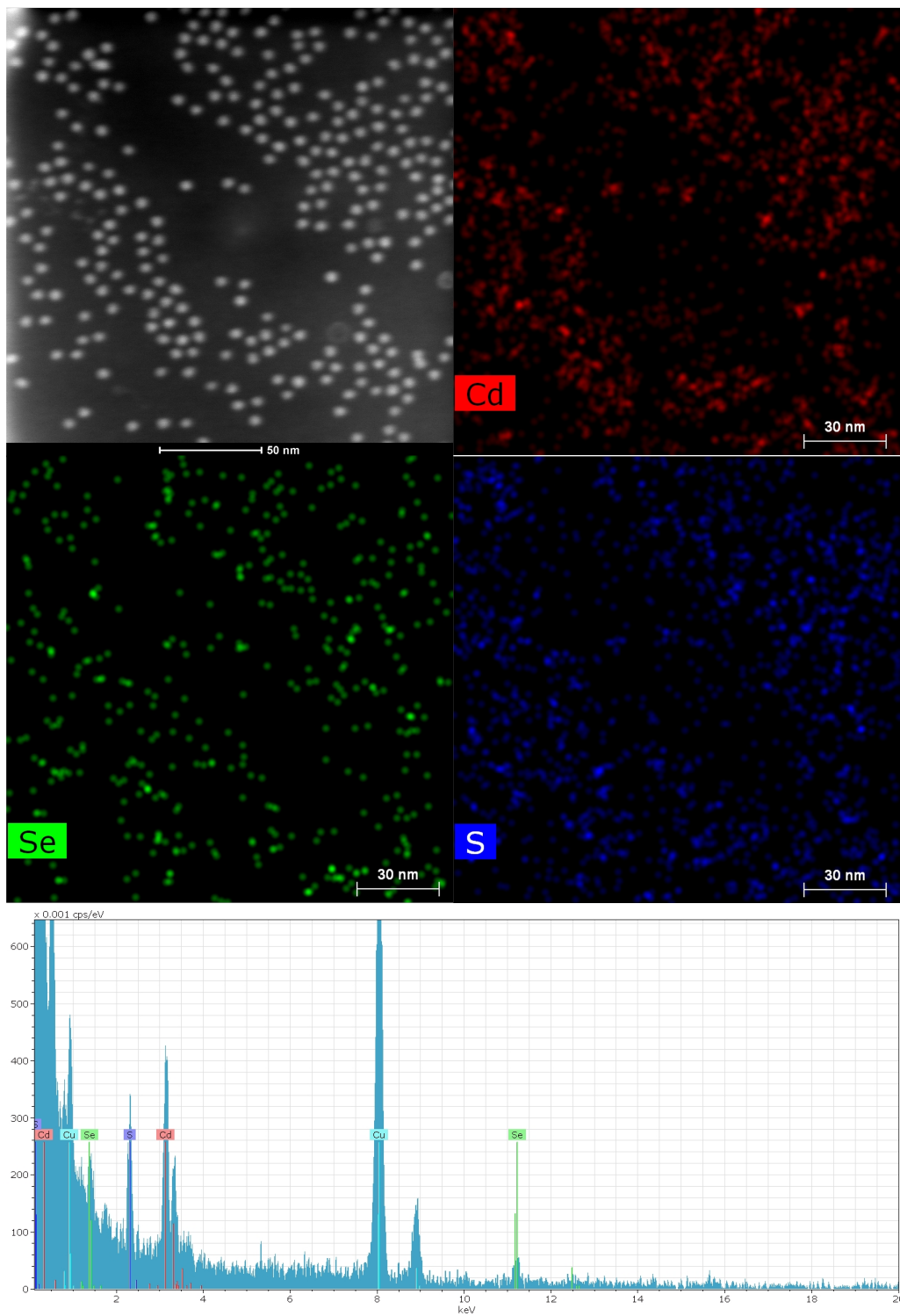
Figure C.2 STEM-EDS maps and EDS spectrum of CdSe/2CdS core-shell nanoparticles showing the presence of cadmium, sulfur, and selenium.
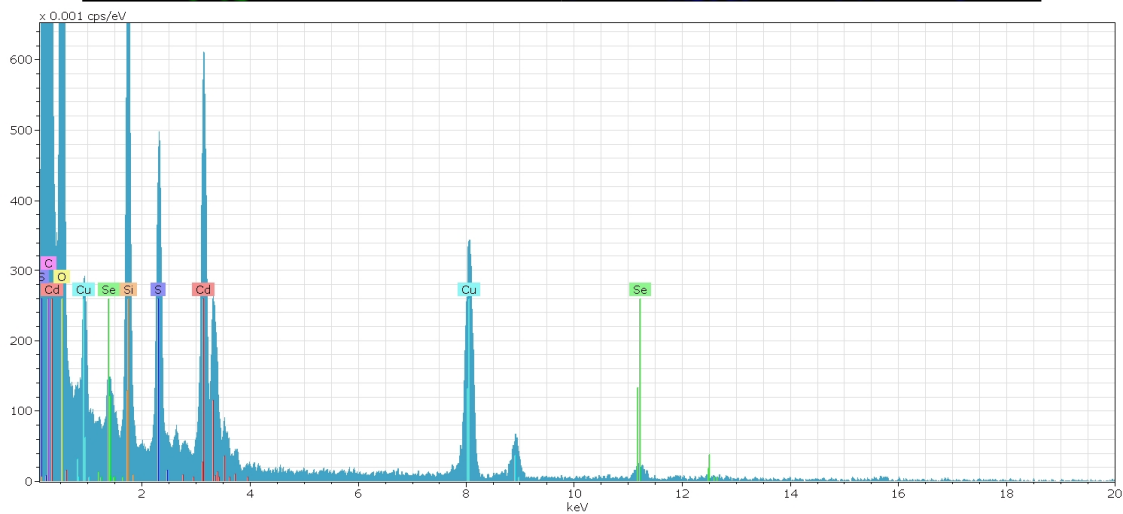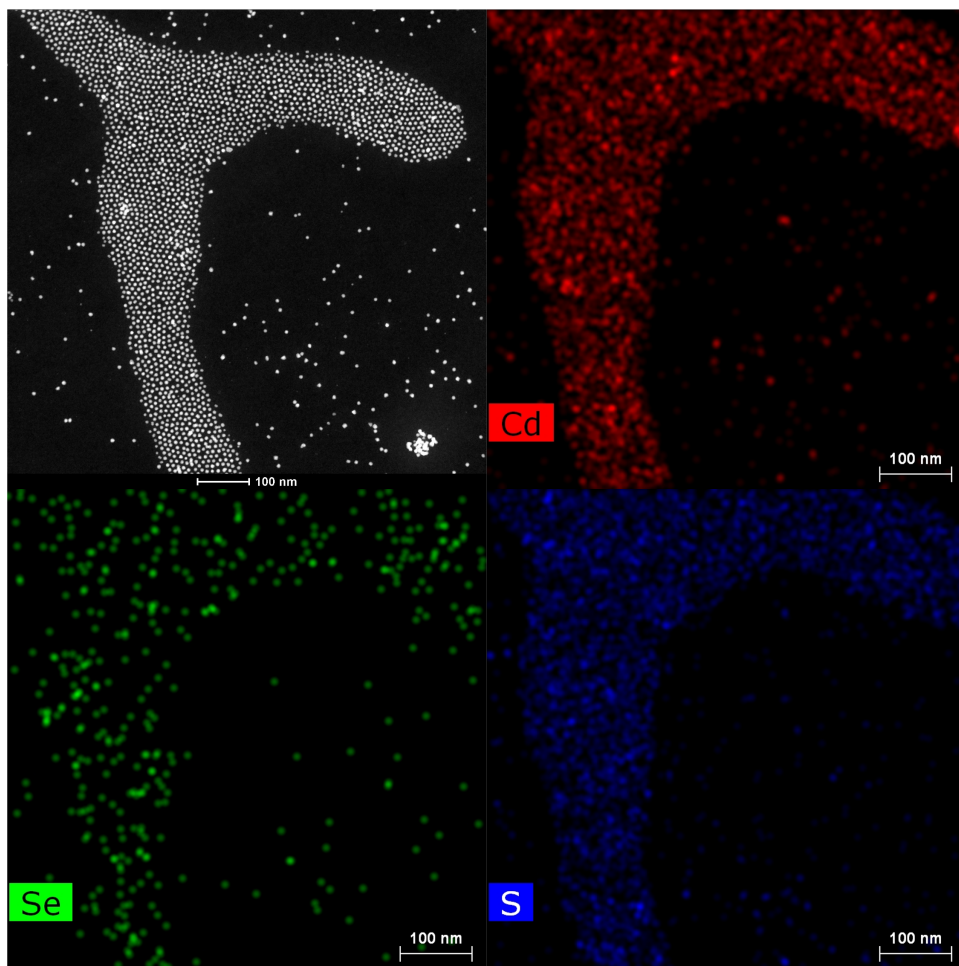
Figure C.3 STEM-EDS maps and EDS spectrum of CdSe/4CdS core-shell nanoparticles showing the presence of cadmium, sulfur, and selenium.
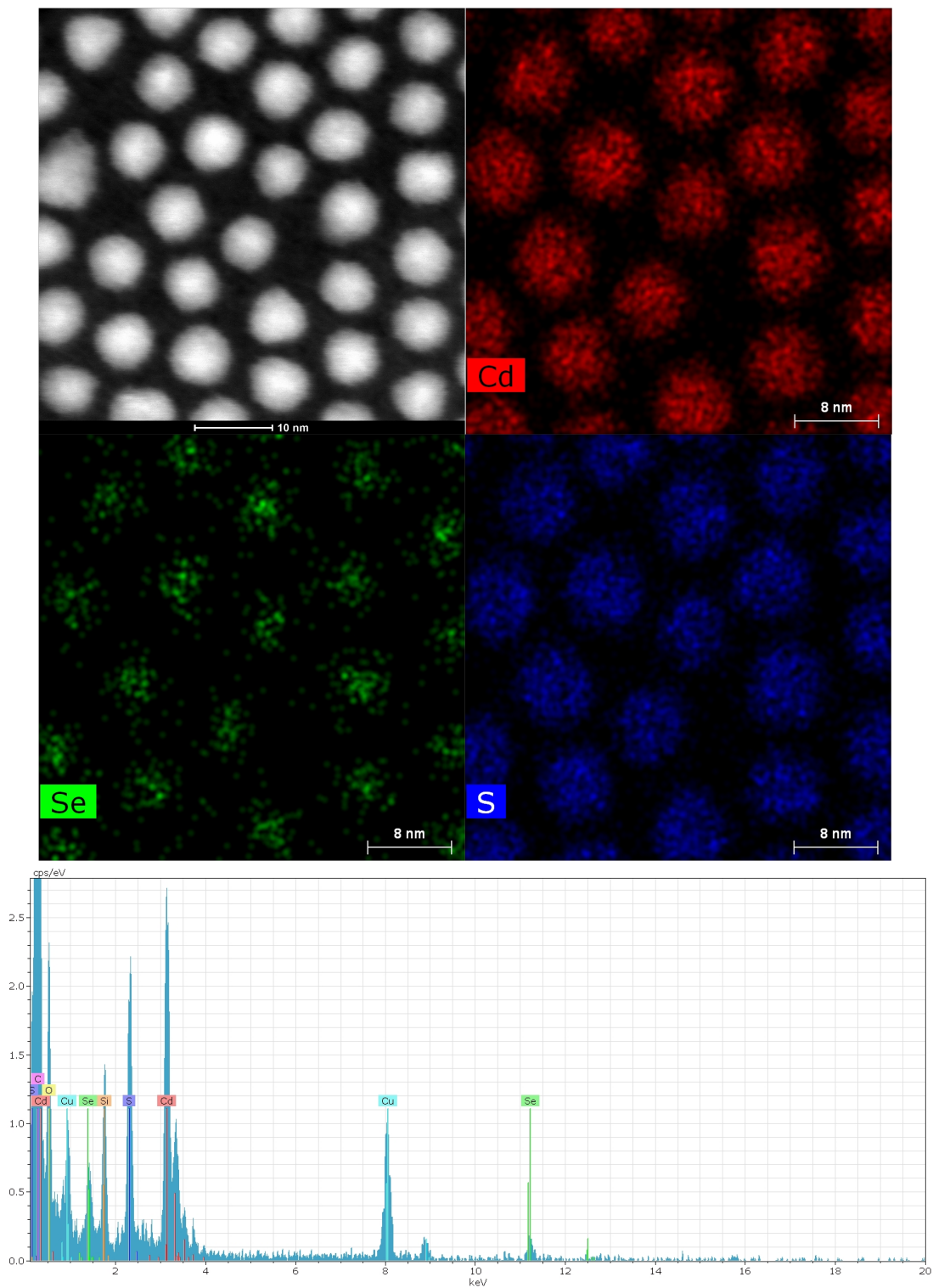
Figure C.4 STEM-EDS maps and EDS spectrum of CdSe/6CdS core-shell nanoparticles showing the presence of cadmium, sulfur, and selenium.
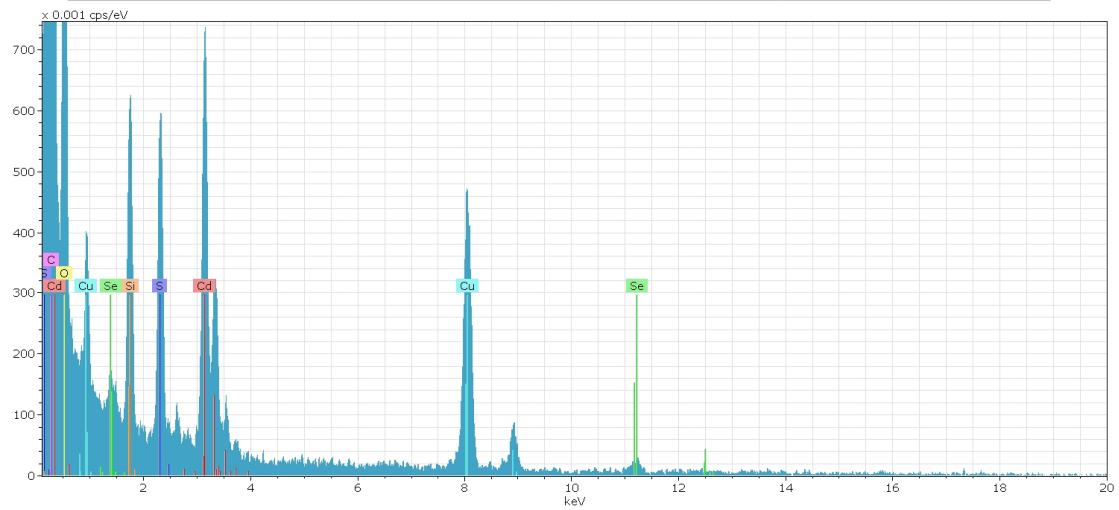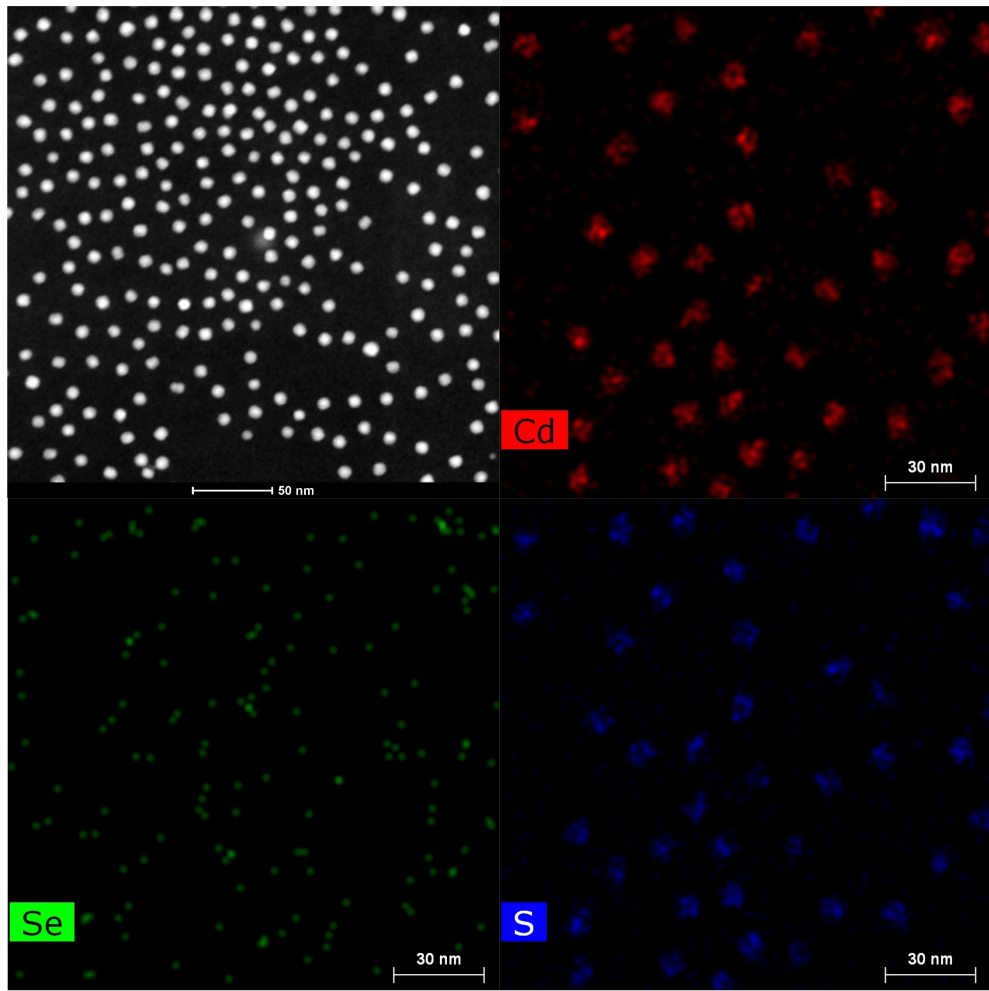
Figure C.5 STEM-EDS maps and EDS spectrum of CdSe/8CdS core-shell nanoparticles showing the presence of cadmium, sulfur, and selenium.
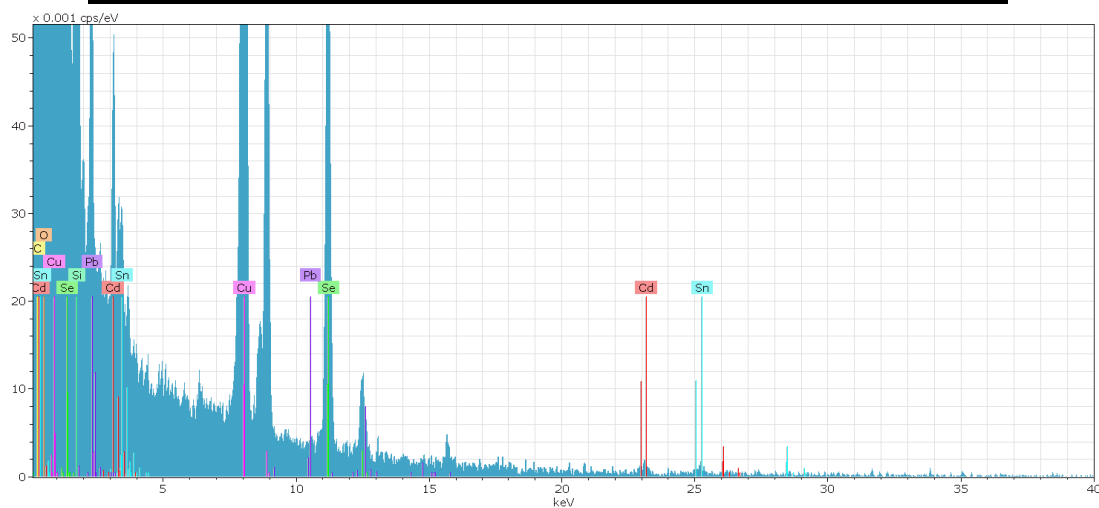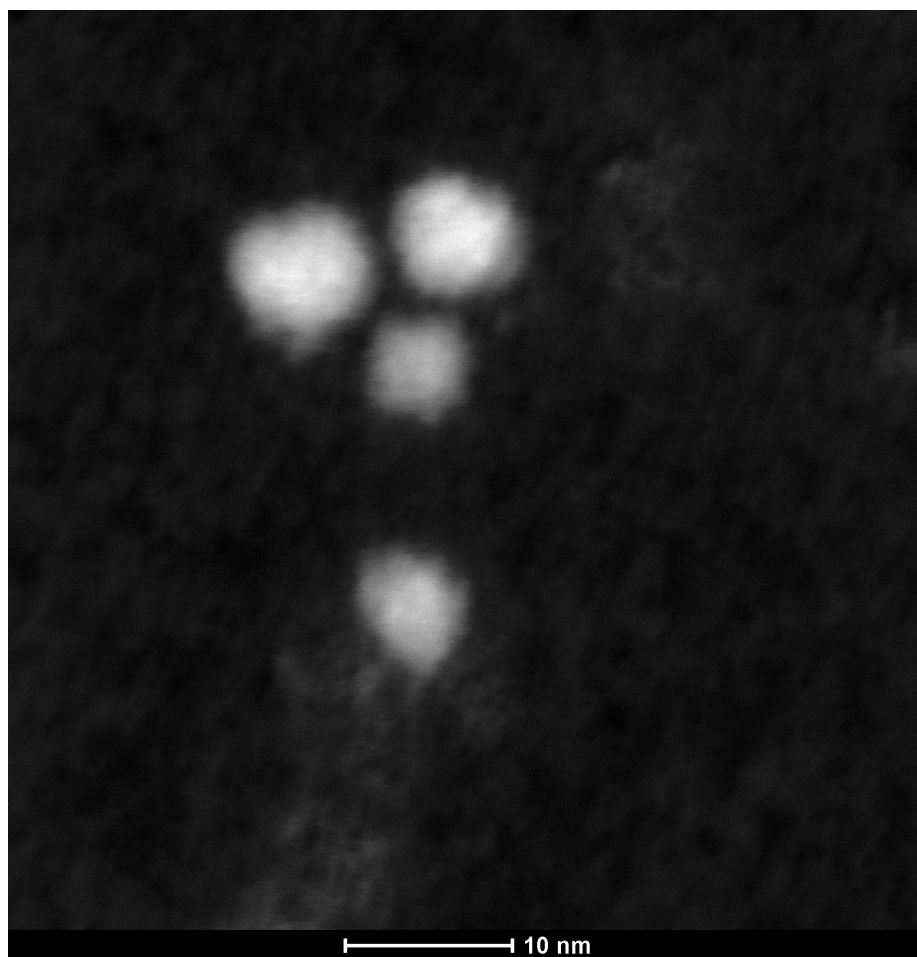
Figure C.6 HAADF and EDS spectrum of CdSe nanoparticles after tin(IV) cation exchange showing the presence of cadmium, selenium, and tin.
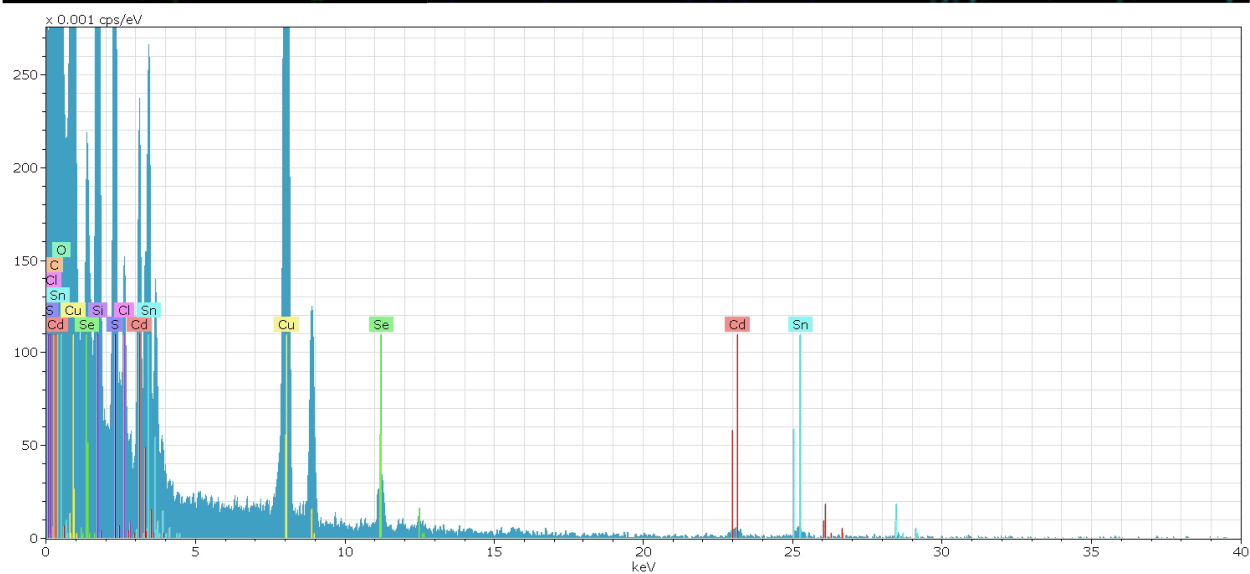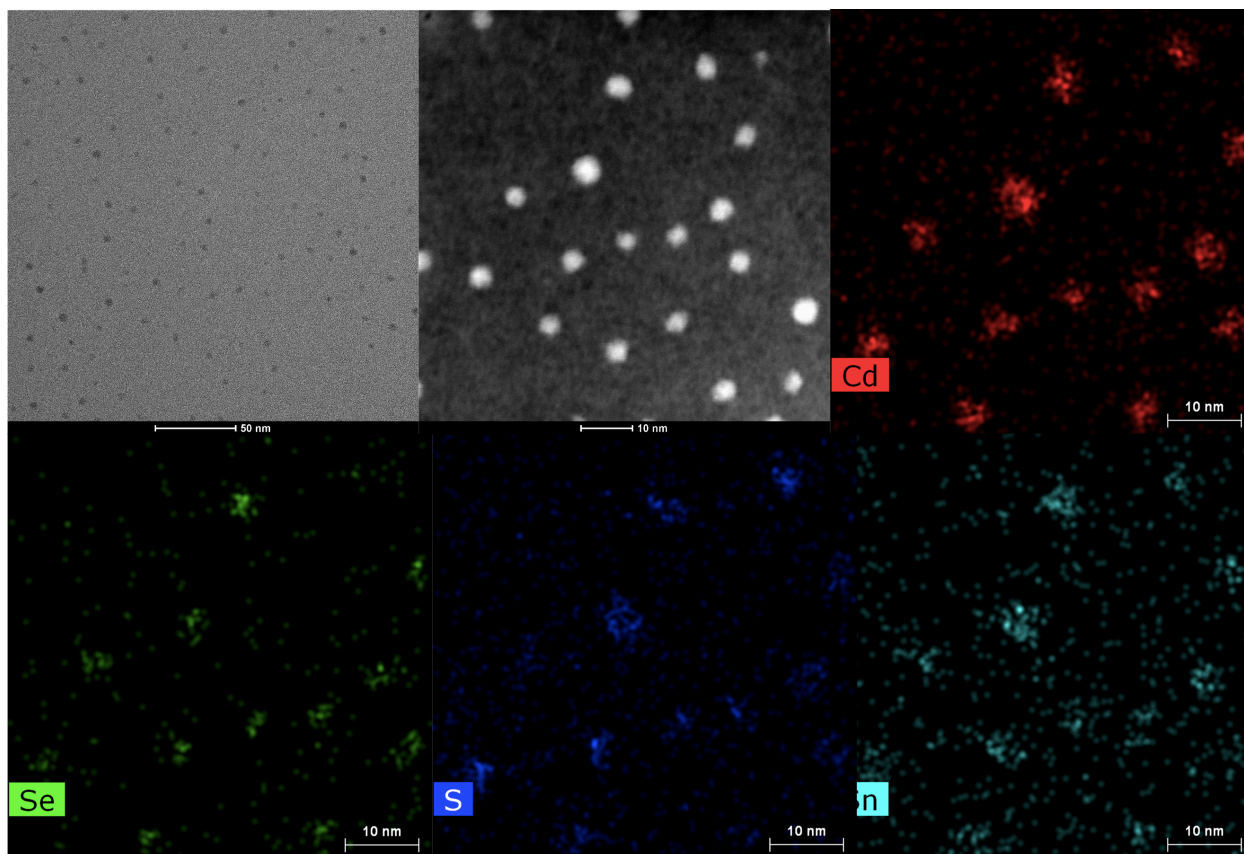
Figure C.7 STEM-EDS maps and EDS spectrum of CdSe/2CdS core-shell nanoparticles after tin(IV) cation exchange showing the presence of cadmium, selenium, sulfur, and tin.
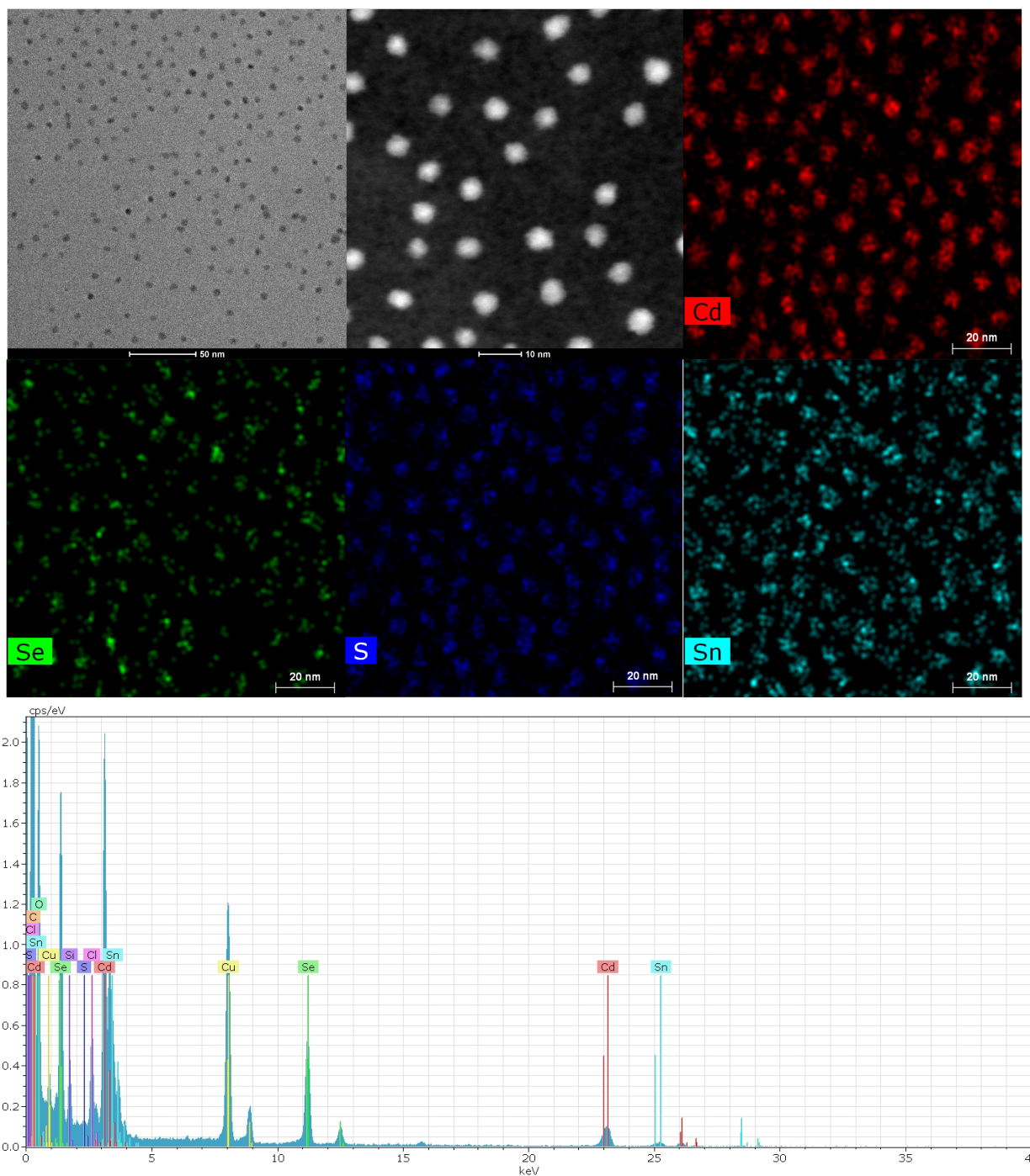
Figure C.8 STEM-EDS maps and EDS spectrum of CdSe/4CdS core-shell nanoparticles after tin(IV) cation exchange showing the presence of cadmium, selenium, sulfur, and tin.
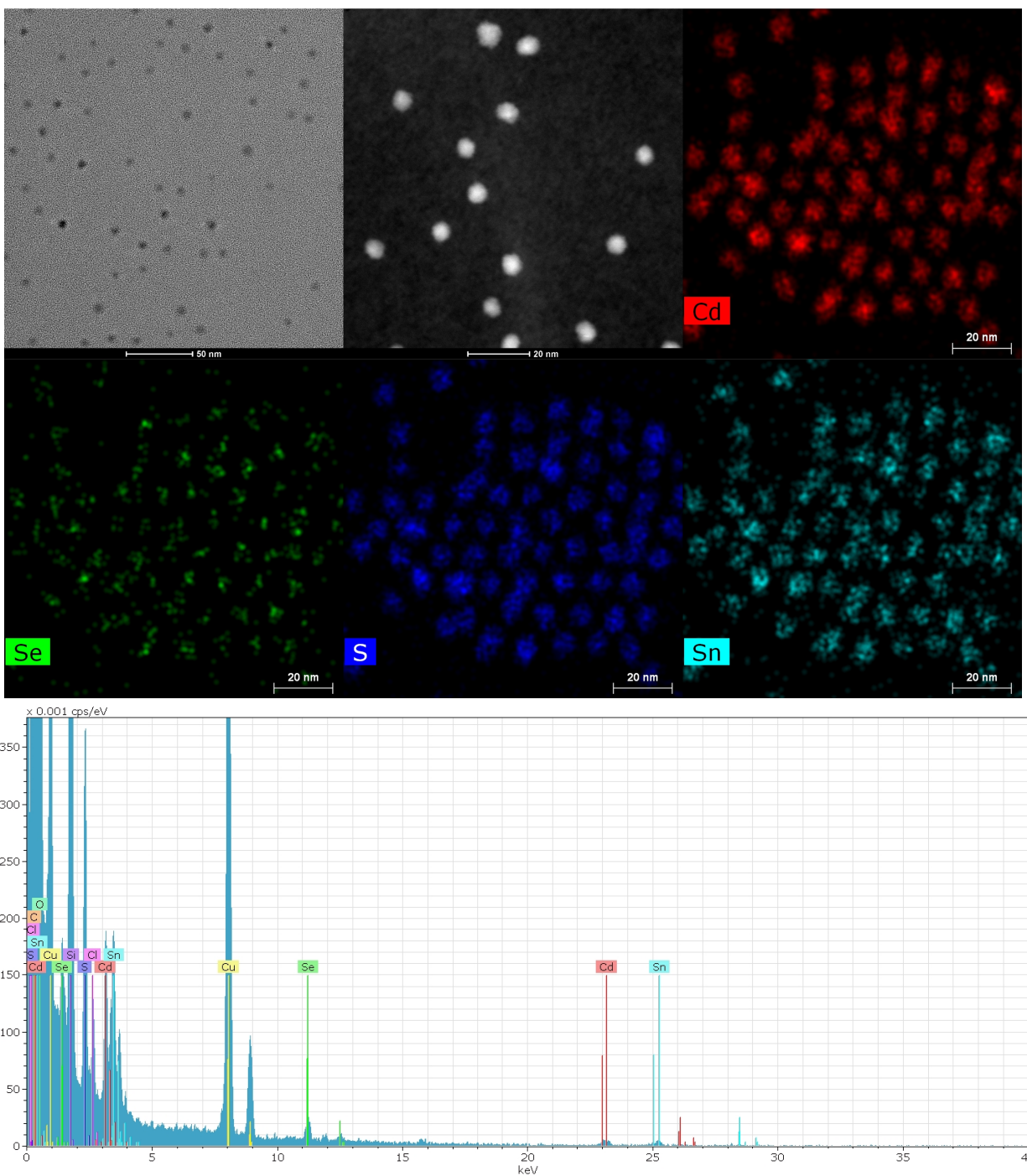
Figure C.9 STEM-EDS maps and EDS spectrum of CdSe/6CdS core-shell nanoparticles after tin(IV) cation exchange showing the presence of cadmium, selenium, sulfur, and tin.
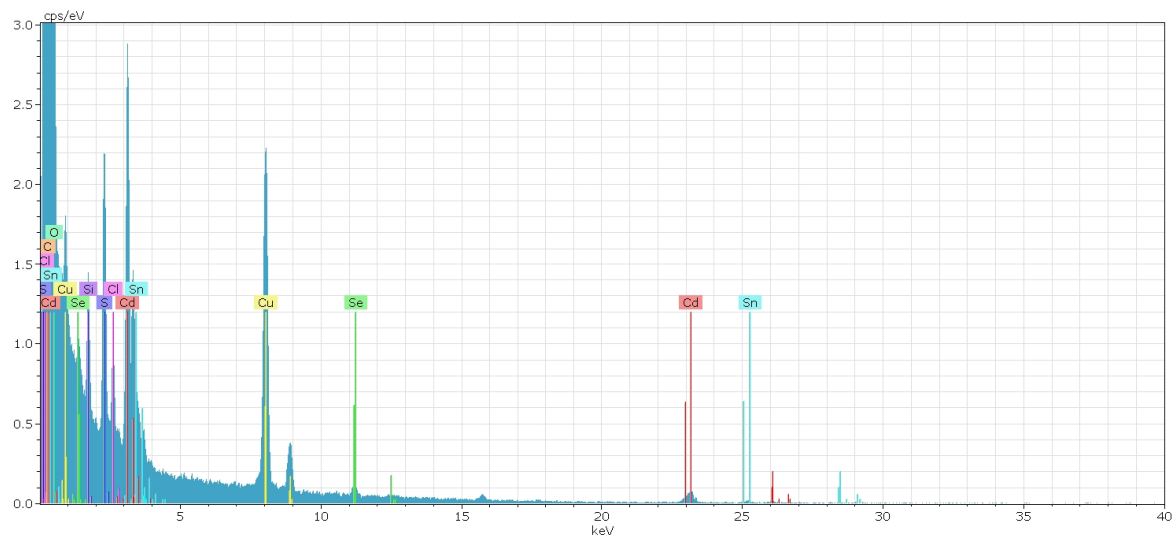
Figure C.10 EDS spectrum of CdSe/8CdS core-shell nanoparticles after tin(IV) cation exchange showing the presence of cadmium, selenium, sulfur, and tin.
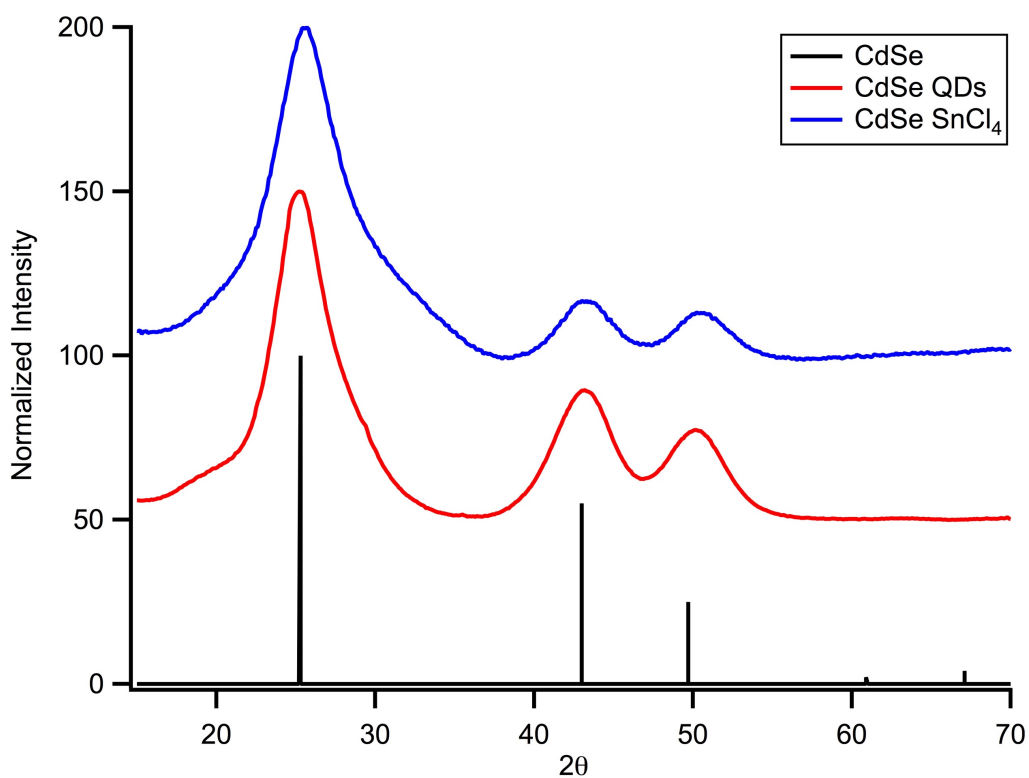
Figure C.11 XRD of CdSe QDs before and after cation exchange with tin(IV). With the introduction of tin(IV) into the crystal structure, disorder increases as shown by peak broadening and a decrease in relative intensities. The vertical bars are corresponding to JCPDS files for zinc blende CdSe no. 19.0191.

APPENDIX D

FERROELECTRICITY AND FLUORESCENCE IN CORE-SHELL NANOPARTICLES

BEFORE AND AFTER CATION EXCHANGE

Following is ferroelectric and fluorescence data for core-shell nanoparticles with increasing numbers of monolayers before and after cation exchange. This demonstrates retention of ferroelectricity with cation exchange in CdSe/2CdS, CdSe/4CdS, and CdSe/6CdS core-shell nanoparticles. Increase in fluorescence retention is also shown with increase in number of CdS monolayers.
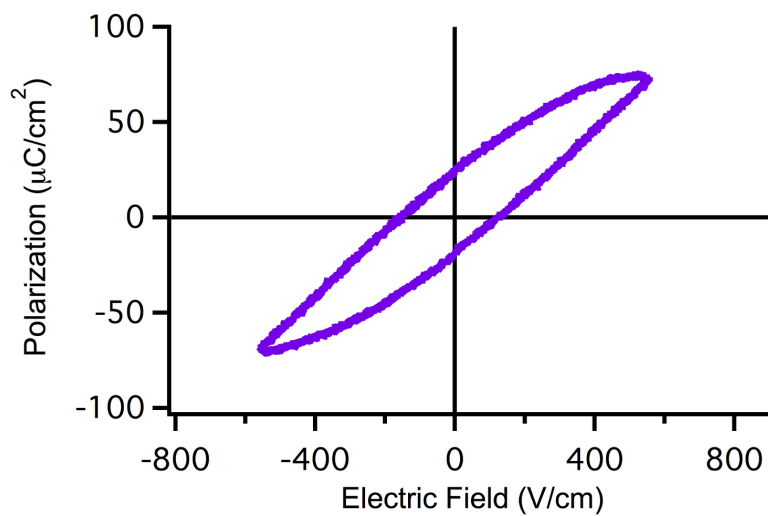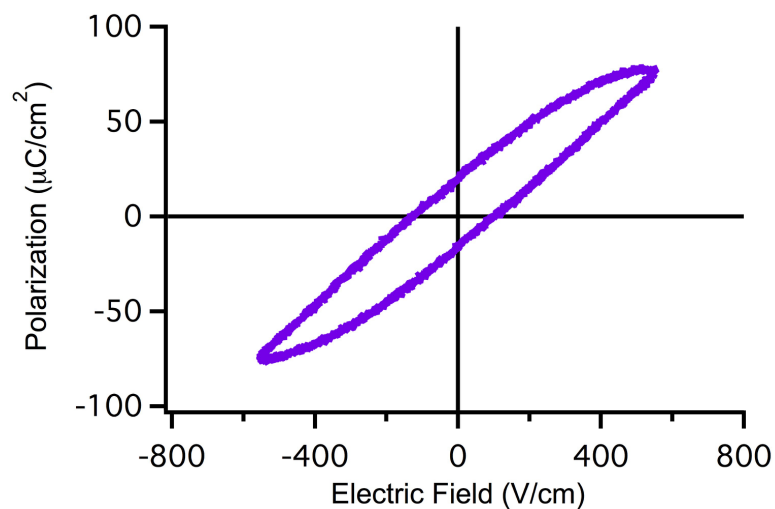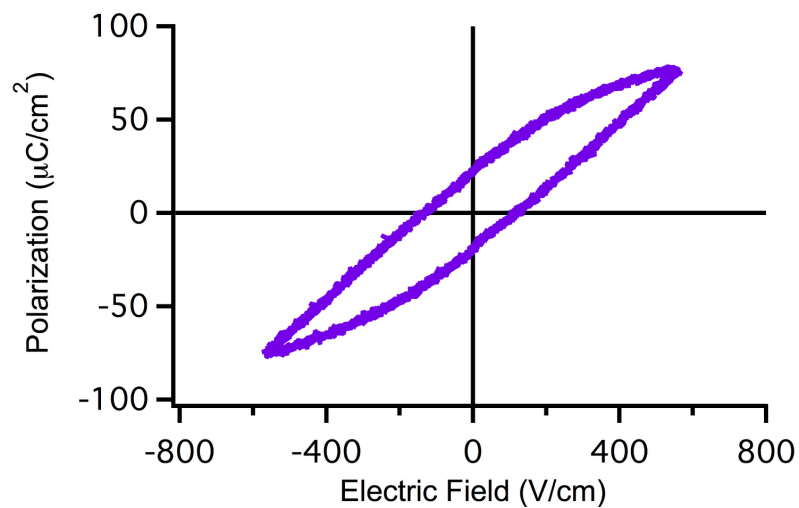
D.1 Polarization response within an applied electric field for a) CdSe/2CdS b) CdSe/4CdS and c) CdSe/6CdS core-shell QDs after tin(IV) cation exchange.
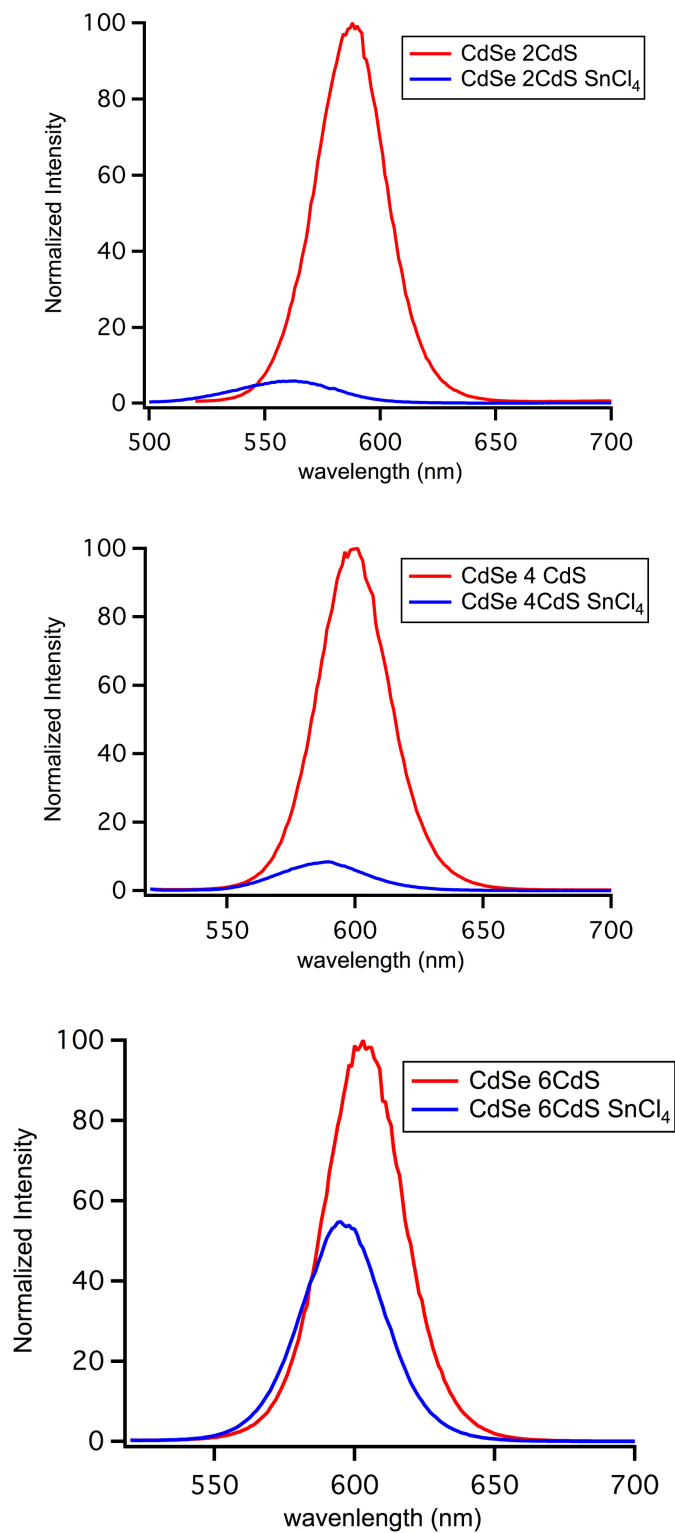
Figure D.2 Fluorescence spectra of (a) CdSe/2CdS (b) CdSe/4CdS and (c) CdSe/6CdS quantum dots before and after tin(IV) cation exchange.

REFERENCES

1. Brus, L. E., Electron–Electron and Electron-Hole Interactions in Small Semiconductor Crystallites: The Size Dependence of the Lowest Excited Electronic State. *J. Chem. Phys.* **1984**, *80 (9),* 4403-4409.

2. Scholes, G. D.; Rumbles, G., Excitons in Nanoscale Systems. *Nat. Mater*. **2006**, *5 (9),* 683-696.

3. Kagan, C. R.; Lifshitz, E.; Sargent, E. H.; Talapin, D. V., Building Devices from Colloidal Quantum Dots. *Science* **2016**, *353 (6302),* aac5523.

4. Rosenthal, S. J., Nanotechnology in Neuroscience Reveals Membrane Mobility Matters. *ACS Chem. Neurosci*. **2019**, *10 (1),* 30-32.

5. Kim, T. H.; Jun, S.; Cho, K. S.; Choi, B. L.; Jang, E., Bright and Stable Quantum Dots and Their Applications in Full-Color Displays. *MRS Bull*. **2013**, *38 (9),* 712-720.

6. Chang, J. C.; Rosenthal, S. J., A Bright Light to Reveal Mobility: Single Quantum Dot Tracking Reveals Membrane Dynamics and Cellular Mechanisms. *J Phys. Chem. Lett*. **2013**, *4 (17),* 2858-2866.

7. Fan, F.; Voznyy, O.; Sabatini, R. P.; Bicanic, K. T.; Adachi, M. M.; McBride, J. R.; Reid, K. R.; Park, Y.-S.; Li, X.; Jain, A.; Quintero-Bermudez, R.; Saravanapavanantham, M.; Liu, M.; Korkusinski, M.; Hawrylak, P.; Klimov, V. I.; Rosenthal, S. J.; Hoogland, S.; Sargent, E. H., Continuous-Wave Lasing in Colloidal Quantum Dot Solids Enabled by Facet-selective Epitaxy. *Nature* **2017**, *544,* 75.

8. Frecker, T.; Bailey, D.; Arzeta-Ferrer, X.; McBride, J.; Rosenthal, S. J., Review—Quantum Dots and Their Application in Lighting, Displays, and Biology. *ECS J. Solid State Sci. Technol.* **2016**, *5 (1),* R3019-R3031.

9. Sargent, E. H., Colloidal Quantum Dot Solar Cells. *Nat. Photonics* **2012**, *6 (3),* 133-135.

10. Shirasaki, Y.; Supran, G. J.; Bawendi, M. G.; Bulović, V., Emergence of Colloidal QuantumDot Light-Emitting Technologies. *Nat. Photonics* **2012**, *7,* 13-23.

11. Schreuder, M. A.; Xiao, K.; Ivanov, I. N.; Weiss, S. M.; Rosenthal, S. J. White Light-Emitting Diodes Based on Ultrasmall CdSe Nanocrystal Electroluminescence. *Nano Lett.* **2010**, *10,* 573− 576.

12. Anikeeva, P. O.; Halpert, J. E.; Bawendi, M. G.; Bulovic, V.́ Quantum Dot Light-Emitting Devices with Electroluminescence Tunable Over the Entire Visible Spectrum. *Nano Lett.* **2009**, *9,* 2532−2536.

13. Rosenthal, S. J.; Chang, J. C.; Kovtun, O.; McBride, J. R.; Tomlinson, I. D. Biocompatible Quantum Dots for Biological Applications. *Chem. Biol*. **2011**, *18*, 10−24.

14. Kovtun, O.; Tomlinson, I. D.; Bailey, D. M.; Thal, L. B.; Ross, E. J.; Harris, L.; Frankland, M. P.; Ferguson, R. S.; Glaser, Z.; Greer, J.; Rosenthal, S. J. Single Quantum Dot Tracking Illuminates Neuroscience at the Nanoscale. *Chem. Phys. Lett*. **2018**, *706*, 741− 752.

15. Ng, A.; Poplawsky, J. D.; Li, C.; Pennycook, S. J.; Rosenthal, S. J. Direct Electronic Property Imaging of a Nanocrystal-Based Photovoltaic Device by Electron Beam-Induced Current via Scanning Electron Microscopy. *J. Phys. Chem. Lett*. **2014**, *5*, 856−860.

16. Bronstein, N. D.; Yao, Y.; Xu, L.; O'Brien, E.; Powers, A. S.; Ferry, V. E.; Alivisatos, A. P.; Nuzzo, R. G. Quantum Dot Luminescent Concentrator Cavity Exhibiting 30-Fold Concentration. *ACS Photonics* **2015**, *2*, 1576−1583.

17. Park, Y.-S.; Lim, J.; Klimov, V. I. Asymmetrically Strained Quantum Dots with Non-Fluctuating Single-Dot Emission Spectra and Subthermal Room-Temperature Linewidths. *Nat. Mater*. **2019**, *18*, 249−255.

18. Dukes, A. D; McBride, J. R.; Rosenthal, S. Luminescent Quantum Dots. *ECS Trans*. **2011**, *33*, 3.

19. Kippeny, T.; Swafford, L. A.; Rosenthal, S. J., Semiconductor Nanocrystals: A Powerful Visual Aid for Introducing the Particle in a Box. *J. Chem. Educ*. **2002**, *79 (9),* 1094. 10.

20. Efros, A. L.; Rosen, M.; Kuno, M.; Nirmal, M.; Norris, D. J.; Bawendi, M., Band-Edge Exciton in Quantum Dots of Semiconductors with a Degenerate Valence Band: Dark and Bright Exciton States. *Phys. Rev. B* **1996**, *54 (7),* 4843-4856. 11.

21. Bowers, M. J.; McBride, J. R.; Rosenthal, S. J., White-Light Emission from Magic-Sized Cadmium Selenide Nanocrystals. *J. Am. Chem. Soc*. **2005,** *127 (44)*, 15378-15379.

22. Li, Y.; Hou, X.; Dai, X.; Yao, Z.; Lv, L.; Jin, Y.; Peng, X. Stoichiometry-Controlled InP Based Quantum Dots: Synthesis, Photoluminescence, and Electroluminescence. *J. Am. Chem. Soc*. **2019**, *141*, 6448-6452.

23. Tessier, M. D.; Baquero, E. A.; Dupont, D.; Grigel, V.; Bladt, E.; Bals, S.; Coppel, Y.; Hens, Z.; Nayral, C.; Delpech, F. Interfacial Oxidation and Photoluminescence of InPBased Core/Shell Quantum Dots. *Chem. Mat*. **2018**, *30*, 6877-6883.

24. Hahm, D.; Chang, J. H.; Jeong, B. G.; Park, P.; Kim, J.; Lee, S.; Choi, J.; Kim, W. D.; Rhee, S.; Lim, J.; Lee, D. C.; Lee, C.; Char, K.; Bae, W. K. Design Principle for Bright, Robust, and Color-Pure InP/ZnSexS1-x/ZnS Heterostructures. *Chem. Mat*. **2019**, *31*, 2476-2484.

25. Cao, F.; Wang, S.; Wang, F.; Wu, Q.; Zhao, D.; Yang, X. A Layer-by-Layer Growth Strategy for Large-Size InP/ZnSe/ZnS Core-Shell Quantum Dots Enabling High-Efficiency Light-Emitting Diodes. *Chem. Mater*. **2018**, *30*, 8002-8007.

26. Kim, Y.; Ham, S.; Jang, H.; Min, J. H.; Chung, H.; Lee, J.; Kim, D.; Jang, E. Bright and Uniform Green Light Emitting InP/ZnSe/ZnS Quantum Dots for Wide Color Gamut Displays. *Appl. Nano Mater*. **2019**, *2*, 1496-1504.

27. Brodu, A.; Ballottin, M. V.; Buhot, J.; van Harten, E. J.; Dupont, D.; La Porta, A.; Prins, P. T.; Tessier, M. D.; Versteegh, M. A. M.; Zwiller, V.; Bals, S.; Hens, Z.; Rabouw, F. T.; Christianen, P. C. M.; Donego, C. D., Vanmaekelbergh, D. Exciton Fine Structure and Lattice Dynamics in InP/ZnSe Core/Shell Quantum Dots. *ACS Photonics* **2018**, *5*, 3353-3362.

28. Rafipoor, M.; Dupont, D.; Tornatzky, H.; Tessier, M. D.; Maultzsch, J.; Hens, Z.; Lange, H. Strain Engineering in InP/(Zn,Cd)Se Core/Shell Quantum Dots. *Chem. Mater*. **2018**, *30*, 4393-4400.

29. Varghese, J.; Whatmore, R. W.; Holmes, J. D. Ferroelectric Nanoparticles, Wires and Tubes: Synthesis, Characterisation and Applications. *J. Mater. Chem. C* **2013**, *1*, 2618−2640.

30. Scott, J. F. Applications of Modern Ferroelectrics. *Science* **2007**, *315*, 954−959.

31. Parizi, S. S.; Mellinger, A.; Caruntu, G. Ferroelectric Barium Titanate Nanocubes as Capacitive Building Blocks for Energy Storage Applications. *ACS Appl. Mater. Interfaces* **2014**, *6*, 17506−17517.

32. Derbenwick, G. F.; Isaacson, A. F. Ferroelectric Memory: On the Brink of Breaking Through. *IEEE Circuits Devices Mag*. **2001**, *17*, 20− 30.

33. Takasu, H. The Ferroelectric Memory and its Applications. *J. Electroceram*. **2000**, *4*, 327−338.

34. Auciello, O.; Scott, J. F.; Ramesh, R. The Physics of Ferroelectric Memories. *Phys. Today* **1998**, *51*, 22−27.

35. Kohlstedt, H.; Mustafa, Y.; Gerber, A.; Petraru, A.; Fitsilis, M.; Meyer, R.; B.ttger, U.; Waser, R. Current Status and Challenges of Ferroelectric Memory Devices. *Microelectron. Eng*. **2005**, *80*, 296−304.

36. Lee, M.-S.; Park, K.-S.; Nam, S.-D.; Lee, K.-M.; Seo, J.-S.; Joo, S.- H.; Lee, S.-W.; Lee, Y.-T.; An, H.-G.; Kim, H.-J.; Cho, S.-L.; Son, Y.- H.; Kim, Y.-D.; Jung, Y.-J.; Heo, J.-E.; Park, S.-O.; Chung, U.-I.; Moon, J.-T. Integration of Ferroelectric Random Access Memory Devices with Ir/IrO2/Pb(ZrxTi1-x)O3/Ir Capacitors Formed by Metalorganic

Chemical Vapor Deposition-Grown Pb(ZrxTi1-x)O3. *Jpn. J. Appl. Phys*. **2002**, *41*, 6709−6713.

37. Pandya, S.; Wilbur, J.; Kim, J.; Gao, R.; Dasgupta, A.; Dames, C.; Martin, L. W. Pyroelectric Energy Conversion with Large Energy and Power Density in Relaxor Ferroelectric Thin Films. *Nat. Mater*. **2018**, *17*, 432−438.

38. Lallart, M.; Guyomar, D. Ferroelectric Materials for Small- Scale Energy Harvesting Devices and Green Energy Products. Ferroelectrics Applications. *Intech Open*, **2011**, 95−114.

39. Bowen, C. R.; Kim, H. A.; Weaver, P. M.; Dunn, S. Piezoelectric and Ferroelectric Materials and Structures for Energy Harvesting Applications. *Energy Environ. Sci*. **2014**, *7*, 25−44.

40. Li, Q.; Wang, Q. Ferroelectric Polymers and Their Energy Related Applications. *Macromol. Chem. Phys*. **2016**, *217*, 1228−1244.

41. Garbovskiy, Y.; Zribi, O.; Glushchenko, A. In Emerging Applications of Ferroelectric Nanoparticles in Material Technologies, Biology, and Medicine. *InTech*, **2013**, 475-497.

42. Zhao, Z.; Buscaglia, V.; Viviani, M.; Buscaglia, M. T.; Mitoseriu, L.; Testino, A.; Nygren, M.; Johnsson, M.; Nanni, P. Grain-size Effects on the Ferroelectric Behavior of Dense Nanocrystalline BaTiO3 Ceramics. *Phys. Rev. B: Condens. Matter Mater. Phys*. **2004**, *70*, 024107.

43. Selbach, S. M.; Tybell, T.; Einarsrud, M.-A.; Grande, T. SizeDependent Properties of Multiferroic BiFeO3 Nanoparticles. *Chem. Mater*. **2007**, *19*, 6478−6484.

44. Huang, T.-C.; Wang, M.-T.; Sheu, H.-S.; Hsieh, W.-F. Size-Dependent Lattice Dynamics of Barium Titanate Nanoparticles. *J. Phys.: Condens. Mater.* **2007**, *19*, 476212.

45. Junquera, J.; Ghosez, P. Critical Thickness for Ferroelectricity in Perovskite Ultrathin Films. *Nature* **2003**, *422*, 506−509.

46. Almahmoud, E.; Kornev, I.; Bellaiche, L. Dependence of Curie Temperature on the Thickness of and Ultrathin Ferroelectric Film. *Phys. Rev. B: Condens. Matter Mater. Phys.* **2010**, *81*, 064105.

47. Varghese, J.; Whatmore, R. W.; Holmes, J. D. Ferroelectric Nanoparticles, Wires and Tubes: Synthesis, Characterisation and Applications. *J. Mater. Chem. C* **2013**, *1*, 2618−2640.

48. Wrenn, T. L.; McBride, J. R.; Mares, J. W.; Rosenthal, S. J. Ferroelectric Particles Generated through a Simple, Room-Temperature Treatment of CdSe Quantum Dots. *Chem. Mater*. **2015**, *27*, 3817−3820.

49. Aubert, T.; Cirillo, M.; Flamee, S.; Van Deun, R.; Lange, H.; Thomsen, C.; Hens, Z. Homogeneously Alloyed CdSe1-xSx Quantum Dots (0<x<1): An Efficient Synthesis for Full Optical Tunability. *Chem. Mater*. **2013**, *25*, 2388-2390.

50. Keene, J. D.; McBride, J. R.; Orfield, N. J.; Rosenthal, S. J. Elimination of Hole-Surface Overlap in Graded CdSxSe1-x Nanocrystals Revealed by Ultrafast Fluorescence Upconversion Spectroscopy. *ACS Nano* **2014**, *8*, 10665−10673.

51. Harrison, M. A.; Ng, A.; Hmelo, A. B.; Rosenthal, S. J. CdSSe Nanocrystal with Induced Chemical Composition Gradients. *Isr. J. Chem*. **2012**, *52*, 1063−1072.

52. Shen, H.; Wang, H.; Tang, Z.; Niu, J. Z.; Lou, S.; Du, Z.; Li, L. S. High Quality Synthesis of Monodisperse zinc-blende CdSe and CdSe/ZnS nanocrystals with a phosphine-free method. *Cryst. Eng. Comm*. **2009**, *11*, 1733-1738.

53. Li, J. J.; Wang, A.; Guo, W.; Keay, J. C.; Mishima, T. D.; Johnson, M. B.; Peng, X. Large-Scale Syntehesis of Nearly Monodisperse CdSe/CdS Core/Shell Nanocrystals Using Air-Stable Reagents via Successive Ion Layer Adsorption and Reaction. *J. Am. Chem. Soc*. **2003**, *125*, 12567-12575.

54. Ghosh, Y.; Mangum, B. D.; Casson, J. L.; Williams, D. J.; Htoon, H.; Hollingsworth, J. A. New Insights into the Complexities of Shell Growth and the Strong Influence of Particle Volume in Nonblinking "Giant" Core/Shell Nanocrystal Quantum Dots. *J. Am. Chem. Soc*. **2012**, *134*, 9634-9643.

55. Bradsher, C. E.; McBride, J. R.; Macdonald, J. E.; Rosenthal, S. J. Modulating Ferroelectric Response in Colloidal Semiconductor Nanocrystals through Cation Exchange. *Chem. Mater*. **2019**, *32*, 4275-4281.

56. Banski M.; Afzaal, M.; Malik, M. A.; Podhorodecki, A.; Misiewicz, J.; O'Brien, P. Special Role for Zinc Stearate and Octadecene in the Synthesis of Luminescent ZnSe Nanocrystals. *Chem. Mater*. **2015**, *27*, 3797-3800.

57. Yu, W. W.; Qu, L.; Guo, W.; Peng, X., Experimental Determination of the Extinction Coefficient of CdTe, CdSe, and CdS Nanocrystals. *Chem. Mater*. **2003**, *15 (14)*, 2854-2860.

58. Allen, M. W., Measurement of Fluorescence Quantum Yields. *Thermo Fisher Scientific* **2010**; *Technical Note*: 52019.

59. Reid, K. R.; McBride, J. R.; Freymeyer, N. J.; Thal, L. B.; Rosenthal, S. J. Chemical Structure, Ensemble and Single-Particle Spectroscopy of Thick-Shell InP-ZnSe Quantum Dots. *Nano Lett*. **2018**, *18*, 709−716.

60. Pecherskaya, E. A. The Use of the Sawyer-Tower Method and its Modifications to Measure the Electrical Parameters of Ferroelectric Materials. *Measurement Techniques*, **2007**, *50*, 1101-1107.ect

61. Bouregba, R.; Poullain, G. Numerical Extraction of the True Ferroelectric Polarization Due to Switching Domains from Hysteresis Loops Measured Using A Sawyer-Tower Circuit. *Ferroelectrics*, **2002**, *274*, 165-181.

62. von Hippel, A. Piezoelectricity, Ferroelectricity, and Crystal Structure. *Z. Phys*. **1952**, *133*, 158−173.

63. Reid, K. R.; McBride, J. R.; La Croix, A. D.; Freymeyer, N. J.; Click, S. M.; MacDonald, J. E.; Rosenthal, S. J. Role of Surface Morphology on Exciton Recombination in Single Quantum-Dot-inRods Revealed by Optical and Atomic Structure Correlation. *ACS Nano* **2018**, *12*, 11434−11445.

64. Shannon, R. D.; Prewitt, C. T. Effective Ionic Radii in Oxides and Fluorides. *Acta Crystallogr., Sect. B: Struct. Crystallogr. Cryst. Chem.* **1969**, *25*, 925−946.

65. Scholdt, G.; Guoyamar, D.; Agbossou, A. On Thermoelectric and Pyroelectric Energy Harvesting. *Smart Materials and Structures*, **2009**, *18*, 125006

66. Hwang, S. J.; Jung, H. J.; Kim, J. H.; Ahn, J. H.; Song, D.; Song, Y.; Lee, H. L.; Park, H.; Sung, T. H. Desiging and Manufacturing a Piezoelectric Tile for Energy Harvesting. *Current Applied Physics*, **2015**, *15*, 669-674.

67. Kokkinopoulos, A.; Vokas, G.; Papageorgas, P. Energy Harvesting Implementing Embedded Piezoelectric Generators – The Potential for the Attiki Odos Traffic Grid. *Energy Procedia*, **2014**, *50*, 1070-1085.

68. Batra, A. K.; Bhattacharjee, S.; Chilvery, A. K.; Aggarwal, M. D.; Edwards,M. E.; Bhalla, A. Simulation of Energy Harvesting from Roads via Pyroelectricity. *Journal of Photonics for Energy,* **2011**, *1*, 014001.

69. Hadi, A. M. A.; Tawil, S. N. M.; Mohammad, T. N. T.; Syaripuddin, M. Energy Harvesting from Road by Pyroelectric Effect. *ARPN Journal of Engineering and Applied Sciences*, **2015**, *10*, 9884-9890.

70. Bowen, C. R.; Arafa, M. H. Energy Harvesting Technologies for Tire Pressure Monitoring. Systems. *Advanced Energy Materials*, **2014**, *5*, 1-17.

71. Van den Ende, D. A.; van de Wiel, H. J.; Groen, W. A.; van der Zwaag, S. Direct Strain Energy Harvesting in Automobile Tires Using Piezoelectric PZT-Polymer Composites. *Smart. Mater. Struct*. **2012**, *21*, 1-11.

72. Dutoit, N. E.; Wardle, B. L.; Kim, S. Design Considerations for MEMS-Scale Piezoelectric Mechanical Vibration Energy Harvesters. *Integrated Ferroelectrics*, **2005**, *71*, 121-160.

73. Liu, H.; Lee, C.; Kobayashi, T.; Tay, C. J.; Quan, C. Investigation of a MEMs Piezoelectrc Energy Harvester System with a Frequency-Widened-Bandwidth Mechanism Introduced by Mechanical Stoppers. *Smart Mater. Struct.* **2012**, *21*, 1-12.

74. Bowen, C. R.; Taylor, J.; LeBoulbar, E.; Zabek, D.; Chauhan, A.; Vaish, R. Pyroelectric Materials and Devices for Energy Harvesting Applications. Energy & Environmental *Science*, **2014**, *7*, 3836-3856.

75. Li, F.; West, J.; Glushchenko, A.; Cheon, C. I.; Reznikov Ferroelectric Nanoparticle/Liquid Crystal Colloidsfor Display Applications. *Journal of the SID*, **2006**, *14*, 523-527.

76. Cain, M. G.; Weaver, P. M.; Reece, M. J. Ferroelectric Materials for Fusion Energy Applications. *Journal of Materials Chemistry A*, **2016**, *4*, 10394.

77. Adireddy, S.; Lin, C.; Cao, B.; Zhou, W.; Caruntu, G. Solution-Based Growth of Monodisperse Cube-Like $BaTiO_3$ Colloidal Nanocrystals. *Chem. Mater.* **2010**, *22*, 1946-1948.

78. Smith, M. B.; Page, K.; Siegrist, T.; Redmond, P. L.; Walter, E. C.; Seshadri, R.; Brus, L. E.; Steigerwald, M. L. Crystal Structure and the Paraelectric-to-Ferroelectric Phase Transition of Nanoscale $BaTiO_3$. *J. Am. Chem. Soc.* **2008**, *130*, 6955-6963.

79. Huang, L.; Chen, Z.; Wilson, J. D.; Banerjee, S.; Robinson, R. D.; Herman, I. P.; Laubowitz, R.; O'Brien, S. Barium Titanate Nanocrystals and Nanocrystal Thin Films: Synthesis, Ferroelectricity, and Dielectric Properties. *J. Appl. Phys.* **2006**, *100*, 1-10.

80. Cohen, R. E. Origin of Ferroelectricity in Perovskite Oxides. *Nature*, **1992**, *358*, 136-138.

81. Pearson, R. G. Hard and Soft Acids and Bases. *J. Am. Chem. Soc.* **1963**, *85*, 3533-3539.

82. Green, M. The Nature of Quantum Dot Capping Ligands. *Journal of Materials Chemistry*, **2010**, *20*, 5797-5809.

83. Bastrakov, E. N.; Jaireth, S.; Mernagh, T. P. Solubility of Uranium in Hydrothermal Fluids at 25º to 300ºC: Implications for the Formation of Uranium Deposits. *Geoscience Australia*, **2010**, *29*, 1-94.

84. Murray, C. B.; Norris, D. j.; Bawendi, M. Synthesis and Characterization of Nearly Monodisperse CdE (E= S, Se, Te) Semiconductor Nanocrystallites. *J. Am. Chem. Soc.* **1993**, *115*, 8706–8715.

85. Neeleshwar, S.; Chen, C. L.; Tsai, C. B.; Chen, Y. Y.; Chen, C. C.; Shyu, S. G.; Seehra, M. S. Size-Dependent Properties of CdSe Quantum Dots. *Phys. Rev. B* **2005**, *71*, 201307.

86. Kagan, C. R.; Murray, C. B.; Nirmal, M.; Bawendi, M. G. Electronic Energy Transfer in CdSe Quantum Dot Solids. *Phys. Rev. Lett*. **1996**, *76*, 1517.

87. Soloviev, V. N.; Eichhofer, A.; Fenske, D.; Banin, U. Molecular Limit of a Bulk Semiconductor of the "Band Gap" in CdSe Cluster Molecules. *J. Am. Chem. Soc*. **2000**, *122*, 2673–2674.

88. Ekimov, A. I.; Hache, F.; Schanne-Klein, M. C.; Ricard, D.; Flytzanis, C. Absorption and Intensity-Dependent Photoluminescence Measurements on CdSe Quantum Dots: Assignment of the First Electronic Transitions. *J. Opt. Soc. Am. B* **1993**, *10*, 100–107.

89. Medintz, I. L.; Uyeda, H. T.; Goldman, E. R.; Mattoussi, H. Quantum Dot Bioconjugates for Imaging, Labelling and Sensing. *Nat. Mater*. **2005**, *4*, 435–446.

90. Guo, Y.; Shi, S.; Hagen, G.; Zank, B.; Arango, A. Core-Shell Colloidal Quantum Dots for Photovoltaics with Improved Open Circuit Voltage. *APS March Meet. 2019*, Abstr. id.F33.003 **2019**.

91. Niezgoda, J. S.; Yap, E.; Keene, J. D.; McBride, J. R.; Rosenthal, S. J. Plasmonic CuxInyS2 Quantum Dots Make Better Photovoltaics than Their Nonplasmonic Counterparts. *Nano Lett.* **2014**, *14*, 3262–3269.

92. Mangum, B. D.; Landes, T. S.; Theobald, B. R.; Kurtin, J. N. Exploring the Bounds of Narrow-Band Quantum Dot Downconverted LEDs. *Photonics Res.* **2017**, *5*, A13–A22.

93. Supran, G. J.; Shirasaki, Y.; Song, K. W.; Caruge, J.-M.; Kazlas, P. T.; Coe-Sullivan, S.; Andrew, T. L.; Bawendi, M. G.; Bulović, V. QLEDs for Displays and Solid-State Lighting. *MRS Bull*. **2013**, *38*, 703–711.

94. Derfus, A. M.; Chan, W. C. W.; Bhatia, S. N., Probing the Cytotoxicity of Semiconductor Quantum Dots. *Nano Lett.* **2004**, *4 (1),* 11-18.

95. Tamang, S.; Lincheneau, C.; Hermans, Y.; Jeong, S.; Reiss, P., Chemistry of InP Nanocrystal Syntheses. *Chem. Mater*. **2016**, *28 (8),* 2491-2506.

96. Taylor, P. N.; Schreuder, M. A.; Smeeton, T. M.; Grundy, A. J. D.; Dimmock, J. A. R.; Hooper, S. E.; Heffernan, J.; Kauer, M., Synthesis of Widely Tunable and Highly Luminescent Zinc Nitride Nanocrystals. *J. Mat. Chem. C* **2014**, *2 (22),* 4379-4382.

97. Xie, R.; Battaglia, D.; Peng, X., Colloidal InP Nanocrystals as Efficient Emitters Covering Blue to Near-Infrared. *J. Am. Chem. Soc*. **2007**, *129 (50),* 15432-15433.

98. Niezgoda, J. S.; Harrison, M. A.; McBride, J. R.; Rosenthal, S. J., Novel Synthesis of Chalcopyrite CuxInyS2 Quantum Dots with Tunable Localized Surface Plasmon Resonances. *Chem. Mater*. **2012**, *24 (16),* 3294-3298.

99. Guzelian, A. A.; Katari, J. E. B.; Kadavanich, A. V.; Banin, U.; Hamad, K.; Juban, E.; Alivisatos, A. P.; Wolters, R. H.; Arnold, C. C.; Heath, J. R., Synthesis of Size-Selected, Surface-Passivated InP Nanocrystals. *J. Phys. Chem*. **1996***, 100 (17),* 7212-7219.

100. Won, Y.-H.; Cho, O.; Kim, T.; Chung, D.-Y.; Kim, T.; Chung, H.; Jang, H.; Lee, J.; Kim, D.; Jang, E., Highly Efficient and Stable InP/ZnSe/ZnS Quantum Dot Light-Emitting Diodes. *Nature* **2019**, *575 (7784),* 634-638.

101. Xu, L.; Liang, H.; Yang, Y.; Yu, S. Stability and Reactivity: Positive and Negative Aspects for Nanoparticle Processing. *Chem. Rev.* **2018**, *118*, 3209-3250.

102. Chen, P. E.; Anderson, N. C.; Norman, Z. M. Owen, J. S. Tight Binding of Carboxylate, Phosphonate, and Carbamate Anions to Stoichiometric CdSe Nanocrystals. *J. Am. Chem. Soc.* **2017**, *139*, 3227-3236.

103. Zhou, Y.; Buhro, W. E. Reversible Exchange of L-Type and Bound-Ion-Pair X-Type Ligation on Cadmium Selenide Quantum Belts. *J. Am. Chem. Soc.* **2017**, *139*, 1288-12890.